SIMULATING SURFACE AIR POLLUTION IN THE UNITED STATES: AN EXAMINATION OF MAJOR INFLUENCES AND A DIAGNOSIS OF MODEL CAPABILITIES

‘

A Dissertation

Presented to the Faculty of the Graduate School

of Cornell University

in Partial Fulfillment of the Requirements of the Degree of

Doctor of Philosophy

by

Benjamin Edward Brown-Steiner

January 2015

© 2015 Benjamin Edward Brown-Steiner

ALL RIGHTS RESERVED

SIMULATING SURFACE AIR POLLUTION IN THE UNITED STATES: AN EXAMINATION OF MAJOR INFLUENCES AND A DIAGNOSIS OF MODEL CAPABILITIES

Benjamin Edward Brown-Steiner, Ph.D.

Cornell University, 2015

ABSTRACT

In this dissertation I explore various influences on the surface chemistry in the United States. The research is in three parts: (1) the influence of emissions from Asia on surface ozone mixing ratios in the US using a tracer chemistry scheme; (2) a diagnostic analysis of surface ozone chemistry simulations using a Global Climate Chemistry Model (GCCM) in the US; and (3) an examination of the changing freight transportation patterns and its influence on Black Carbon (BC) surface chemistry in the Midwestern and Northeastern US. For the first part, we find that the Asian influence on US surface ozone chemistry is maximum in the springtime and a minimum in the summertime. This springtime maximum is a result of a low, dispersed plume of Asian pollution entering the air space over North America in the springtime. In contrast, the plume of Asian pollution crosses North American air space in a tighter and higher plume and is inaccessible to surface dynamics which could impact surface ozone. For the second part, we find that overall the CESM CAM-Chem GCCM is capable of capturing many aspects of surface ozone chemistry in the US, especially in the Southeastern and Western US. However, biases result under different sets of paramaterizations in model configurations, which must be

accounted for in interpretation of GCCM results, including: (1) a large positive ozone bias when a 26-layer configuration is used and a reduced, but still positive, bias when a 56-layer configuration is chosen; and (2) utilizing online meteorology performs as good as or better when simulated a variety of ozone metrics than a simulation using forced meteorology. In the third part find that although the overall demand for transportation is increasing due to globalization and a fragmentation of the production process, the increases in technological efficiencies and emission factor regulations have resulted in a regionally averaged leveling-off or decrease in BC emissions from 1977 – 2007. The fabricated metal and construction sectors, with generally heavy freight, dominate the emission of BC. Finally, increases in BC emissions in urban centers are increasing as they continue to develop into production and transportation nodes.

BIOGRAPHICAL SKETCH

Benjamin grew up with a passion for learning and the good luck to live in a community and family that fostered and encouraged his passion. At a young age he, with his parents and brothers, loved catching, identifying, and releasing insects, stargazing, bird watching, fishing, and learning of the natural world and the scientific process. Through this experience, along with the public television program *Bill Nye the Science Guy,* he quickly figured out that he wanted to do some form of science in order to protect the natural world around him.

Throughout grade school and high school, Ben thrived under the guidance of his teachers, coaches, and parents as they encouraged him to fill his time with science, math, music, and learning. After graduating high school in 2004, and hoping to bridge the gap between the scientists and the public, Ben went to Clarkson University to study Civil Engineering. Gradually he learned that Civil Engineering was not the best means for achieving his goals, he switched to Environmental Engineering and graduated with honors in 2008. At Clarkson, in addition to gaining engineering training, he was exposed to philosophy (via Dr. Bill Vitek), environmental law (via Dr. Christopher Robinson), and literature (via Dr. Jan Wojcik). For his senior thesis he conducted a research project on biomass availability for biofuel production in New York State under the guidance of Dr. Susan Powers. Although he was unsure of what step he should take next, both Dr. Powers and Ben's academic advisor, Dr. Andrea Ferro insisted that he should proceed to a graduate research position.

Not knowing what field of science to study, and having research experience only in biofuel production, Ben arranged meetings with several professors in the Biological and Environmental Engineering department at Cornell University. Unfortunately, none of the researchers matched Ben's preferences, until on a whim an administrative assistant suggested meeting with a new professor, Dr. Peter Hess. In less than an hour, Peter Hess agreed to take Ben on as an M.S./Ph.D. graduate student. Over the next six years, Ben progressed from an engineer to a scientist, earned his doctoral degree, purchased a bow tie, and has been able to communicate science to non-scientists in the style of Bill Nye the Science Guy.

This dissertation is dedicated to science communicators everywhere.

The world would have one less dissertation and one less scientist

but for the passion for science I gained through your efforts.

ACKNOWLEDGEMENTS

I have had the fortune to be surrounded by a loving family and supportive community that encouraged and fostered by abilities and passions which led me to where I am today. I would like to thank them all expansively, but do not have the space to acknowledge their contributions completely here. I'd like to thank many of the academics and researches that have offered assistance and given my guidance throughout my time at Cornell University including (but not limited to): Peter Gierasch, Dan Wilks, Hugh Gaugh, Jr., Silvia Kloster, Sebastian Engelstaedtir, Stuart Riddick, Lei Meng, Qi Tang, Wenxiu Sun, Dan Ward, Samual Albani, Rajendra Paudel, Brian Buchanan, Josephine Archibald, Darrick Evensen, Katherine Evensen, Aurelia Evensen, Dan Fuka, Becky Majerison, Chris Berry, Asha Sharma, Kyle Delwiche, and many others.

To my parents, your love and support humbles me every day.

To my brothers, I feel lucky to be your friend as well as your brother.

To my best friend and partner, you are one in a million (but you fall within a bell curve).

To my teachers and advisors, I am amazed and thankful at the impact you all have.

To my committee, thank you for getting me through.

To my friends, old and new, I am glad our paths crossed and hope they keep crossing.

To Bill Nye, Carl Sagan, Stephen Schneider, Neil deGrasse Tyson, thank you.

TABLE OF CONTENTS

Biographical Sketch iii
Dedication iv
Acknowledgements v
Table of Contents vi
List of Figures viii
List of Tables ix

Chapter 1: Introduction 1

Chapter 2: Asian Influence on Surface Ozone Chemistry in the United States: A Comparison of Regional Chemistry, Seasonality, and Transport Mechanisms 10

I. Abstract 10
II. Introduction 11
III. Methods 13
IV. O_3A Distribution and Seasonality 17
V. Transport to the US Boundary Layer 22
VI. O_3A Signal Decomposition 24
VII. Comparisons to Other Studies 28
VIII. Discussion and Conclusion 29
IX. Acknowledgements 31
X. References 32
XI. Appendix (including Supplemental Material) 37

Chapter 3: On the Capabilities and Limitations of GCCM Simulations of Summertime Regional Air Quality: A Diagnostic Analysis of Ozone and Temperature Simulations in the US Using CESM CAM-Chem 42

I. Abstract 42
II. Introduction 43
III. Methods 47
A. Description of Simulation 47
B. Description of Emissions 50
1. Anthropogenic Emissions 50
2. Biomass Burning Emissions 51
3. Natural Emissions 51
4. CASTNET Selection and Filtration Criteria 52
5. Correction of Simulated Ozone to the Surface 53
6. Mixed Modeling 54
IV. Results 55
A. Mean Ozone and Temperature Biases and Interannual Variability 55
B. Ozone Response to Changes in Anthropogenic Emissions 59
C. Climate Penalty Factor 61

D. Extreme Value Theory Analysis 66
V. Discussion 69
VI. Conclusion 73
VII. Acknowledgements 79
VIII. References 79
IX. Appendix (including Supplemental Material) 87

Chapter 4: Black Carbon Emissions from Trucks and Trains in the Midwestern and Northeastern United States from 1977 - 2007 93
I. Abstract 93
II. Introduction 94
III. Methods 97
IV. Comparison Against Standard Existing BC Emissions Inventories 105
V. Results 109
VI. Discussion 116
VII. Conclusion 119
VIII. Acknowledgements 122
IX. References 122

LIST OF FIGURES

Figure 1.1:	Spatial and temporal scales of chapters in this dissertation	2
Figure 2.1:	Seasonal 5-year average O_3A over the Pacific and North America	16
Figure 2.2:	Zonal profiles of O_3A over East Asia, the Pacific, and the US	18
Figure 2.3:	Meridional profiles of O_3A Plume over the US	19
Figure 2.4:	O_3A concentrations following isentropic surfaces	20
Figure 2.5:	Seasonal composites of O_3A for well-defined low systems	23
Figure 2.6:	O_3A seasonal decomposition over the US	25
Figure 2.7:	Meridional profiles of net chemistry signal	27
Figure S2.1	Locations of sites for comparison to observations	38
Figure S2.2	Comparison to observations of monthly O_3 averages at 10 sites	39
Figure S2.3	Comparison to observations of O_3 diurnal cycle	40
Figure S2.4	Comparison to observations at various vertical levels	41
Figure 3.1:	Time series for total monthly NO_x emissions over the US	50
Figure 3.2:	Ozone and temperature correlations and regional definitions	52
Figure 3.3:	Summertime mean DM8H O_3 bias and interannual variation	56
Figure 3.4:	Summertime mean DMT bias and interannual variation	56
Figure 3.5:	Post-SIP to Pre-SIP DM8H O_3 difference	59
Figure 3.6:	Average daily summertime $m_{O3\text{-}T}$	62
Figure 3.7:	Time-scale comparison of $m_{O3\text{-}T}$	64
Figure 3.8:	Estimated return interval of a 100 ppb daily ozone event	67
Figure 3.9:	Surface layer climatological variables	70
Figure 4.1:	Thirteen state study region	97
Figure 4.2:	Process schematic	99
Figure 4.3:	Comparison of time series of BC emissions	106
Figure 4.4:	Comparison of spatial BC emissions	107
Figure 4.5:	Sectoral stacked bar plots of BC emissions	109
Figure 4.6:	Tonnage, GDP, Population, and Ton-Miles time series	110
Figure 4.7:	Sectoral time series, with/without transportation and EF changes	112
Figure 4.8:	Comparison of BC emissions from sub-regions	113
Figure 4.9:	Sectoral BC emissions from sub-regions	115
Figure 4.10:	Spatial BC emissions from selected sectors	116

LIST OF TABLES

Table 2.1:	Tracer definitions	13
Table 2.2:	Concentrations and ratios of O_3A and O_3	22
Table 2.3:	Comparison of East Asian contribution to North American O_3	28
Table 3.1:	Summary of CESM configurations	48
Table 3.2:	Summary of DM8H O_3 and DMT biases	57
Table 3.3:	Summary of Post-SIP to Pre-SIP DM8H O_3 difference	60
Table 3.4:	Summary of statistics accompanying Figures 3.2 and 3.6	63
Table 3.5:	Summary of Return Interval and Skewness	67
Table 3.6:	Summary Table, all metrics, all regions, all configurations	69
Table S3.1	Emissions comparison for Asia and US to other inventories	89
Table S3.2	Division of annual emissions by all sectors and all species	89
Table S3.3	Total annual emissions for all species	90
Table S3.4	DM8H O_3 bias at each site and for each configuration	91
Table S3.5	DMT bias at each site and for each configuration	92
Table 4.1:	Regional input-output sector definitions	98
Table 4.2:	Truck and rail emission factors	98

CHAPTER 1: INTRODUCTION

The emissions and concentrations of air pollutants and their precursors alter the chemistry of our atmosphere and the physical climate of our planet (Fiore et al., 2012). Regional atmospheric chemistry is influenced both by the local pattern of emissions as well as the regional manifestation of weather patterns, which themselves are manifestations of regional and global climate. However, all of this chemistry, weather, and climate, with the exception of fleeting phenomena such as clouds, precipitation, haze, and plumes, are invisible to us and thus difficult to directly experience. As a result, we must turn to a variety of tools and frequently abstract visualizations to understand what is happening in the atmosphere we are dependent on for our survival.

The research conducted for this dissertation has examined various interactions between atmospheric chemistry and regional and global climate largely through the use of a powerful tool: the Community Earth Systems Model with Chemistry (CESM CAM-Chem). This tool is one of many new Global Climate-Chemistry Models (GCCMs), which have emerged from a variety of General Circulation Models / Global Climate Models (GCMs), which have genealogies stretching back to the 1960s (Mason and Knutti, 2011). Comparatively, GCCMs have emerged only in the 1990s (e.g. Rasch et al., 1997), and thus are relatively new tools for understanding atmospheric chemistry and climate.

The specific research focus of this dissertation has been to examine aspects of ozone and black carbon chemistry on intercontinental and regional scales. Since air quality is largely a regional problem, the analysis conducted as part of this research has been on the impacts of global climate and chemical changes on the local scale and on timescales as short as five years. Future work (as part of the post-doctoral work to finish the current project) is going to simulate

BC with a regional chemical transport model (CTM), the WRF-Chem (e.g. Ma et al., 2014), rather than the CESM CAM-Chem. In this introduction I briefly explore some of the aspects of the question: what model (i.e. global or regional) is appropriate for simulating atmospheric chemistry and climate at what spatial and temporal scales and why?

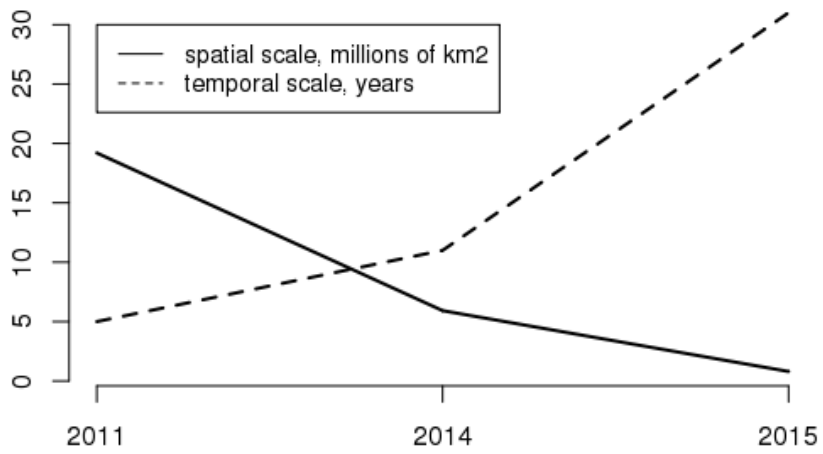

Figure 1.1: Spatial and Temporal Scales of the Three Chapters in this Dissertation. The years are the dates of publication (or expected data of publication) of each paper.

Figure 1.1 shows the progression of spatial and temporal scales the three chapters of this dissertation. The papers have time scales of 5, 11, and 31 years with corresponding spatial scales moving form intercontinental to regional to sub-regional. This progression of increasing length of time and decreasing spatial scale is interesting in that it crosses some muddy boundaries between weather and climate and raises some important questions, which are explored below.

Largely GCCMs have not been retuned from the GCM physical parameters to match atmospheric chemical conditions. This has the potential of influencing much of the atmospheric chemistry output as the GCM model tuning aimed at achieving physical climate objectives (i.e. temperature, sea level pressure, top-of-atmosphere radiative balance) rather than chemical objectives (i.e. atmospheric chemical composition). Any tuning process is necessarily subjective

and has the potential to tune is such as way as to incorporate complimentary errors in the model framework (Mauristen et al., 2012).

Model output from GCMs and now GCCMs have typically been on grids with resolution on the order of 1x1 degree latitude and longitude. As with any model, he question weather the model is good or bad depends on the question being asked (Knutti et la, 2010b) and since these models are global in scale and their analysis is primarily focused on large-scale aspects of the earth climate system. Any tuning of these models is thus focused on large-scale aspects and not tuned for accurate depictions of small-scale features (Raisanen and Ylhaisi, 2011). Subsequently, there is little confidence in the output of these models on regional scales, which has lead many researches to generally average their results from individual grid cells to larger scales (e.g. regional or continental) or to average multiple models together to eliminate individual model noise (Raisanen and Ylhaisi, 2011). Our use of Mixed Model statistical analysis in Brown-Steiner et al., (2015) attempted to represent interregional variability while still accounting for small-scale variability.

Similarly, GCMs and GCCMs are designed and tuned to represent aspects of the climate, which are by definition long-term averages (of at least 5 years and typically much more) and not the weather. Especially if the models simulate their own meteorology there is no expectation for the models to reproduce individual meteorological phenomena. Even when forced meteorology is used to drive the model simulations, the choice of meteorological dataset and various aspects of data set itself result in differences in the ultimate output (e.g Hess and Mahowald, 2009).

Nearly a decade ago, Lawrence (2005) introduced the term “chemical weather” as:

> Local, regional, and global distributions of important trace gases and aerosols and their variabilities on time scales of minutes to

> hours to days, particularly in light of their various impacts, such as on human health, ecosystems, the meteorological weather, and climate. (Lawrence, 2005).

This definition was intended to mirror the definition of meteorological weather, which is to be distinguished from climate (e.g. AR5 Box: FAQ 11.1: "If you cannot predict the weather next month, how can you predict the climate for the coming decade?"). The phrase 'chemical weather' has not become as prevalent as the original authors expected. It has primarily been adopted in Europe (e.g. Kukkonen et al., 2012) and a lingering usage in material describing and discussion the WRF-Chem model (e.g. http://ruc.noaa.gov/wrf/WG11/). Additionally short-term chemical weather forecasts are currently available in the US (e.g. http://www.airnow.gov/, http://airquality.weather.gov/, http://www.weather.com/activities/health/airquality/, and http://www.air.dnr.state.ga.us/amp/) although the phrase 'chemical weather' is not used to describe or explain these forecasts.

Similarly a formal definition of "chemical climate" has been proposed by Möller (2010):

> The synthesis of chemical weather conditions in a given area, characterized by long-term statistics (mean values, variances, probabilities of extreme values, etc.) of the chemical substances in that area. (Möller, 2010)

This accurate simulation of chemical climate has been the objective of GCMs and GCCMs since the beginning, and just as GCMs are expected to reproduce the earth's climate and not the earth's weather, GCCMs should be expected to reproduce the earth's chemical climate and not the earth's chemical weather. This is addressed in the most recent IPCC report, the AR5 in Chapter 11, Box 11.1. At short time scales (less than one year), simulations are focused on weather

predictions and are ultimately an initial conditions problem. At long time scales (greater than 10 years), simulations are climate predictions and are forced boundary condition problems. In between (from 1 year to 10 years) simulations and projections are classified as seasonal to interannual.

In Brown-Steiner and Hess (2011) we examine ozone trends on a 5-year timescale with forced meteorology, which most closely matches the definition for chemical weather and is between an initial value problem and a forced boundary condition problem. For Brown-Steiner et al., (2015) we simulate 11-years of ozone chemistry using both forced and simulated meteorology, which is somewhere between the chemical weather and chemical climate domains, leaning more towards the forced boundary condition domain.

And while the final research (Brown-Steiner et al, in preparation) is preparing 31-year emissions of BC, which is well within the chemical climate domain, the spatial scale of this project is a sub-region within the US. The question of whether a GCCM is capable of simulating chemical climate on that spatial scale (e.g. Räisänen and Ylhäisi, 2011) is one of the main reasons we are considering the use of the WRF-Chem CTM for these simulations.

In addition, in this 'in-between' time scale of 1 to 10 years we also have to address the potential for interannual or inter-decadal oscillations and cycles to complicate our results. The US, where all of the research for this dissertation is focused, is an area which experiences variability due to seasonal (NOA/PNA), interannual (e.g. ENSO) (e.g. Deser et al., 2012, Pierce et al, 2009; Elia et al., 2013) and inter-decadal (e.g. PDO/PNA) (e.g. Lin et al., 2014), although this variability is smaller than in other regions of the globe (Hess and Mahowald, 2009). In Brown-Steiner et al., (2015) we simulate a dramatic change in NO_x emissions in the Eastern US on a time scale that can be classified as a change in chemical weather. The possible influence of

ENSO or other oscillations is not negligible and potential metrics such as the Time of Emergence (ToE) or the Expected Year of Emergence (EYE) (Hawkins and Sutton, 2012) may need to be extended to chemical weather and chemical climate aspects of the atmospheric system. Future work at this temporal and spatial scale should be cautious about the potential for interference from these oscillations and cycles.

All of these questions and cautions deal with aspects of uncertainty: uncertainty about emissions, variability, model capability, and signal detection. Even more so than in GCMs GCCMs are simulating complex interactions with dozens of species and processes which are parameterized with limited ability for observational verification (e.g. Räisänen, 2007). The growing attention given to classifying and characterizing uncertainty (e.g. Clavreul et al., 2013, Senge et al., 2014) are particularly applicable to GCCMs, CTMs, and all aspects of chemical weather and chemical climate.

Ultimately, we are posing questions of model reliability (e.g. Räisänen, 2007) and our trust in the ability of the CESM CAM-Chem GCCM to simulate chemical weather and chemical climate, which, unfortunately, are not typically addressed in publications of this nature. The interbreeding of these models (Mason and Knutti, 2011) spawns questions of model independence (Knutti, 2010a) and capabilities. In addition to the existing questions regarding aleatoric/statistical uncertainty (Hora et al., 1996) (e.g. What are the natural variations we can expect and how are we able to extract signals from the physical and chemical noise in the earth system?) we have many growing questions concerning epistemic/systematic uncertainty (Hora et al., 1996): Do we understand and are we simulating the correct forcings (forcing uncertainty)? Do we adequately understand and are we accurately simulating the correct parameters? How can we test, observe, and verify our understanding and simulation of these parameters (parameter

uncertainty)? Are we accurately and sufficiently simulating the physical and chemical system (structural uncertainty)?

The three following chapters in this dissertation serve as independent attempts at examining and understanding the nature and scale (both spatial and temporal) of surface chemistry in the United States. We show that the CESM CAM-Chem is a powerful tool, which can allow us to create artificial tracers and examine aspects of atmospheric chemistry and atmospheric dynamics that are difficult to measure directly (Chapter 2). We take a critical approach with a diagnostic analysis of the modeling capabilities of the CESM CAM-Chem under four configurations utilizing different parameterizations, and find that interpretation of GCCM results must be made with caution and with knowledge of the influence of differences among parameterizations (Chapter 3). Finally, we develop a stylized transportation and emissions model, which will allow us to examine the impact of changing transportation, economic, and regulatory systems on BC emissions in the Midwestern and Northeastern US (Chapter 4).

REFERENCES

Brown-Steiner, B., Hess, P., 2011. Asian influence on surface ozone in the United States: A comparison of chemistry, seasonality, and transport mechanisms. J. Geophys. Res. 116, 1–13. doi:10.1029/2011JD015846

Brown-Steiner, B., Chen, J., and Donaghy, K., in press. The Evolution of Freight Movement and Associated Non-Point Source Emissions in the Midwest-Northeast Transportation Corridor of the United States, 1977 – 2007. In: *The Region and Trade: New Analytical Directions.* Batabyal, P.A. and Nijkamp, P. (eds).

Clavreul, J., Guyonnet, D., Tonini, D., Christensen, T.H., 2013. Stochastic and epistemic uncertainty propagation in LCA. Int. J. Life Cycle Assess. 18, 1393–1403. doi:10.1007/s11367-013-0572-6

Deser, C., Knutti, R., Solomon, S., Phillips, A.S., 2012. Communication of the role of natural variabiliyt in future North American climate 2, 775–780. doi:10.1038/NCLIMATE1562

Hawkins, E., Sutton, R., 2012. Time of emergence of climate signals. Geophys. Res. Lett. 39, n/a–n/a. doi:10.1029/2011GL050087

Hess, P., Mahowald, N., 2009. Interannual variability in hindcasts of atmospheric chemistry : the role of meteorology. Atmos. Chem. Phys. 9, 5261–5280. doi:doi:10.5194/acp-9-5261-2009

Hora, S.C., 1996. Aleatory and epistemic uncertainty in probability elicitation with an example from hazardous waste management. Reliab. Eng. Syst. Saf. 54, 217–223. doi:10.1016/S0951-8320(96)00077-4

Knutti, R., 2010. The end of model democracy? Clim. Change 102, 395–404. doi:10.1007/s10584-010-9800-2

Knutti, R., Furrer, R., Tebaldi, C., Cermak, J., Meehl, G. a., 2010. Challenges in Combining Projections from Multiple Climate Models. J. Clim. 23, 2739–2758. doi:10.1175/2009JCLI3361.1

Kukkonen, J., Olsson, T., Schultz, D.M., Baklanov, a., Klein, T., Miranda, a. I., Monteiro, a., Hirtl, M., Tarvainen, V., Boy, M., Peuch, V.-H., Poupkou, a., Kioutsioukis, I., Finardi, S., Sofiev, M., Sokhi, R., Lehtinen, K.E.J., Karatzas, K., San José, R., Astitha, M., Kallos, G., Schaap, M., Reimer, E., Jakobs, H., Eben, K., 2012. A review of operational, regional-scale, chemical weather forecasting models in Europe. Atmos. Chem. Phys. 12, 1–87. doi:10.5194/acp-12-1-2012

Lawrence, M.G., Hov, Ø., Beekmann, M., Brandt, J., Elbern, H., Eskes, H., Feichter, H., Takigawa, M., 2005. The Chemical Weather. Environ. Chem. 2, 6–8. doi:10.1071/EN05014

Lin, M., Horowitz, L.W., Oltmans, S.J., Fiore, A.M., Fan, S., 2014. Tropospheric ozone trends at Mauna Loa Observatory tied to decadal climate variability. Nat. Geosci. 7, 136 – 143. doi:10.1038/NGEO2066

Ma, P.-L., Rasch, P.J., Fast, J.D., Easter, R.C., Gustafson Jr., W.I., Liu, X., Ghan, S.J., Singh, B., 2014. Assessing the CAM5 physics suite in the WRF-Chem model: implementation, resolution sensitivity, and a first evaluation for a regional case study. Geosci. Model Dev. 7, 755–778. doi:10.5194/gmd-7-755-2014

Masson, D., Knutti, R., 2011. Climate model genealogy. Geophys. Res. Lett. 38, 1–4. doi:10.1029/2011GL046864

Mauritsen, T., Stevens, B., Roeckner, E., Crueger, T., Esch, M., Giorgetta, M., Haak, H., Jungclaus, J., Klocke, D., Matei, D., Mikolajewicz, U., Notz, D., Pincus, R., Schmidt, H., Tomassini, L., 2012. Tuning the climate of a global model. J. Adv. Model. Earth Syst. 4, 1–18. doi:10.1029/2012MS000154

Möller, D. Chemistry of the Climate System, 2010. Walter de Gruyter GmbH & Co., KG, Berlin/New York.

Pierce, D.W., Barnett, T.P., Santer, B.D., Gleckler, P.J., 2009. Selecting global climate models for regional climate change studies. Proc. Natl. Acad. Sci. U. S. A. 106, 8441–6. doi:10.1073/pnas.0900094106

Räisänen, J., 2007. How reliable are climate models? Tellus 59, 2–29. doi:10.1111/j.1600-0870.2006.00211.x

Räisänen, J., Ylhäisi, J.S., 2011. How Much Should Climate Model Output Be Smoothed in Space? J. Clim. 24, 867–880. doi:10.1175/2010JCLI3872.1

Rasch, P.J., Mahowald, N.M., Eaton, B.E., 1997. Representations of transport, convection, and the hydrologic cycle in chemical transport models: Implications for the modeling of short-lived and soluble species. J. Geophys. Res. 102, 28127–28138. doi:10.1029/97JD02087

Senge, R., Bösner, S., Dembczyński, K., Haasenritter, J., Hirsch, O., Donner-Banzhoff, N., Hüllermeier, E., 2014. Reliable classification: Learning classifiers that distinguish aleatoric and epistemic uncertainty. Inf. Sci. (Ny). 255, 16–29. doi:10.1016/j.ins.2013.07.030

CHAPTER 2: ASIAN INFLUENCE ON SURFACE OZONE IN THE UNITED STATES: A COMPARISON OF CHEMISTRY, SEASONALITY, AND TRANSPORT MECHANISMS

Benjamin Brown-Steiner and Peter Hess

Published in the Journal of Geophysical Research, Volume 116, Issue D17309, 2011.

I. Abstract

Ongoing growth in Asia has increased emissions of several ozone precursors which are increasingly impacting surface ozone levels in the US. We use the offline Community Atmospheric Model with Chemistry (CAM-Chem) driven by National Center for Environmental Protection (NCEP) meteorology for 2001 – 2005 and chemistry, plus additional tagged tracers, to examine the chemistry, seasonality, and transport of Asian emissions as they are lofted from the Asian boundary layer into the free troposphere over the Pacific Ocean and into the US. In the western US, Asian ozone (O_3A) concentrations are maximum in the spring at 3.36 ± 1.3 ppbv and are minimum in the summer at 1.36 ± 0.7 ppbv. Transport of O_3A and its precursors to the surface of the US depends on the structure of the elevated O_3A plume and available meteorological transport mechanisms, such as dry air streams associated with midlatitude cyclones, which can tap and transport pollutants to the surface. We show that the structure of this plume has a strong seasonal dependence, entering the US in the spring widely dispersed in the lower free troposphere and boundary layer (0 – 6 km) with O_3A concentrations between 5 and 10 ppbv and in the summer in a tight plume in the upper free troposphere centered at 8 km with peak O_3A of 11 ppbv. This pattern is in contrast to total O_3 concentrations which show a summertime peak, which implies that the largest Asian impact on surface ozone in the US will be in the off-peak spring season.

II. Introduction

Substantial growth in transportation, coal-fired power plants and the industrial sectors in Asia have resulted in sharp increases in the emissions of O_3 precursors (CO, non-methane hydrocarbons (NMHCs), and NO_x (NO and NO_2)) and other criteria air pollutants (Ohara et al., 2007; Streets et al. 2003), which can impact surface O_3 concentrations in the US (e.g. Cooper et al., 2010; Fiore et al., 2002, Jacob et al., 1999, Holzer et al., 2007 and references therein). While the transport of pollutants out of the Asian BL and over the Pacific has been extensively measured and studied (during the Pacific Exploratory Mission (PEM-West) field campaign (e.g. Hoell et al., 1997) and the Transport and Chemical Evolution over the Pacific (TRACE-P) field campaign (e.g. Crawford et al., 2004; Hannan et al., 2003; Jacob et al., 2003; Mari et al., 2004)) and Asian pollutant plumes have been measured over the west coast of the US and in the eastern Pacific (during the Intercontinental Transport and Chemical Transformation (ITCT) 2002 field campaign (e.g. Parrish et al., 2004; Goldstein et al., 2004; Jaffe et al. 2003) and the Intercontinental Chemical Transport Experiment (INTEX-B) field campaign (e.g. Singh et al., 2009; Zhang et al., 2009)), relatively little is known about the processes that bring ozone down to the surface of the US. In this study we examine these processes in detail, including their seasonality, distribution, and impact on surface O_3.

East Asian pollutants can be effectively lofted from the BL into the FT by lifting ahead of midlatitude cyclones and deep convection (Liang et al., 2004, 2007; Liu et al., 2003; Mari et al., 2004) and then rapidly transported into North American air space by the free-tropospheric westerlies. Transport that occurs exclusively in the Pacific BL accounts for only a small fraction of the total East Asian influence during the spring season (Holzer et al., 2007). This transport is episodic (Mari et al., 2004; Zhang et al., 2008), but both observations (Husar et al., 2001; Jaffe et

al., 1999, 2003; Liang et al., 2007; Liu et al., 2003, Tang et al., 2004) and models (Hess and Vukicevic, 2003; Stohl et al., 2002; Yienger et al., 2000) have demonstrated that Asian pollutants can reach the North American FT every 3 – 9 days.

These pollutants form a free tropospheric plume that can be found during all seasons over North America (Liang et al., 2007; Wang et al., 2006; Yienger et al., 2000). A majority of the Asian pollutants pass over North America, but a portion is brought down to the BL and can impact North American surface O_3 (Cooper et al., 2004, 2005). The spring season shows the highest US surface concentrations of O_3 produced from precursors originating from outside the US (Fiore et al., 2003; Husar et al., 2001; Jacob et al., 1999; Reidmiller et al., 2009; Weiss-Penzias et al., 2006) with surface concentrations of 2 - 5 ppbv in the western US, 1 - 3 ppbv in the central US, and 0 - 1 ppbv in the eastern US (Jaffe et al., 1999, 2003; Zhang et al., 2008).

This study uses the offline Community Atmospheric Model with Chemistry (CAM-Chem) driven by National Center for Environmental Protection (NCEP) reanalysis meteorology to examine the seasonality, distribution, and transport mechanisms of the Asian influence on surface ozone in the US. It provides modeling evidence for the dominant role of isentropic subsident transport of pollutants into the BL in post-frontal systems in the US. The ability of synoptic scale transport to bring O_3 produced from Asian precursors to the surface depends on the intermittent presence of high-O_3 pollutant plumes in the free troposphere, that these mechanisms can tap into. We show that the availability of this ozone depends in turn on ozone production over Asia, the transport of this ozone to the U.S. and the production or destruction of this ozone enroute. The relative importance of these various processes produce a springtime maximum in surface O_3 and a summertime maximum in upper tropospheric O_3 in the US. While it has been established that mid-latitude cyclones can adiabatically transport polluted BL air into

the FT in the warm conveyor belt (e.g. Browning and Roberts, 1994; Cooper et al., 2002; Liang et al., 2004; Hannan et al., 2003), transport of pollutants from the FT to the BL in the post-cold front descending dry air (DA) stream is less well established (see Liang et al., 2004). Section 2 of this paper describes the methods, tracers, and simulation. Section 3 explores the distribution and seasonality of O_3A and Section 4 explores mechanisms and evidence for the transport of O_3A into the US boundary layer. Section 5 explains the seasonal variations in O_3A into transport and chemical components, and Section 6 compares the results of this study with other similar studies. Section 7 includes the final discussions and conclusions.

III. Methods

Table 2.1: Summary of the various tracers used in the simulation

Description of Tracer	O_3A "Anthropogenic Asian O_3…"	O_3Atr "…tracer…"	O_3AtrCS "…with constant source…"
Chemistry	full chemistry	none	none
Production	full chemistry	explicitly set to match O3A over Asia	explicitly set to 10 ppb over Asia
Loss	full chemistry	none	none
Spatial Limitations?	no	yes*	yes*

*: these two tracers are set to zero outside of the northern hemisphere and between 0° – 60° N from 60° W - 60° E.

This study simulates the global circulation and chemistry for the years 2001 to 2005 using the offline version of the National Center for Atmospheric Research (NCAR) Community Climate System Model – Community Atmospheric Model (CCSM-CAM) version 3.65, a three-dimensional global circulation model driven by offline meteorological fields (see Pfister et al, 2006), with incorporated Model for Ozone and related chemical Tracers, version 4 (MOZART-4) chemistry. See http://www.ccsm.ucar.edu/models/atm-cam/docs/description/ for a detailed description of the model and Emmons et al. (2010) for a description of the MOZART-4 chemical mechanism used for this simulation. The standard chemical mechanism includes 85 gas-phase species with 39 photolysis and 157 gas-phase reactions. A similar model set-up was used for

diagnosing intercontinental transport as part of the Task Force on Hemispheric Transport of Air Pollution (HTAP) (see www.htap.org for the 2010 Assessment Report). The mechanism utilized for this study included additional tracer species and their associated reactions so as to tag O_3 generated from Asian precursor species, as described below.

The offline meteorology is from the NCEP reanalysis data from 2000 – 2005 with a 1.9°x2.5° degree horizontal resolution and 28 vertical layers from the surface to 2.7 hPa. The initial year is not analyzed. Model evaluation against surface measurements and with respect to simulated intercontinental transport in a multitude of other models was performed by HTAP (2010), Fiore et al. (2009), Jonson et al. (2010), and Shindell et al. (2008). Emissions for this simulation are the same as those from the HTAP runs (see Fiore et al. (2009) and HTAP (2010)), which allows for a comparison of the results.

In addition to the MOZART-4 chemistry, added tracers tag NO_x emissions over East Asia (xNO_x) and follow their chemical transformations throughout the total reactive nitrogen family. Any O_3 created from species that originated as xNO_x emissions are tagged as O_3A, which represents a molecule of O_3 that can be traced back to anthropogenic xNO_x emitted over East Asia. O_3A concentrations and chemical production and destruction are explicitly calculated in addition to the other MOZART-4 chemical species. This method has been utilized in several previous studies (e.g. Hess and Lamarque, 2007; Murazaki and Hess, 2006) as is estimated to be 95% accurate at reproducing anthropogenic ozone production on a monthly basis (Lamarque et al., 2005). East Asia is defined as the area between 15° and 50° N, and 95° – 160° E, which matches the definition of East Asia found in Fiore et al. (2009). In addition, several other tracers were included in these model simulations to further explore the details and mechanisms of O_3 transport and chemistry (Table 2.1) and are described below.

The artificial tracer O_3Atr has its concentrations explicitly set to those of O_3A over East Asia from the surface up to the tropopause. O_3Atr has no explicit simulated chemistry or loss, but its concentration is set to zero outside of a specified latitude and longitude range (see Table 2.1). This prevents the build-up of O_3Atr within the model and allows us to examine the impact of direct transport pathways between Asia and North America. The second tracer, O_3AtrCS (constant source) is set to a constant 10 ppbv over East Asia year-round from the surface to the tropopause, where 10 ppb is the approximate annual averagí concentration of O_3A over East Asia. For the calculation of the baseline transport signal this was then scaled to the actual modeled year-round O_3A concentrations over East Asia from the surface to the tropopause. The difference between O_3Atr and O_3AtrCS concentrations is used to examine seasonality and chemistry signals in Section V.

While the coastal influence and complex topography of the western US makes it particularly interesting, it complicates the structure and our ability to isolate the transport and impacts of mid-latitude cyclones. Therefore, this study includes simulation results for the western, central, and eastern US, but focuses on the central US for a better understanding of the structure and seasonality of mid-latitude cyclones and their associated transport mechanisms. The topography of the central US allows for well-defined mid-latitude cyclone systems without a strong coastal influence, and still has a significant (around 5%) Asian influence even though the O_3A plume is lower in concentrations and higher in altitude.

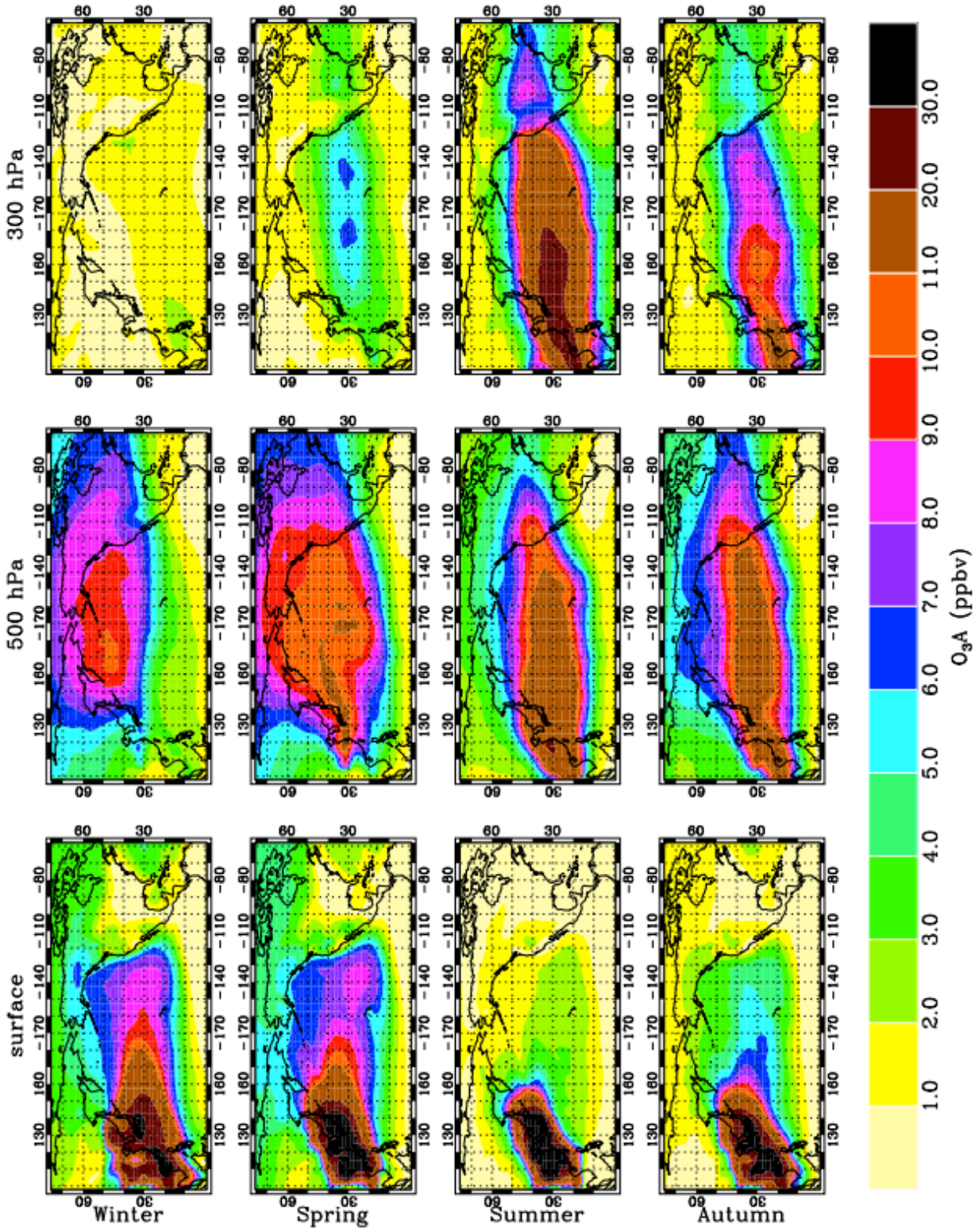

Figure 2.1: Seasonal 5-year average of O_3A over the Pacific Basin and North America at the surface, 500 hPa (approximately 5 km), and 300 hPa (approximately 10 km) taken from the 2001 – 2005 model results.

IV. O_3A Distribution and Seasonality

This section examines the 5-year seasonal average O_3A plume between East Asia and North America. Daily variability of O_3A concentrations is high, is strongly dependent on local meteorology, and is explored in the next section. Seasonally averaged O_3A generally forms a plume originating at the surface in East Asia that extends into the FT and over the Pacific Ocean into the North American FT. Figure 2.1 shows the 5-year average O_3A plume for each season at the surface layer, 500 hPa layer (around 5 km), and the 300 hPa layer (around 10 km).

The O_3A plume can be divided into two distinct seasonal regimes: the winter/spring regime and the summer/autumn regime. In the winter/spring regime, O_3A concentrations are generally high (greater than 5 ppbv) in the BL and lower and middle FT extending from East Asia to the North American west coast. Overall, the highest concentrations are found in the BL directly over East Asia between 20 and 30 ppbv. Over the Eastern Pacific Ocean and western North America, the highest O_3A concentrations (8 – 11 ppbv) are found in the middle FT (at 500 hPa) and extend from 20° N to 75° N over much of the Pacific Ocean and North America. Both in the BL and in the upper FT over North America the winter/spring O_3A concentrations are markedly lower (typically less than 5 ppbv). O_3A concentrations in excess of 7 ppbv reach the Atlantic Ocean in the middle FT. US surface O_3A concentrations are typically below 5 ppbv with maximum concentrations at the surface of the western US.

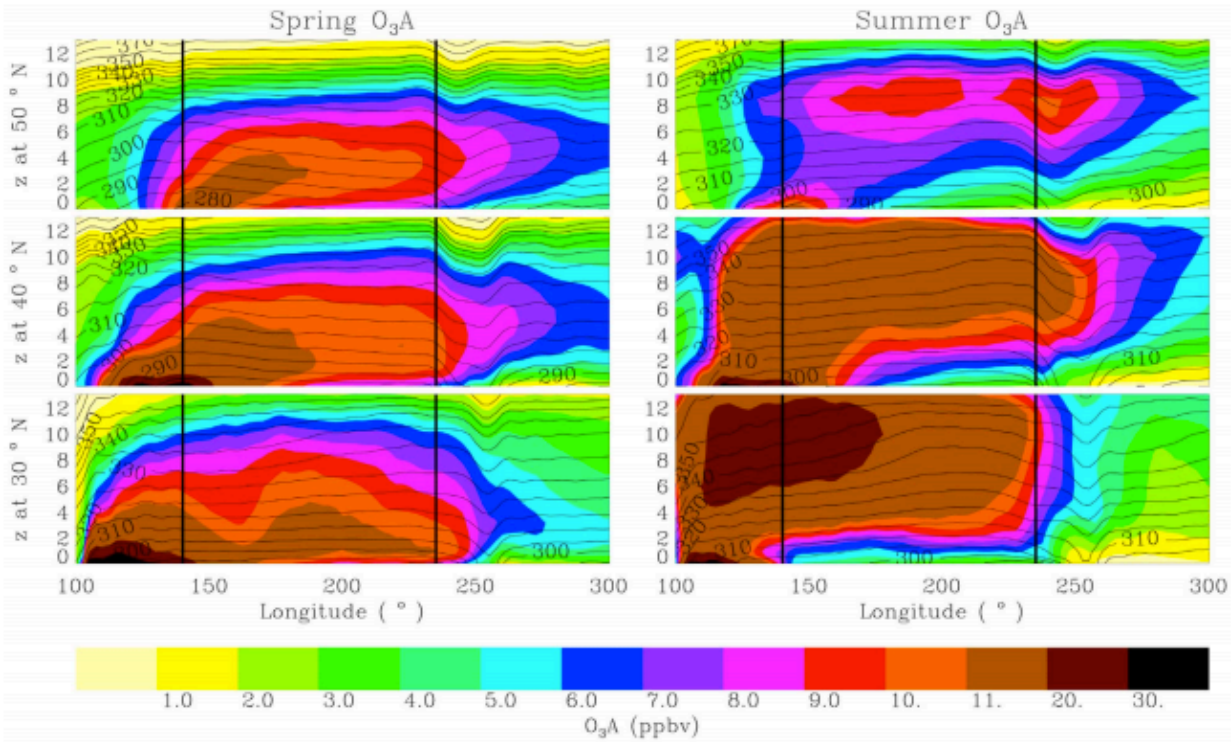

Figure 2.2: Zonal profiles of O_3A concentrations over East Asia, the Pacific Basin, and the U.S. at 30°, 40°, and 50° N for the spring and summer averages. Isentropic surfaces are also plotted (solid lines).

The summer/autumn regime has lower O_3A concentrations at the surface over the Pacific Ocean (less than 5 ppbv) with high O_3A concentrations (5 – 30 ppbv) concentrated in a tight latitudinal band centered at 30° N and filling the middle and upper FT (6 – 10 km). Peak O_3A in this regime is found in the upper FT directly over East Asia in excess of 20 ppbv. O_3A concentrations comparable to the winter/spring regime reach the Atlantic Ocean in the lower FT, but O_3A concentrations at the surface in the US are lower (typically 0 – 3 ppbv) than found in the winter/spring regime.

In the absence of diabatic (i.e. latent) heating and cooling, air parcels in the troposphere tend to move along isentropic surfaces rather than across them. Figure 2.2 gives the height cross-section of the O_3A plume as it is lifted over EA and carried over the Pacific and North America with isentropic surfaces plotted (black lines). Figure 2.2 only shows the spring and summer

plumes, as they are representative of their respective regimes. The fact that the plume crosses isentropic surfaces over Asia and the Western Pacific indicates that diabatic heating is an important factor in governing its transport out of the boundary layer. The summertime plume has a c-shaped profile consistent with convective lifting associated with the East Asian summertime monsoon season. The stronger lifting in the summer regime results in an O_3A plume at higher altitudes than found in the spring regime. Over East Asia, the spring plume is lifted into the lower FT (below ~6 km) and O_3A concentrations do not exceed 20 ppbv. In contrast, the model simulations suggest the plume in the summer regime is convectively lifted up to the tropopause (10-12 km) with O_3A concentrations in excess of 25 ppbv.

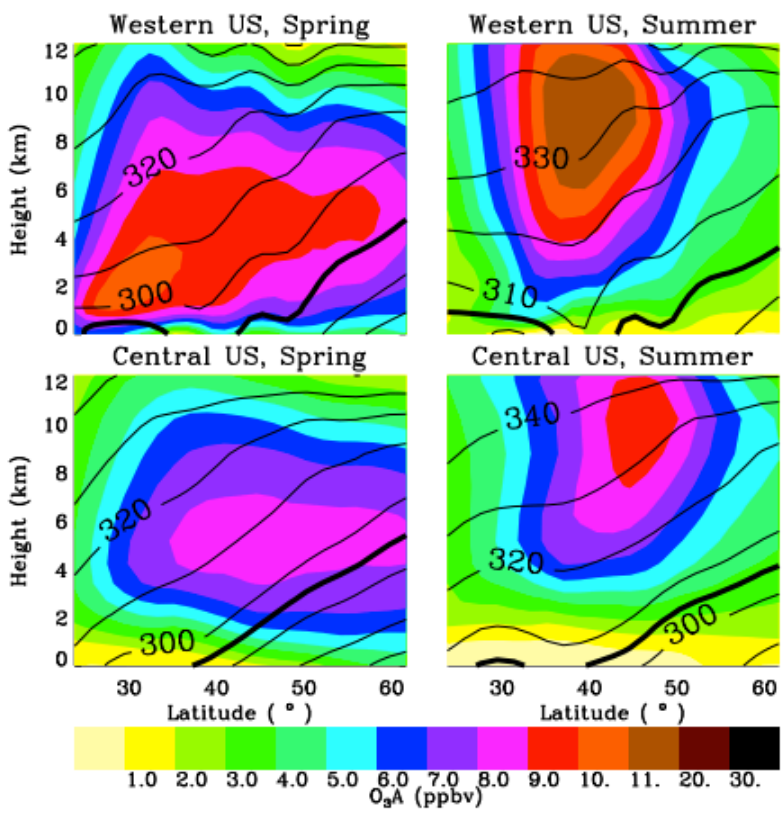

Figure 2.3: Meridional profiles of the O_3A plume as in enters US air space over the west coast (235° E) (top) and central US (260° E) (bottom) for the spring (left) and summer (right) seasons. Isentropic surfaces are also plotted (thin lines) and the thick line denotes the isentropic surface plotted in Figure 2.4.

Once in the FT, the Asian plume tend to follow isentropic surfaces in both regimes (Figure 2.2), implying isentropic transport over the Pacific. The spring O_3A plume primarily enters the NA air basin below 5 km while the summer plume enters primarily above 5 km. Figure 2.3 shows a meridional slice of the average O_3A plume as in crosses the western boundary of the US (235° E) and in the central US. Both regimes have O_3A concentrations in excess of 5 ppbv in the FT at the North American west coast, but the peak O_3A in the spring is around 10-11 ppbv and is found below 5 km while peak O_3A in the summer is around 15-20 ppbv and is found in the upper FT. In addition, O_3A in the spring at the west coast of the US is spread from 20° N to 50° N below 5 km, while O_3A in the summer is found in a tight band centered at 40° N at 8 km. By the time the O_3A plume reaches the central US, it has decreased in concentration and moved higher in altitude and farther north during both seasons.

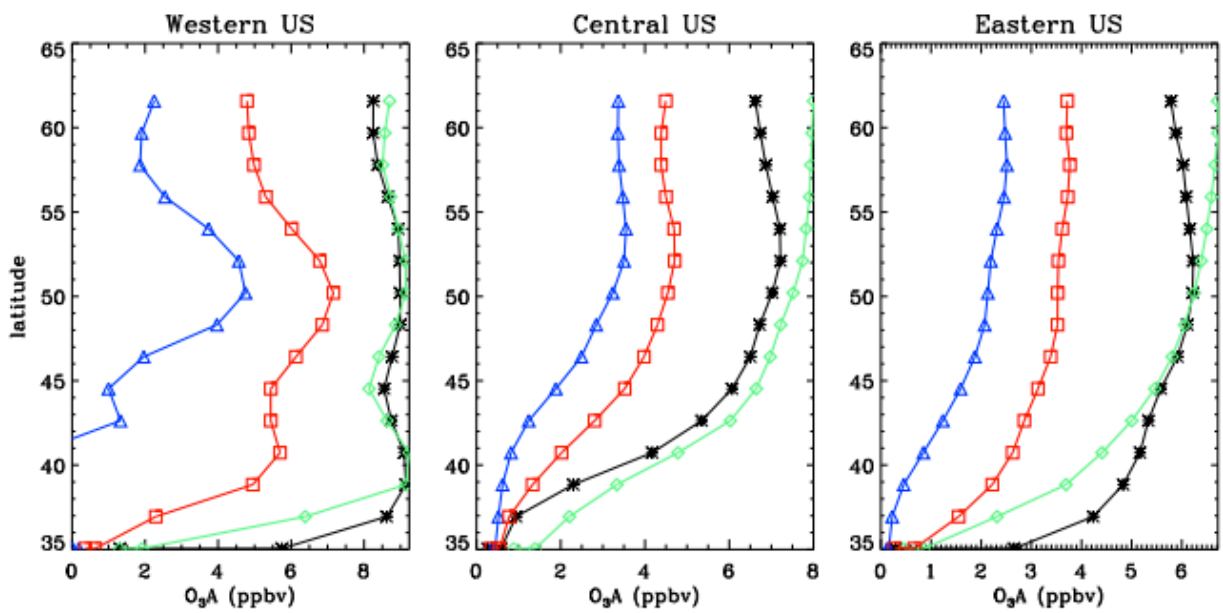

Figure 2.4: O_3A concentrations following isentropic surfaces that intersect the surface at 35° N for the western (235° E), central (260° E), and eastern (280° E) US surface at 35° N for the winter (black), spring (green), summer (blue), and autumn (red).

The impact of Asian pollution on surface ozone in the US depends on both the concentrations of O_3A over the US and the ability of meteorological events to bring the elevated concentrations in the O_3A plume down to the surface. Isentropic transport mechanisms, such as transport in the dry air stream behind cold fronts, operate primarily along isentropic surfaces, as they lack the strong diabatic heating found during precipitation events required to result in significant cross isentropic transport. Figure 2.4 shows the concentrations of O_3A along the isentropic surfaces that intersects the surface at 35° N and 235° E in the western US, 260° E in the central US, and 280° E in the eastern US. In the central US, this is the 290 K and 300 K potential temperature surface for the spring, and summer, respectfully (Figure 2.3). In the western US, this intersection is at a slightly lower potential temperature (Figure 2.3), and in the eastern US, the intersection is at a slightly higher potential temperature surface (data not shown). Therefore, at each location, this figure gives the potential O_3A concentrations available for transport to the surface isentropically. These surfaces typically rise in altitude towards the north and intercept higher O_3A concentrations at higher altitudes (see Figure 2.3). The winter (black) and spring (green) lines show that O_3A concentrations in excess of 6 ppbv in each region can be easily "tapped" by isentropic motions, while the summer (blue) and autumn (red) lines show similar isentropic transport can only tap significantly lower concentrations of O_3A. The next section examines this transport.

V. Transport to the US Boundary Layer

Table 2.2: Summary of Concentrations and Ratios for O_3A and O_3 in the Western (35°-50° N, 235°-350° E), central (30°-50° N, 250°-270° E), and eastern (35°-45° N, 270°-285° E) US Values

	O_3A (ppb)				O_3 (ppb)				O_3A/O_3 (%)		
	surface	BL	FT	%BL	surface	BL	FT	%BL	surface	BL	FT
					Western US						
DJF	2.45 ± 1.0	6.89 ± 2.1	9.88 ± 2.0	41.1%	32.0 ± 5.3	59.0 ± 6.3	82.6 ± 10	41.7%	7.7%	11.7%	12.0%
MAM	3.36 ± 1.3	6.55 ± 2.3	11.1 ± 2.0	37.1%	37.4 ± 3.5	63.2 ± 5.5	85.0 ± 9.0	42.6%	9.0%	10.4%	13.1%
JJA	1.36 ± 0.7	2.43 ± 1.2	10.7 ± 2.8	18.5%	39.0 ± 4.8	63.6 ± 8.4	76.9 ± 6.8	45.3%	3.5%	3.8%	13.9%
SON	1.70 ± 0.9	3.85 ± 2.1	11.0 ± 2.8	25.9%	32.9 ± 4.6	57.6 ± 6.3	74.1 ± 6.6	43.7%	5.2%	6.7%	14.8%
					Central US						
DJF	1.14 ± 0.4	3.39 ± 1.1	7.73 ± 1.6	30.5%	29.4 ± 5.7	53.7 ± 6.7	74.7 ± 7.0	41.8%	3.9%	6.3%	10.3%
MAM	1.66 ± 0.5	3.28 ± 1.0	8.23 ± 1.5	28.5%	40.0 ± 4.1	67.7 ± 6.4	77.7 ± 6.3	46.6%	4.2%	4.8%	10.6%
JJA	0.70 ± 0.3	1.22 ± 0.6	6.97 ± 2.1	14.9%	47.1 ± 5.2	78.4 ± 9.0	75.6 ± 5.5	50.9%	1.5%	1.6%	9.2%
SON	0.81 ± 0.3	1.82 ± 0.9	7.97 ± 1.9	18.6%	33.9 ± 7.7	59.5 ± 11	68.5 ± 5.4	46.5%	2.4%	3.1%	11.6%
					Eastern US						
DJF	0.38 ± 0.2	1.66 ± 0.9	8.29 ± 2.0	16.7%	22.5 ± 6.8	46.6 ± 8.2	83.1 ± 9.3	35.9%	1.7%	3.6%	10.0%
MAM	0.56 ± 0.3	1.29 ± 0.8	8.16 ± 2.0	13.7%	46.7 ± 9.7	81.3 ± 15	89.9 ± 9.2	47.5%	1.2%	1.6%	9.1%
JJA	0.16 ± 0.1	0.32 ± 0.2	6.38 ± 1.8	4.7%	64.0 ± 8.5	109 ± 14	90.1 ± 7.3	54.6%	0.3%	0.3%	7.1%
SON	0.27 ± 0.2	0.76 ± 0.5	8.31 ± 2.4	8.3%	38.4 ± 15	69.0 ± 23	78.4 ± 7.2	46.8%	0.7%	1.1%	10.6%
					Total US						
DJF	1.37 ± 0.6	4.07 ± 1.4	8.46 ± 1.8	32.5%	28.8 ± 5.8	53.9 ± 6.9	78.6 ± 8.2	40.7%	4.8%	7.6%	10.8%
MAM	1.94 ± 0.7	3.84 ± 1.3	9.05 ± 1.7	29.8%	40.5 ± 5.0	69.0 ± 7.9	82.2 ± 7.6	45.6%	4.8%	5.6%	11.0%
JJA	0.79 ± 0.4	1.40 ± 0.7	7.94 ± 2.3	15.0%	48.0 ± 5.7	79.9 ± 9.9	78.8 ± 6.2	50.4%	1.6%	1.7%	10.1%
SON	0.96 ± 0.5	2.20 ± 1.2	8.92 ± 2.2	19.8%	34.5 ± 8.2	60.8 ± 12	72.0 ± 6.1	45.8%	2.8%	3.6%	12.4%

[a]The tropopause was set at the 210 hPa layer for all seasons, and the boundary layer (BL) height was set at 964 hPa level for the winter, 943 hPa level for the spring and autumn, and 916 hPa level for the summer (model output). Model output planetary BL height is used to differentiate the free troposphere (FT) from the BL. All concentrations are density-weighted (%BL = (BL)/(BL + FT)).

The seasonally averaged, density-weighted O_3A and O_3 concentrations for western, central, eastern, and the total US are summarized in Table 2.2. In addition, the O_3A/O_3 fraction (%) for the surface, BL, and FT are also summarized to examine the contribution of O_3A to total O_3 concentrations. These results show that in the US, total O_3 concentrations peak in the summer months at 39 ± 4.5, 47 ± 5.2, and 64.0 ± 8.5 ppbv in the western, central, and eastern US, respectfully. In the US troposphere, the highest O_3 concentrations are found in the eastern summertime BL at 109±14 ppbv, a peak noted by Cooper et al. (2007), although Murazaki and Hess (2006) shows a high O_3 bias in the eastern US in a similar model setup.

O_3A concentrations show a different seasonality. The highest O_3A concentrations are found in the western US, with the central and eastern US showing roughly 50% and 25%, respectfully, of the western US concentrations. The following features are similar in all regions:

(1) peak surface O_3A is found in the spring; (2) peak BL O_3A is found in the winter and spring; (3) minimum vertically averaged O_3A concentrations in all regions of the troposphere occur primarily in the summer; (4) the maximum Asian influence (i.e. O_3A /O_3) at the surface is found in the spring in the western and central US at 9%, 4%, and in the winter in the eastern US at 1%; and (5) the minimum Asian influence at the surface is found in the summer, with 3.5%, 1.5%, and 0.3% in the western, central, and eastern US, respectfully. Throughout the US, surface and BL O_3A concentrations show more seasonal variability than the FT O_3A concentrations, which is consistent with a year-round O_3A plume in the FT over the US. The seasonally-averaged FT O_3A results in Table 2.2 do not indicate the summertime upper free tropospheric maximum. This feature is simply not evident when averaging across the entire FT.

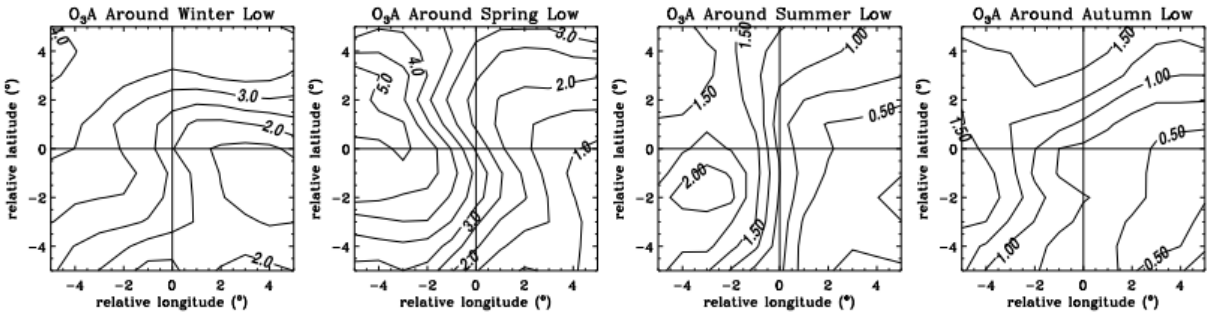

Figure 2.5: Seasonal Composites of the O_3A for the 15 most well-defined Low Systems over the central US for the each season. The crosshairs mark the center of the low pressure system, and the composites extend out 5 degrees in all directions.

Mid-latitude cyclones move over the US on a synoptic timescale of 3 – 10 days, and play a dominant role in meteorology, transport, and air quality. The center of a mid-latitude cyclone is a low-pressure system with a warm front extending eastward, and a cold front extending south and west. Ahead of the low-pressure system, the warm conveyor belt (WCB) air stream lifts surface air into the FT, while behind the low-pressure system, the dry air (DA) stream transports FT air to the surface ((Cooper at al., 2001, 2002). This paper shows that these subsident, post-

frontal air streams can "tap" free-tropospheric O_3A and impact surface O_3 concentrations, particularly in the central US where low systems are the most well-defined.

Figure 2.5 shows the surface O_3A concentrations around the low pressure centers of 15 well-defined low pressure systems in the central US for each season. For each season, there are lower O_3A concentrations ahead of the cold front (south and east of the low system) and higher O_3A concentrations behind the cold front (west and north of the low system), but this signal is most pronounced during the springtime. The total change in O_3A that occurs during the passage of the springtime cold front is around 4 ppbv. However, there is no correlation noted between the strength of the low pressure system and the magnitude of the O_3A increase (not shown). Total O_3 concentrations show much higher system to system variability, with a general decrease in O_3 (approximately 5 ppbv for the 15 well-defined low systems) during the passage of the cold front (data not shown). However, the daily variability is high, and no clear pattern is discernible.

VI. O_3A Signal Decomposition

The differences between various tracers (See Table 2.1) highlight the different mechanisms which determine the budget of O_3A over the U.S. The following equation divides the total O_3A into three distinct signals:

$$O_3A = [S*O_3AtrCS] + [O_3Atr - S*O_3AtrCS] + [O_3A - O_3Atr] \qquad (1)$$

The three terms on the right hand side represent: (1) the transport of an inert tracer with a specified concentration over East Asia to the US (baseline), scaled to the annually averaged O_3A concentrations over East Asia; (2) the impact of the seasonal variations in the concentration of this tracer over East Asia, including seasonal variations in the height distribution (seasonality); (3) the net chemistry that occurs between the defined Asian source region and the U.S. (net

chemistry). The sum of the baseline and seasonality signals is equal to the O_3Atr tracer, and the sum of all three signals returns the total O_3A tracer.

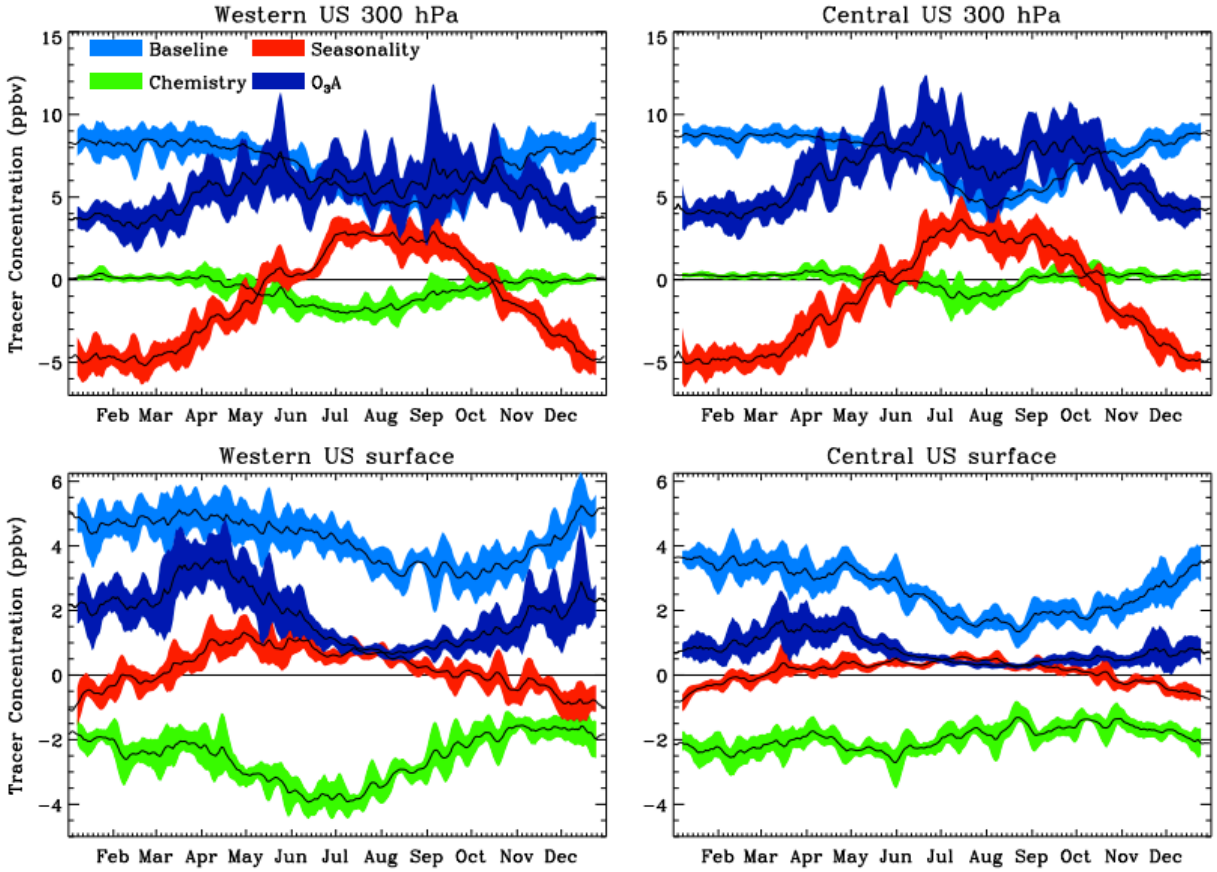

Figure 2.6: O_3A Signal Decomposition for the western (35°-50° N, 235°-350° E) and central (30°-50° N, 250°-270° E) US at the 300 hPa layer (top) and surface (bottom). The signals are plotted with their moving weekly averaged single standard deviations. O_3A is plotted in dark blue, the baseline signal in light blue, seasonality in red, and net chemistry in green (see Equation 1).

Figure 2.6 compares these three signals along with the total O_3A concentrations for the 2001 – 2005 composite years in the western and central US at 300 hPa (top) and at the surface (bottom). These values are 5-year composite averages with the 1 standard deviation of the moving weekly averages shown in the shaded outlines. At the surface in both regions, there are high standard deviations in the spring and winter, with relatively low standard deviations in the

summer. In addition, the 300 hPa layer shows high standard deviations during the summertime, which is consistent with high O_3A plumes advecting through on a weekly time scale.

Total O_3A shows strong variation at the surface for both regions, with a peak in the spring and a minimum in the summer. The peak in the springtime (4 ppbv in the west, and 2 ppbv in the central US) at the surface can be explained by examining the contributions from all the three signals. During the spring months the baseline signal is near its maximum, indicating the most robust transport of East Asian air to North America occurs during spring. The seasonality signal is nearly maximum in the spring months, indicating that there are high concentrations of O_3A in the source region over East Asia which can be transported to the US. Net chemistry, which reflects both chemical ozone production from East Asian ozone precursors and chemical loss en route, tends to be negative for all seasons for surface air. However, net chemistry has a broad seasonal maximum between October and April, suggesting minimal ozone destruction during these months. These three factors contribute to the O_3A maximum in the springtime. One major difference in the central US is that the net chemical signal shows significantly less seasonal variation than is seen in the western US.

Similarly, the summertime surface minimum in both regions can be explained by again decomposing the O_3A concentrations into the three signals. In the summertime, the baseline signal is nearly at its minimum, implying less robust transport from East Asia to North America. The seasonality signal is still at its maximum, but starts to decrease slightly in the late summer. And finally, the net chemistry signal is at its maximum net destruction; nearly double that than found in the springtime. While this strong net negative chemistry signal is not seen in the central US, the other two signals still account for the summertime O_3A minimum. The seasonal variation of the 300 hPa chemistry signal is flatter with a broad winter-spring maximum. At 300 hPa the

chemistry signal plays a much smaller role, with the baseline and seasonality dominating the O_3A signal.

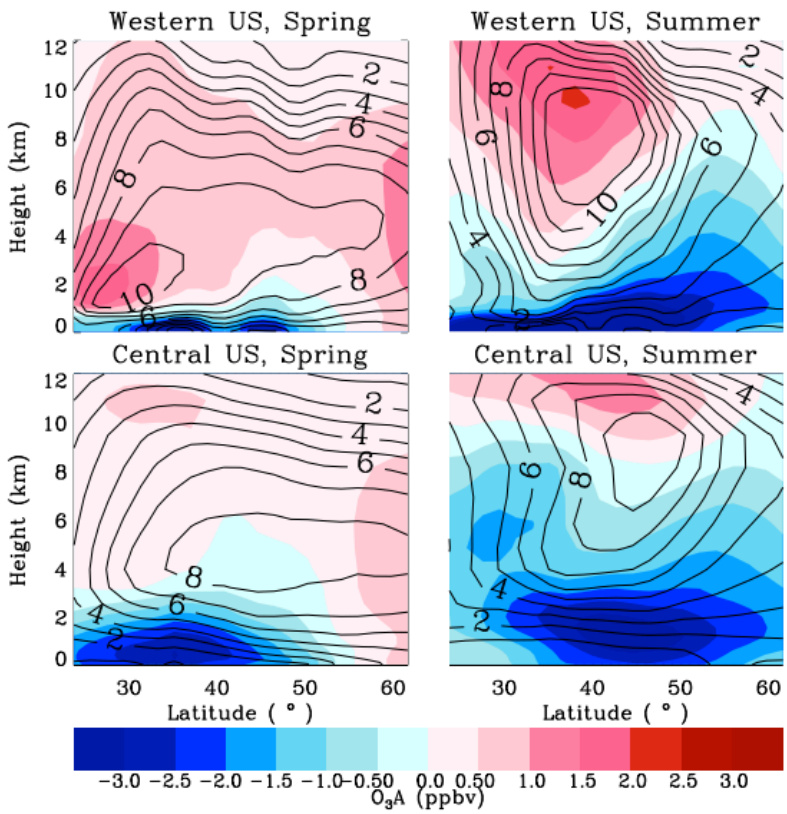

Figure 2.7: Net chemistry signal for the same composites as in Figure 2.3. See Section 6 for description of this signal. The left figures are for the west coast of the US, and the right figures are for central US. Color contours are the net chemistry signal, and line contours are O_3A concentrations.

Figure 2.7 examines the net chemistry of the plumes more closely by plotting the net chemistry signal for the same meridional slices as in Figure 2.3. This figure demonstrates: (1) net destruction in the US BL during every season, (2) net chemical production in the FT in the springtime; (3) modest net chemical production in the FT in the western US and modest net chemical destruction in the eastern US during the summertime, (4) and a tight band of large chemical production in the upper FT in the summertime, especially in the western US. This tight band is limited to the upper free troposphere, as the much of the BL and lower FT shows

predominant net chemical destruction during the summertime. Fiore et al. (2002) notes low background O_3 contributions during peak total O_3 events in the summer, as strong photochemical cycling destroys much of the background O_3 while producing high concentrations of total O_3. The results from this study show strong net chemical destruction of O_3A in the BL, which is consistent with Fiore et al. (2002) in that summertime high O_3 originates locally rather than from background sources. The spring and autumn seasons show similar net chemistry signals, but both are relatively minor (within ± 1.0 ppbv of zero throughout most of the troposphere). The western US shows higher O_3A concentrations in the FT and parts of the BL, while the central US shows net O_3A destruction throughout the BL and lower FT in the summer.

VII. Comparisons to Other Studies

Table 2.3: Comparison of contribution of surface O_3 in North America from East Asia to other studies

	HTAP results	Results from this study**
DJF	0.82	2.29±0.41
MAM	0.99	2.35±0.56
JJA	0.48	0.70±0.31
SON	0.69	1.19±0.53
Annual	0.75	1.63±0.45

*: from HTAP results for North American ozone change with 20% decrease in NOx, scaled by 5

**: mean ± interannual variability of tagged Asian ozone (O3A) from 2001 – 2005.

Table 2.3 summarizes results from HTAP (results from archived HTAP data with similar model version and set up as this study's simulation) and the results from this study, which were both obtained utilizing similar simulations. In this comparison the HTAP results are O_3 changes over North America in response to 20% reductions of East Asian emissions scaled by a factor of 5, while the results from this study are the average O_3A concentrations over North America. Pfister et al. (2006) used this same tagging method with MOZART-4 chemistry to look at O_3 production during North American forest fires, and found that NO_x-O_3 non-linearity was

strongest near source regions, but far from source regions tagged NO_x gives almost the same concentration of tagged O_3 as turning off the emissions in the source region. Wu et al. (2009) examined the differences in this NO_x-O_3 non-linearity by decreasing NO_x emissions by 20% and 100%, found that non-linearities were strongest in the spring, and that 100% reductions in NO_x emissions always resulted in larger O_3 responses than a 20% reduction of NO_x emissions scaled by a factor of 5. This complicates comparisons between the HTAP results and the results from this study in Table 2.3. In general, this study shows approximately 2 – 2.5 times the East Asian influence on North American ozone than the HTAP results in the winter and spring, and roughly double the HTAP results in the summer and autumn.

VIII. Discussion and Conclusion

The import of Asian pollutants into the western US, and particularly the Pacific coast, has been extensively studied as this region of the US is most impacted by Asian emissions (O_3A makes up around 10% of total surface O_3). The eastern US is strongly impacted by interactions with air from the Atlantic Ocean and the Gulf of Mexico, and shows very strong O_3A net chemical destruction in the BL, and therefore has very small (around 1%) Asian influence at the surface. This paper shows simulation results from all three regions, but focuses primarily on the central US to gain insight into the impact of mid-latitude cyclones on transporting Asian O_3 to the surface of the US as this region is most conducive to frequent and well-defined mid-latitude cyclones.

Transport of O_3A and its precursors to the surface of the US depends on the structure of the elevated O_3A plume and the available meteorological transport mechanism that can tap the plume and bring it to the surface. This study has shown that the highest O_3A concentrations are found in the summer regime plume, but these concentrations are centered in a tight plume in the

upper free troposphere. In contrast, while the spring regime plume has generally lower concentrations, they are found lower in the free troposphere, and occasionally in the BL (Figure 2.3).

The summertime peak in O_3A concentrations in the FT of the US result from the transport signal being the dominant signal in the summertime, with the seasonality and net chemistry signals are comparatively small. Enhanced convection over East Asia during the summertime lofts O_3A and its precursors higher into the FT, which are then transported over the Pacific in the dominant midlatitude westerlies. However, summertime net chemical destruction in the BL and lower FT in the US keep O_3A concentrations low. In contrast, weaker convection over East Asia in the spring results in lifting of O_3A and its precursors to the lower FT, allowing meteorological mechanisms to more easily tap O_3A during the spring, even though there are generally lower O_3A concentrations. Figure 2.5 shows enhanced O_3A concentrations behind cold fronts during all seasons in the central US, with the highest concentrations in the springtime. Overall, surface O_3A concentrations show a summertime low and a springtime peak, in contrast to total O_3 concentrations, which show a summertime peak.

In this study, we have shown that springtime O_3A enters the US air basin widely dispersed in the FT (2 – 6 km from 30-50°N) with a seasonally averaged peak of 10.0 ppbv (30°N at 2 km) and that summertime O_3A enters the US air basin in the upper FT (6 – 12 km) tightly centered on a higher peak of 12.0 ppbv (40°N at 8 km) but with a lower average of 6.0±1.0 ppbv (Figure 2.3). However, surface O_3A concentrations in the western US (240°E) show a springtime maximum of 3.5 ± 1.0 ppbv (with daily peaks reaching 10.0 ppbv) and a summertime minimum of 1.0 ± 0.25 ppbv. The remainder of the US shows a similar pattern but with lower O_3A concentrations. The springtime peak is in contrast to higher O_3A concentrations over East Asia in

the summertime. This surface springtime maximum and summertime minimum can be explained by: (1) the O_3A plume entering US airspace in the lower free troposphere, while the summertime O_3A plume enters in the upper free troposphere; (2) mechanisms that transport free tropospheric air to the surface of the US can "tap" higher O_3A concentrations during the springtime; and (3) higher O_3A destruction during transport to the surface of the US in the summertime. This pattern is in contrast to total O_3 concentrations which show a summertime peak. This implies that, while O_3A will still exacerbate summertime ozone peaks, the larger Asian impact on surface ozone in the US will be in the off-peak springtime.

IX. Acknowledgements

The authors would like to thank the National Science Foundation (NSF) and National Center for Atmospheric Research (NCAR) for the computer time to run these simulations, as well as Francis Witt for his help with the chemical mechanism. We would also like to thank NASA (Project Number 386H956) for the initial funding for this project, as well as EPA (Project Number RD-83428301-0) for additional funding.

X. References

Browning, K. A., and N. M. Roberts (1994), Structure of a frontal cyclone, *Quarterly Journal of the Royal Meteorological Society*, *120*(520), 1535-1557, doi:10.1002/qj.49712052006.

Cooper, O. R. et al. (2004), A case study of transpacific warm conveyor belt transport: Influence of merging airstreams on trace gas import to North America, *J. Geophys. Res, 109*(D23S08), doi:10.1029/2003JD003624.

Cooper, O. R., J. L. Moody, D. D. Parrish, M. Trainer, T. B. Ryerson, J. S. Holloway, G. Hübler, F. C. Fehsenfeld, and M. J. Evans (2002), Trace gas composition of midlatitude cyclones over the western North Atlantic Ocean: A conceptual model, *J. Geophys. Res.*, *107(*4056), doi:200210.1029/2001JD000901.

Cooper, O. R., J. L. Moody, D. D. Parrish, M. Trainer, T. B. Ryerson, J. S. Holloway, G. Hübler, F. C. Fehsenfeld, S. J. Oltmans, and M. J. Evans (2001), Trace gas signatures of the airstreams within North Atlantic cyclones: Case studies from the North Atlantic Regional Experiment (NARE '97) aircraft intensive, *J. Geophys. Res., 106*(D6) 5437-5456, doi:10.1029/2000JD900574.

Cooper, O. R. et al. (2010), Increasing springtime ozone mixing ratios in the FT over western North America, *Nature*, *463*(7279), 344-348, doi:10.1038/nature08708.

Cooper, O. R. et al. (2005), A springtime comparison of tropospheric ozone and transport pathways on the east and west coasts of the United States, *J. Geophys. Res., 110*(D05S90), doi:10.1029/2004JD005183.

Cooper, O. R. et al. (2007), Evidence for a recurring eastern North America upper tropospheric ozone maximum during summer, *J. Geophys. Res.*, *112*(D23304), doi:10.1029/2007JD008710.

Crawford, J. H. et al. (2004), Relationship between Measurements of Pollution in the Troposphere (MOPITT) and in situ observations of CO based on a large-scale feature sampled during TRACE-P, *J. Geophys. Res.*, *109*(D15S04), doi:200410.1029/2003JD004308.

Emmons, L. K. et al. (2010), Description and evaluation of the Model for Ozone and Related chemical Tracers, version 4 (MOZART-4), *Geosci. Model Dev.*, *3*(1), 43-67, doi:10.5194/gmd-3-43-2010.

Fiore, A., D. J. Jacob, H. Liu, R. M. Yantosca, T. D. Fairlie, and Q. Li (2003), Variability in surface ozone background over the United States: Implications for air quality policy, *J. Geophys. Res.*, *108*(D24), 4787, doi:10.1029/2003JD003855.

Fiore, A. M. et al. (2009), Multimodel estimates of intercontinental source-receptor relationships for ozone pollution, *J. Geophys. Res.*, *114*(D04301), doi: 10.1029/2008JD010816

Fiore, A. M., D. J. Jacob, R. M. Yantosca, B. D. Field, A. C. Fusco, J. G. Wilkinson, and I. Bey (2002), Background ozone over the United States in summer: Origin, trend, and contribution to pollution episodes, *J. Geophys. Res., 107*(4275), doi:10.1029/2001JD000982.

Goldstein, A. H., D. B. Millet, M. McKay, L. Jaeglé, L. Horowitz, O. Cooper, R. Hudman, D. J. Jacob, S. Oltmans, and A. Clarke (2004), Impact of Asian emissions on observations at Trinidad Head, California, during ITCT 2K2, *J. Geophys. Res.*, *109*(D23S17), doi:200410.1029/2003JD004406.

Hannan, J. R., H. E. Fuelberg, J. H. Crawford, G. W. Sachse, and D. R. Blake (2003), Role of wave cyclones in transporting BL air to the FT during the spring 2001 NASA/TRACE-P experiment, *J. Geophys. Res., 108*(8785), doi:10.1029/2002JD003105.

Hess, P. G., and T. Vukicevic (2003), Intercontinental transport, chemical transformations, and baroclinic systems, *J. Geophys. Res.*, *108*(4354), doi:200310.1029/2002JD002798.

Hess, P. G., and J. Lamarque (2007), Ozone source attribution and its modulation by the Arctic oscillation during the spring months, *J. Geophys. Res., 112*(D11303), doi:10.1029/2006JD007557.

Hoell, J. M., D. D. Davis, S. C. Liu, R. E. Newell, H. Akimoto, R. J. McNeal, and R. J. Bendura (1997), The Pacific Exploratory Mission-West Phase B: February-March, 1994, *J. Geophys. Res.*, *102*(D23),28223-28239, doi:199710.1029/97JD02581.

Holzer, M., and T. M. Hall (2007), Low-level transpacific transport, *J. Geophys. Res.*, *112*(D09103), doi:200710.1029/2006JD007828.

Husar, R. et al. (2001), Asian dust events of April 1998, *J. Geophys. Res., 106*(D16), 18317-18330, doi: 10.1029/2000JD900788.

Jacob, D. J., J. H. Crawford, M. M. Kleb, V. S. Connors, R. J. Bendura, J. L. Raper, G. W. Sachse, J. C. Gille, L. Emmons, and C. L. Heald (2003), Transport and Chemical Evolution over the Pacific (TRACE-P) aircraft mission: Design, execution, and first results, *J. Geophys. Res.*, *108*(9000), doi:200310.1029/2002JD003276.

Jacob, D. J., J. A. Logan, and P. P. Murti (1999), Effect of rising Asian emissions on surface ozone in the United States, *Geophys. Res. Lett.*, *26*(14), 2175-2178, doi:10.1029/1999GL900450.

Jaffe, D. et al. (1999), Transport of Asian air pollution to North America, *Geophys. Res. Lett., 26*(6), 711-714, doi:10.1029/1999GL900100.

Jaffe, D., H. Price, D. Parrish, A. Goldstein, and J. Harris (2003), Increasing background ozone during spring on the west coast of North America, *Geophys. Res. Lett.*, *30*(1613), doi:200310.1029/2003GL017024.

Jonson, J. E. et al. (2010), A multi-model analysis of vertical ozone profiles, *Atmospheric Chemistry & Physics*, *10*, 5759-5783, doi:10.5194/acp-10-5759-2010.

Lamarque, J. and P. Hess, Cross-Tropopause Mass Exchange and Potential Vorticity Budget in a Simulated Tropopause Folding, *J. Atm. Sci., 50*(15), 2246-2269.

Lamarque, J., P. Hess, L. Emmons, L. Buja, W. Washington, and C. Granier (2005), Tropospheric ozone evolution between 1890 and 1990, *J. Geophys. Res., 110*(D08304), doi:10.1029/2004JD005537.

Liang, Q. et al. (2007), Summertime influence of Asian pollution in the FT over North America, *J. Geophys. Res., 110*(D08304), doi:10.1029/2004JD005537.

Liang, Q., L. Jaeglé, D. A. Jaffe, P. Weiss-Penzias, A. Heckman, and J. A. Snow (2004), Long-range transport of Asian pollution to the northeast Pacific: Seasonal variations and transport pathways of carbon monoxide, *J. Geophys. Res., 109*(D23S07), doi:10.1029/2003JD004402.

Liu, H., D. J. Jacob, I. Bey, R. M. Yantosca, B. N. Duncan, and G. W. Sachse (2003), Transport pathways for Asian pollution outflow over the Pacific: Interannual and seasonal variations, *J. Geophys. Res., 108*(8786), doi:10.1029/2002JD003102.

Mari, C., M. J. Evans, P. I. Palmer, D. J. Jacob, and G. W. Sachse (2004), Export of Asian pollution during two cold front episodes of the TRACE-P experiment, *J. Geophys. Res., 109*(D15S17), doi:10.1029/2003JD004307.

Murazaki, K., and P. Hess (2006), How does climate change contribute to surface ozone change over the United States?, *J. Geophys. Res., 111*(D05301), doi:10.1029/2005JD005873.

Ohara, T., H. Akimoto, J. Kurokawa, N. Horii, K. Yamaji, X. Yan, and T. Hayasaka (2007), An Asian emission inventory of anthropogenic emission sources for the period 1980-2020, *Atmos. Chem. Phys. Dis.*, *7*, 6843-6902.

Parrish, D. D. et al. (2004), Changes in the photochemical environment of the temperate North Pacific troposphere in response to increased Asian emissions, *J. Geophys. Res., 109*(D23S18), doi:10.1029/2004JD004978.

Pfister, G. G. et al. (2006), Ozone production from the 2004 North American boreal fires, *J. Geophys. Res., 111*, doi:10.1029/2006JD007695.

Shindell, D. T. et al. (2008), A multi-model assessment of pollution transport to the Arctic, *Atmos. Chem. Phys.*, *8*, 5353-5372, doi:10.5194/acp-8-5353-2008.

Singh, H. B., W. H. Brune, J. H. Crawford, F. Flocke, and D. J. Jacob (2009), Chemistry and transport of pollution over the Gulf of Mexico and the Pacific: spring 2006 INTEX-B campaign overview and first results, *Atmos. Chem. Phys.*, *9*(7), 2301-2318, doi:10.5194/acp-9-2301-2009.

Stohl, A., S. Eckhardt, C. Forster, P. James, and N. Spichtinger (2002), On the pathways and timescales of intercontinental air pollution transport, *J. Geophys. Res.*, *107*(4684), doi:200210.1029/2001JD001396.

Streets, D. G. et al. (2003), An inventory of gaseous and primary aerosol emissions in Asia in the year 2000, *J. Geophys. Res.*, *108*(8809), doi:200310.1029/2002JD003093.

Tang, Y. et al. (2004), Multiscale simulations of tropospheric chemistry in the eastern Pacific and on the U.S. West Coast during spring 2002, *J. Geophys. Res., 109*(D23S11), doi:10.1029/2004JD004513.

Wang, Y., Y. Choi, T. Zeng, B. Ridley, N. Blake, D. Blake, and F. Flocke (2006), Late-spring increase of trans-Pacific pollution transport in the upper troposphere, *Geophys. Res. Lett., 33*(L01811), doi:10.1029/2005GL024975.

Weiss-Penzias, P., D. A. Jaffe, P. Swartzendruber, J. B. Dennison, D. Chand, W. Hafner, and E. Prestbo (2006), Observations of Asian air pollution in the FT at Mount Bachelor Observatory during the spring of 2004, *J.Geoph. Res., 111*(D10304), doi:10.1029/2005JD006522.

Wu, S., B. N. Duncan, D. J. Jacob, A. M. Fiore, and O. Wild (2009), Chemical nonlinearities in relating intercontinental ozone pollution to anthropogenic emissions, *Geophys. Res. Lett.*, *36*(L05806), doi:200910.1029/2008GL036607.

Yienger, J. J., M. Galanter, T. A. Holloway, M. J. Phadnis, S. K. Guttikunda, G. R. Carmichael, W. J. Moxim, and H. L. II (2000), The episodic nature of air pollution transport from Asia to North America, *J. Geophys. Res., 105*(D22), doi:10.1029/2000JD900309.

Zhang, L. et al. (2008), Transpacific transport of ozone pollution and the effect of recent Asian emission increases on air quality in North America: an integrated analysis using satellite, aircraft, ozonesonde, and surface observations, *Atmos. Chem. Phys., 8,* 6117-6136, doi:10.5194/acp-8-6117-2008.

Zhang, Q. et al. (2009), Asian emissions in 2006 for the NASA INTEX-B mission., *Atmos. Chem. Phys., 9,* 5131-5153, doi:10.5194/acp-9-5131-2009.

XI. APPENDIX (INCLUDING SUPPLEMENTAL MATERIAL)

In addition to the model assessment studies referenced in this paper [Fiore et al., 2009; Jonson et al, 2010; Shindell et al., 2008; HTAP, 2010], this supplement compares available observations with simulation results from 2001–2005. We limit our analysis to the troposphere (below roughly 200 hPa) since this study is primarily interested in tropospheric O3. Comparisons to surface mixing ratios are done using data from the Environmental Protection Agency's (EPA) Clean Air Status and Trends Network (CASTNET) [available at java.epa.gov/castnet], while free tropospheric mixing ratios are taken from the World Ozone and Ultraviolet Radiation Data Centre (WOUDC) [available at www.woudc.org]. Limited ozonesonde measurements during this time period limit our ability to compare throughout the study region over from 2001–2005, but the included comparisons provide sufficient information to make a general comparison.

Figure S1 marks the locations of the observations, labeled according to the CASTNET and WOUDC classifications. Figure S2 compares 2001–2005 model output to surface observations at 10 sites in the US, with 2 in the western US, 2 in the central US, and 6 in the eastern US, with an average model bias of +1.2 ppbv, –3.5 ppbv, and +10.6 ppbv, respectively. At the surface, the model generally overpredicts O3 mixing ratios, particularly in the eastern US in the summertime. The model captures the five-year seasonal cycle reasonably well, with an R-value greater than 0.60 for all but 1 site, and greater than 0.75 at 6 of the 10 sites (Figure S1). Figure S3 compares the average daily diurnal cycle in the spring and summer seasons at 4 sites in the eastern and central US. The model is reasonably accurate over the central US sites (average bias of –4.3 ppbv and +0.52 ppbv in the spring and summer, respectively) but shows a strong positive bias in the eastern US (with an average bias greater than +9.7 ppbv and +14.7 ppbv for the spring and summer, respectively). This strong positive bias in the eastern US is well

documented [Fiore et al., 2008; Liu et al., 2008; Murazaki and Hess, 2006; Pfister et al., 2008] in other model simulations. Some possible sources of error include overestimations of emissions, heterogeneity of sources and observations sites within the coarse grid boxes [Wild and Prather, 2006], and land-sea circulations.

Despite the high O_3 bias at the surface, the model is more accurate in the free troposphere between 800 and 400 hPa in the eastern US. Figure S4 shows 2001–2005 monthly values for both model and ozonesonde observations at two sites, with negative biases between –4.4 ppbv and –7.6 ppbv. The model does not capture the seasonal variation as well as it does at the surface with R-values between 0.14 and 0.62.

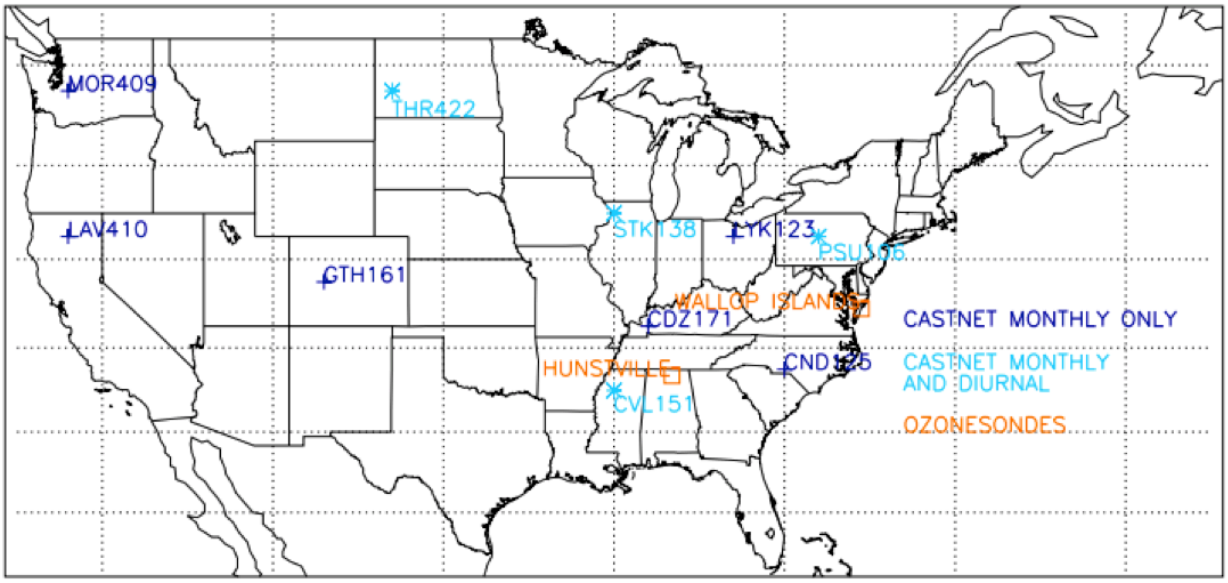

Figure S2.1. Locations of sites used for the comparisons to observations, labeled according to the CASTNET and WOUDC classifications.

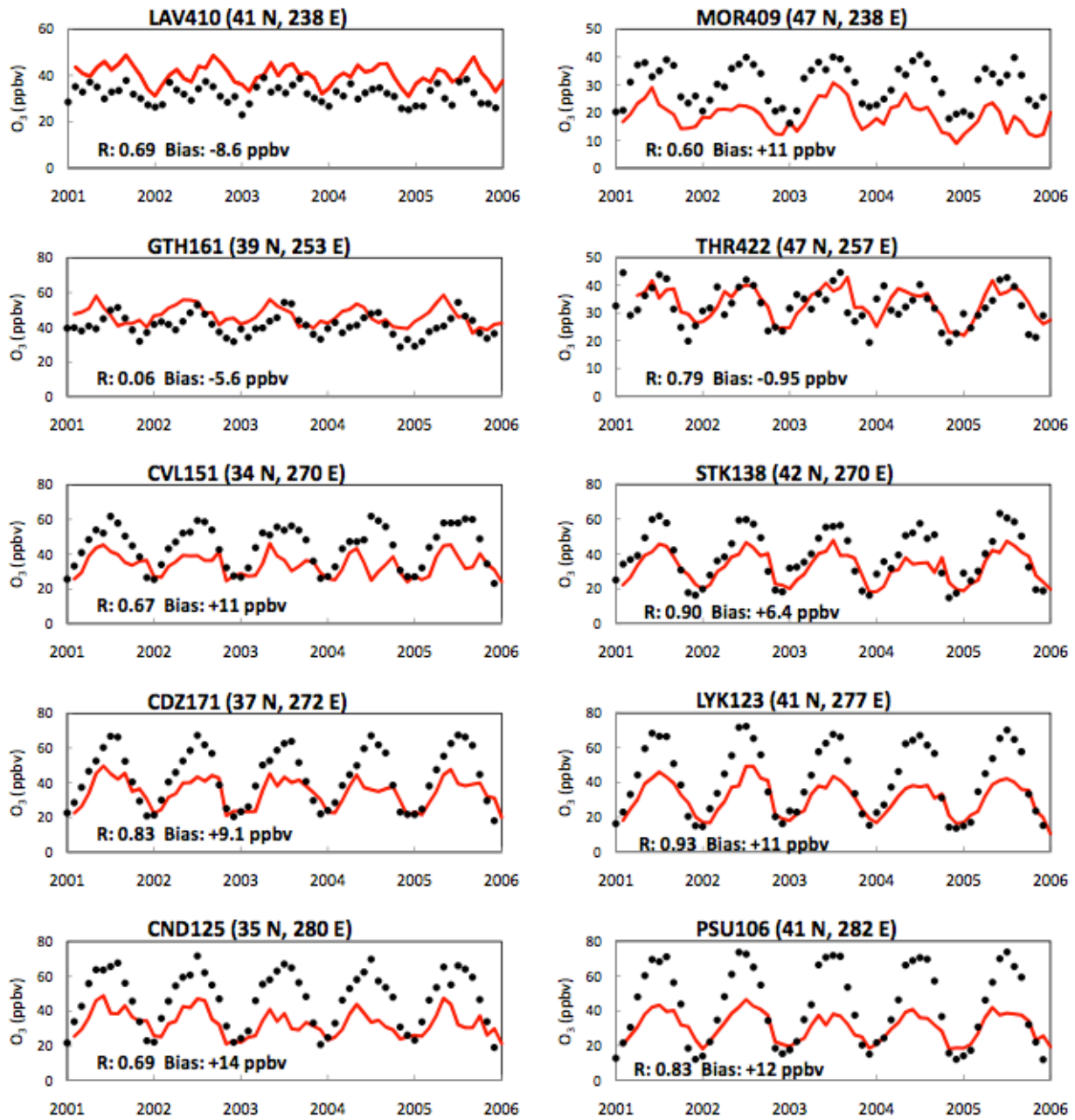

Figure S2.2. Comparison of monthly O_3 averages for 2001-2005 of the modeled output and observations for 10 CASTNET sites.

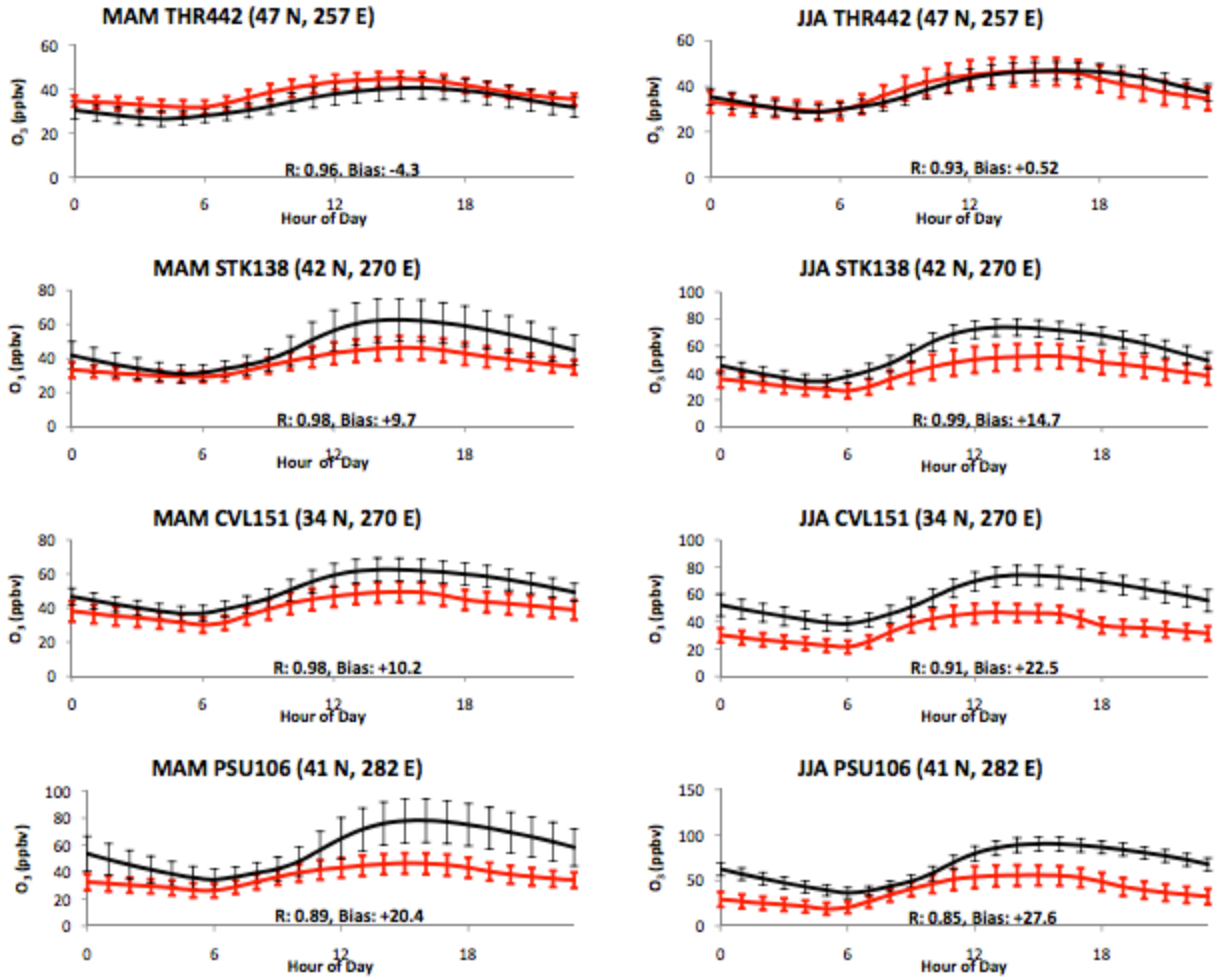

Figure S2.3. Comparison of the average daily O_3 diurnal cycle in the spring and summer of modeled output and observed data.

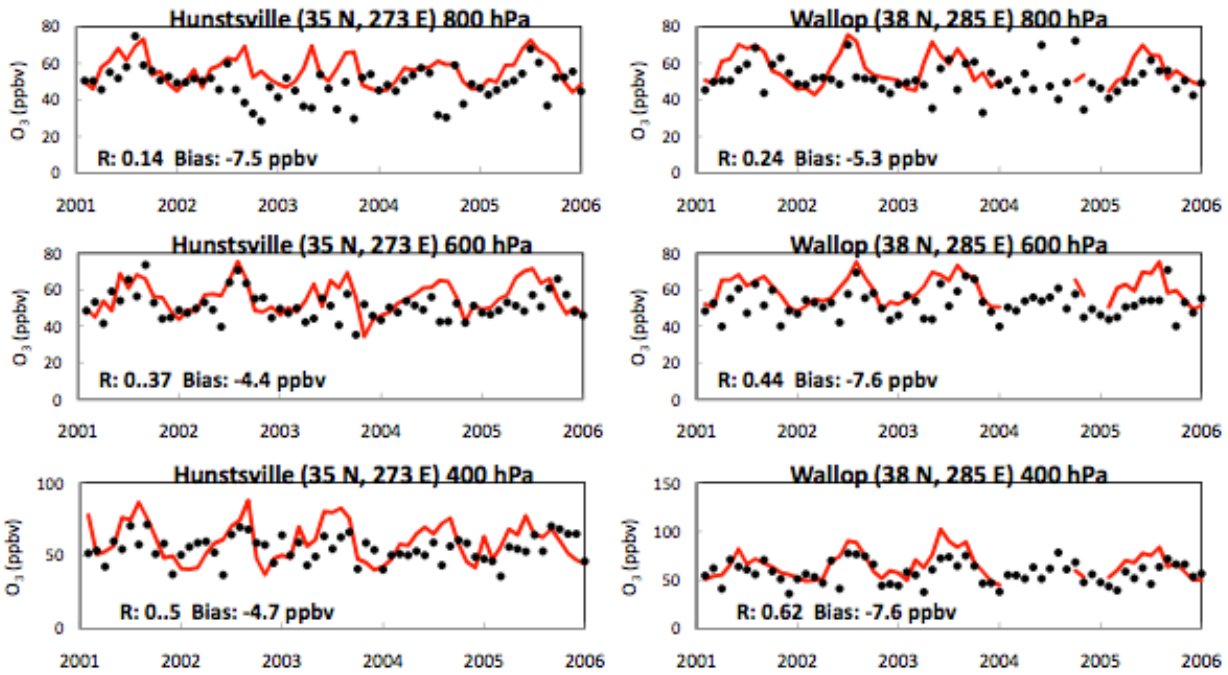

Figure S4. Comparison of O_3 mixing ratios at 800, 600, and 400 hPa layers of modeled output and observations at two sites.

CHAPTER 3: ON THE CAPABILITIES AND LIMITATIONS OF GCCM SIMULATIONS OF SUMMERTIME REGIONAL AIR QUALITY: A DIAGNOSTIC ANALYSIS OF OZONE AND TEMPERATURE SIMULATIONS IN THE US USING CESM CAM-CHEM

B. Brown-Steiner, P.G. Hess, M. Y. Lin

Published in Atmospheric Environment, Volume 101, pp. 134-148, 2015.

I. ABSTRACT

We conduct a diagnostic analysis of ozone chemistry simulated by four different configurations of a Global Climate-Chemistry Model (GCCM), the Community Earth System Model (CESM) with detailed tropospheric chemistry. The purpose of this study is to evaluate the ability of GCCMs to simulate future ozone chemistry by evaluating their ability to simulate present-day chemistry. To address this we chose four configurations of the CESM that differ in their meteorology (analyzed versus simulated meteorological fields), number of vertical levels, and the coupling of the ice and ocean models. We apply mixed model statistics to evaluate these different configurations against CASTNET ozone observations within different regions of the US by using various performance metrics relevant to evaluating future ozone changes. These include: mean biases and interannual variability, the ozone response to emission changes, the ozone response to temperature changes and ozone extreme values. Using these metrics, we find that although the configuration using analyzed meteorology best simulates temperatures it does not outperform a configuration with simulated meteorology in other metrics. All configurations are unable to capture observed ozone decreases and the ozone north-south gradient over the eastern US during 1995-2005. We find that the configuration with simulated meteorology with 56 vertical levels is markedly better in capturing observed ozone-temperature relationships and extreme values than a configuration that is identical except that it contains 26 vertical levels. We recommend caution in the use of GCCMs in simulating surface chemistry as differences in a

variety of model parameters have a significant impact on the resulting chemical and climate variables. Isoprene emissions depend strongly on surface temperature and the resulting ozone chemistry is dependent on isoprene emissions but also on cloud cover, photolysis, the number of vertical levels, and the choice of meteorology. These dependencies must be accounted for in the interpretation of GCCM results.

II. Introduction

General Circulation Models (GCMs) like the Community Earth Systems Model (CESM) are constantly evolving models with genealogies stretching back several decades (Masson and Knutti, 2011). Global Climate-Chemistry Models (GCCMs), such as the CESM Community Atmosphere Model with Chemistry (CAM-Chem) (Lamarque et al., 2012, hereafter referred to as L2012), are comparatively recent advancements with their genealogical roots stretching back only to the chemical transport models (CTMs) of the 1990s (Rasch et al., 1997, Brasseur et al., 1998, Hauglestaine et al., 1998, Emmons et al., 2010 (hereafter referred to as E2010)). Consequently, much of the framework upon which GCCMs operate has been designed, parameterized, and tuned towards the domain of GCMs (e.g. the simulation of surface air temperature, precipitation, sea level pressure, top-of-atmosphere radiative balance) rather than a domain more appropriate for GCCMs (e.g. the simulation of the chemical composition of the atmosphere) (Räisänen, 2007, Mauritsen et al., 2012). Generally, model framework and design are intended to reproduce physical aspects of a known climate by combining physical theory, observational evidence, and results from other models (Mauristen et al., 2012). Invariably this necessitates making a sequence of choices that ultimately influence the behavior of the model (Räisänen, 2007) and its chemistry. While GCCMs are able to simulate synoptic meteorological patterns that impact ozone chemistry, patterns which are expected to change under a warming

climate (Weaver et al., 2009, Doherty et al., 2013), it is becoming increasingly clear that the highly localized, rapid, and non-linear nature of atmospheric chemistry and dynamics provide a challenge in simulations of atmospheric chemistry (Wild and Prather, 2006). Out of necessity GCCMs must be used to predict ozone and other air pollutants and precursors under future climate scenarios. In an effort to evaluate the ability of GCCMs to simulate future chemical conditions, this study evaluates four configurations of the CESM CAM-Chem against observations: three with simulated meteorology and one driven by analyzed meteorological fields.

Ozone chemistry is harmful to plants, infrastructure, and people, and as a result ozone is a regulated pollutant with the United States Environmental Protection Agency (EPA) promulgating a National Ambient Air Quality Standard (NAAQS) of 75 ppb (for the fourth highest Daily-Maximum 8-Hour ozone value (DM8H O_3)) (US EPA, 2008). In 1998, the EPA promulgated the NO_x State Implementation Plan (SIP) Call, which called upon states in the Eastern US to reduce NO_x emissions through emissions budgeting as a means of reducing ground-level ozone exceedances (US EPA, 1998). Power plant NO_x emissions have decreased up to 50% since 1990 in the eastern US despite increases in electrical power over the same time period (Kim et al., 2006, Frost et al., 2006, Cooper et al., 2012) with a concurrent decrease in ozone exceedances (Bloomer et al., 2010), extreme ozone events (Rieder et al., 2013a) and the slope of the ozone-temperature relationship (Bloomer et al., 2009).

In the US, background levels of ground level ozone are typically 20 – 60 ppb, and are generally higher in the Western US than the Eastern US (Wang et al., 2009, Steiner et al., 2010, Chan and Vet, 2010) due in part to stronger influences from Asian emissions (Reidmiller et al., 2009, Brown-Steiner and Hess, 2011, Lin et al., 2012b) and stratospheric intrusions (Langford et

al., 2009, Lin et al., 2012a). Ozone is highly correlated with temperature within a temperature range of 295 - 312K (Dawson et al., 2007, Jacob and Winner, 2009, Steiner et al., 2010). Summertime DM8H O_3 events in the US occasionally exceed 100 ppb (e.g. Lai et al., 2012) and regularly exceed 60 ppb. The ozone production rates are largely influenced by secondary effects of increased temperatures on chemical kinetics (e.g. Murazaki and Hess, 2006, Jacob and Winner, 2009) such as an increased rate of peroxyacetylnitrate (PAN) decomposition into NO_x (Sillman and Samson, 1995, Racherla and Adams, 2008) and increased emission of isoprene and increased concentrations of its photochemical byproducts, many of which are known ozone precursors (Roberts et al., 2006) particularly in the Eastern US summer (Guenther, 1997, Lam et al., 2011, Guenther et al., 2012). A warming climate not only changes surface chemistry through changes in temperature, but through changes in atmospheric dynamics (Jacob and Winner, 2009, Hegglin and Shepperd, 2009, Lang and Waugh, 2011, Hu et al., 2012, Barnes and Fiore, 2013, Doherty et al, 2013, Turner et al., 2013, Lin et al., 2014). Under a warming climate, the net effect of both chemical and dynamical changes is to increase the number of NAAQS exceedances in the U.S (Murazaki and Hess, 2006, Jacob and Winner, 2009).

This study examines the physical and chemical factors that can impact ozone chemistry under present-day climate conditions in a particular GCCM. We compare four configurations of the CESM CAM-Chem for a present-day climate (1995 – 2005) in order to highlight and explore both the model's overall ability to simulate the chemical climate of the present day and the impact of various model configurations on the simulated chemical climate. The impact of model resolution on surface chemistry has been largely limited to studies examining the impact of changes in horizontal resolution in GCCMs (e.g. Wild and Prather, 2006, Lin et al., 2008) or limited to CTMs (e.g. Lin et al., 2009, Huang et al. 2013). The main objective of this study is to

answer the question: is the meteorology simulated in this particular GCCM, which is tuned for GCM climate parameters rather than GCCM chemistry parameters, adequate for simulations of future climate and chemistry?

We focus our analysis on metrics of present day ozone that are particularly pertinent to the forecast of future ozone concentration in the CESM CAM-Chem. First, we look at temperature and ozone biases since temperature is an important driver of ozone formation (Jacob and Winner, 2009) and biases may impact our ability to accurately forecast future ozone levels. Secondly, we examine the interannual variability (IAV) of ozone over the 11-year simulation period in order to characterize the model's ability to simulate ozone chemical weather (i.e. interannual variations). We also examine the response of simulated ozone to anthropogenic emission changes as well as the ozone-temperature relationship using a metric called the climate penalty factor or the climate change penalty (Dawson et al., 2007, Wu et al., 2008, Bloomer et al., 2009, Avise et al., 2012, Rasmussen et al., 2012). This metric is defined as the slope of the ozone-temperature relationship ($m_{O3\text{-}T}$). Finally, we examine the model's ability to simulate extreme ozone events as it is usually the highest ozone events that garner the attention of regional and national municipalities.

Section 2 of this paper describes the CESM CAM-Chem and the different model configurations used in this study, as well as the sources and descriptions of emissions, the criteria used to select the CASTNET sites for observational comparison, adjustments made to the surface layer ozone to better match the height of the CASTNET observational stations, and the details of the Mixed Modeling we use for statistical analysis. The results are found in Section 3. Section 3.1 examines the DM8H O_3 and Daily Maximum Temperature (DMT) biases and IAV, Section 3.2 looks at the response to anthropogenic emission changes. Section 3.3 examines the ozone and temperature relationship ($m_{O3\text{-}T}$), while Section 3.4 uses Extreme Value Theory to further explore

the CESM CAM-Chem capabilities. Section 4 contains a discussion of the results and compares climatological variables from each of the four configurations. Section 5 draws conclusions based on the above stated criteria.

III. Methods

A. Description of Simulation

In order to understand the impact of model configurations on the modeled climate-chemistry system, four CESM 1.0 CAM-Chem configurations are compared in this paper. CAM-Chem can be run using specified meteorology (typically called an offline configuration) or with interactive meteorology (L2012), either with specified sea surface temperatures and sea ice or with the atmospheric component fully coupled with the ocean and ice components (both of these are typically called online configurations). The offline configuration reads in winds, surface and air temperatures, surface pressure, heat fluxes and wind stresses from an input meteorological dataset (L2012). Since the same model framework can be run in either an online or offline mode using the same physical parameterizations and the same chemistry the CESM is an ideal choice in comparing online and offline meteorology and chemistry. Online climate runs in the CESM are typically run with a vertical resolution of 26 levels as dictated by the CAM4 physics (L2012) while simulations with specified meteorology are typically run with 56 levels so as to match the resolution of the input meteorological dataset. Vertical interpolation of offline winds can produce severe dynamical noise in the model simulation.

All simulations are from 1994 – 2005, with the first year used for chemical spin-up and not analyzed. CAM-Chem consists of the Community Atmosphere Model (CAM) with fully implemented Model for Ozone and Related chemical Tracers, version 4 (MOZART-4) chemistry with 85 gas phase species, a bulk-aerosol component with 12 species, 39 photolysis reactions and

157 gas phase reactions (E2010, L2012). Long-lived species, such as CH_4, H_2, N_2O and CO_2 are specified at the surface as boundary conditions. The standard resolution is 1.9◦ latitude by 2.5◦ longitude. For a full description of CAM-Chem see L2012. For this paper, we chose the Modern-Era Retrospective Analysis for Research and Applications (MERRA) meteorological dataset (Rienecker et al., 2011) to drive the offline simulation. In all cases, CAM is coupled with the Community Land Model (CLM), the CESM land model. CAM-Chem has been evaluated extensively on a global scale, although with limited evaluation against surface ozone measurements (L2012).

Table 3.1: Summary of configurations for the four CESM simulations. All simulations are run with CESM version 1.0 with identical anthropogenic and biomass burning emissions and the interactive biogenic emissions model MEGAN 2.1.

	vertical levels (total/below 800 hPa)	meteorology	sea surface temperatures	CESM compset
CTM_56 (fully offline)	56/13	MERRA reanalyzed winds*	data ocean	F_SD_CAMCHEM_CN
AMIP_56 (partially offline, 56 levels)	56/13	simulated online	data ocean	F_SD_CAMCHEM_CN
AMIP_26 (partially offline, 26 levels)	26/4	simulated online	data ocean	F_SD_CAMCHEM_CN
CCM_26 (fully online)	26/4	simulated online	POP2 ocean model	B_2000_TROP_MOZART

*: chemistry set to be radiatively passive since meteorology is forced

Table 3.1 summarizes the model configurations analyzed here. Specifically, the simulations include: the CTM_56, a fully offline 56-level simulation with specified MERRA meteorology, ocean sea surface temperatures (SSTs) and sea ice; the AMIP_56, a partially online simulation with 56 vertical levels where meteorology is simulated online but with specified SSTs and ice components that are cycled annually; the AMIP_26, which is identical to the AMIP_56 except that 26 vertical levels are specified; and the CCM_26, a 26-level simulation that includes an interactive ocean (using the POP2 ocean model) and an interactive ice component. These

configurations allow us to examine: (1) the effects of GCM computed meteorology on the chemical system instead of using meteorological fields from a meteorological analysis; (2) the differences between 26-level configurations and 56-level configurations; and (3) the impact of running an interactive ocean model compared to using specified sea surface temperatures. As part of the standard release of the 26-level GCM a number of meteorological parameters have been tuned so as to better reproduce the Earth's climate in the year 2000, but not necessarily its simulation of chemistry. The 56-level configurations have not been explicitly retuned, but instead use the tuning parameters developed for the 26-level configurations. Below 800 hPa, the 26-level configurations have 4 levels while the 56-level configurations have 13 levels (Table 3.1). As a result, boundary layer processes are expected to be more highly resolved when the 56-level resolution is used. The thickness of the bottom layer (approximately 50 meters at the midpoint) is roughly the same in both resolutions (the difference between the 56-level and 26-level vertical gridding always being less than 1% in the summertime).

Except for these explicit differences, we attempted, as much as possible, to keep the differences between various configurations to a minimum. All four configurations are driven with the same anthropogenic and biomass burning emissions (see below) and use the same biogenic emissions model, the Model of Emissions of Gases and Aerosols from Nature, version 2.1 (MEGAN 2.1) (Guenther et al., 2012). Note that MEGAN responds interactively to surface temperature and solar radiation, so the actual biogenic emissions will vary depending on each configuration's surface temperature fields and simulated cloudiness. All four configurations utilize the same standard configurations of radiation parameters and aerosol parameterizations (see E2010 and L2012).

B. Description of Emissions

1. Anthropogenic Emissions

Emissions for the years 1994 - 2005 were obtained from the MACCity emissions, an extension of ACCMIP (Lamarque et al, 2010). Emissions for 2005 over the United States (225◦ - 320◦ E, 24◦ - 60◦ N) were replaced with the EPA NEI 2005 emissions, interpolated from the standard 4x4 km resolution to 1◦ x 1◦ and respeciated to the MOZARTv4 species (available at ftp://aftp.fsl.noaa.gov/divisions/taq/emissions_data_2005). The seasonality found in MACCity was applied to the EPA estimates and linear interpolation between the years 2000 and 2005 was used to estimate US emissions for 2001 – 2004**.**

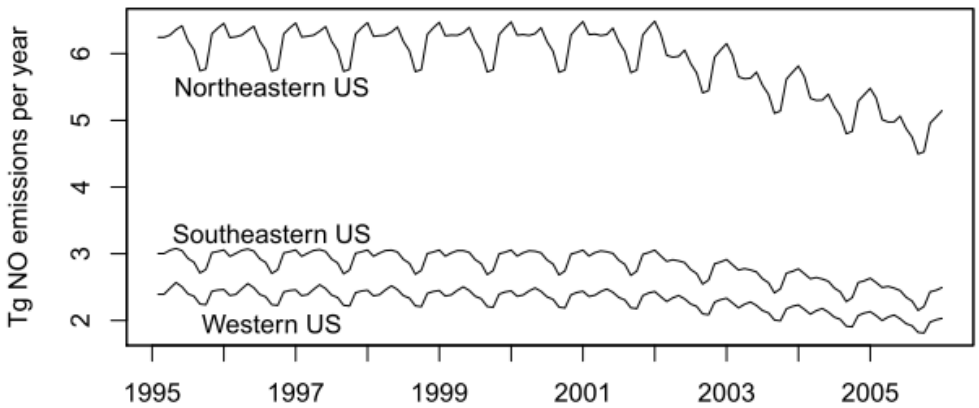

Figure 3.1: Time series for the total monthly NO_x emissions (TgNO / year) for each region (See Figure 3.2) in all configurations.

The NO_x emissions used in this study decrease by roughly 20% between 2001 and 2005 (Figure 3.1) matching the timing of NO_x emissions decreases noted by the US EPA starting after 2002 which lead to reductions in ozone levels beginning in 2003 (US EPA, 2005). However, the reduction in NO_x emissions is less than noted in other studies: Frost et al. (2006) found 50% reductions in NO_x emissions from power plants in the Northeastern US between 1999 and 2003; Kim et al. (2006) find NO_2 columns decreasing by up to 33% over some urban centers in the Northeastern US between 2000 and 2005; Hilboll et al. (2013) show EDGARv4 NO_x emissions

in the Central-Eastern US decrease by more than 10% and NO_x columns decreasing by nearly 20% from 2000 – 2005. After 2005, NO_x emissions contributed to decrease with NO_2 columns from satellite retrievals decreasing, especially around urban centers, by up to 50% from 2005 – 2011 (Russel et al., 2012).

2. Biomass Burning Emissions

Biomass burning emissions were obtained from the RETRO (Schultz et al., 2008) and GFEDv2 (http://daac.ornl.gov/VEGETATION/guides/global_fire_emissions_v2.html) inventories for the years 1994 - 1996 and 1997 - 2005, respectively. Species not included in the RETRO inventory, but included in GFEDv2, were estimated by scaling to the RETRO biomass burning emissions of CO. The scaling coefficient was determined using the GFEDv2 inventory.

3. Natural Emissions

Emissions of isoprene, lumped monoterpenes, methanol, acetone, ethene, propene, ethanol, acetaldehyde, ethane, and propane are calculated online using the updated MEGAN 2.1 (Guenther et al., 2012) and are described in E2010. Heald et al. (2008) estimate global isoprene emissions of 496 Tg C yr^{-1}. The four configurations have average global annual isoprene emissions of 392, 381, 469, and 529 Tg C yr^{-1} for the CTM_56, AMIP_56, AMIP_26, and CCM_26 configurations, respectfully. Global NO_x lightning emissions are estimated to be in the range of 5 ± 3 Tg N/year (Schumann and Huntrieser, 2007) while the model simulations give average annual emissions of 5.69, 5.27, 3.5, and 3.5 Tg N/year for CTM_56, AMIP_56, AMIP_26, and CCM_26, respectfully.

4. CASTNET Site Selection and Filtration Criteria

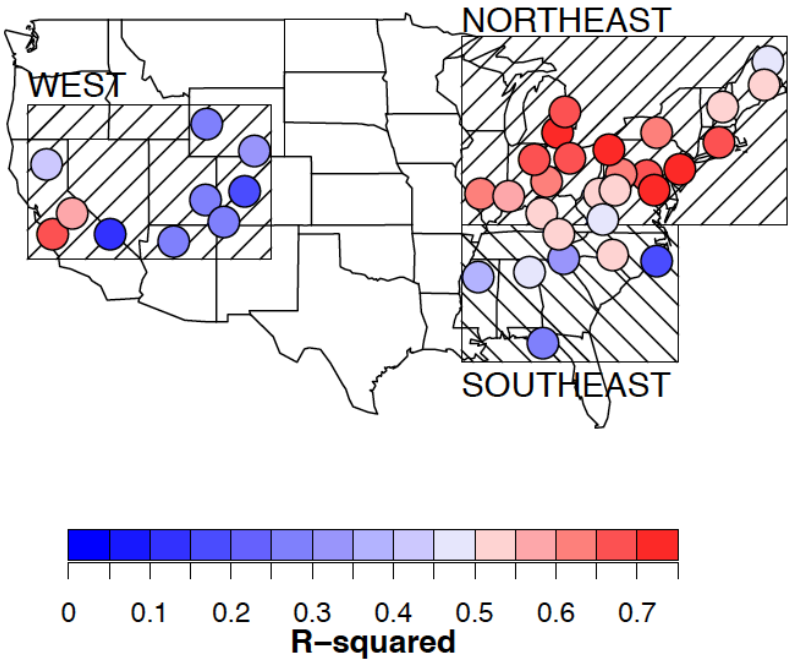

Figure 3.2: Correlation between 1995-2005 DM8H O_3 and DMT at each of the 38 CASTNET sites for the summer months (JJA). There are 1,012 data points in the time series at each site, which leads to any correlation greater than r = 0.06 to be significant at the p < 0.05 level. All sites, therefore, have significant correlations. The boxes indicate the boundaries of the regional definitions that are used in this paper.

We compare model results to the US EPA's Clean Air Status and Trends Network (CASTNET) (CASTNET, 2013a). The rural location of the CASTNET sites minimizes the local impact of urban areas and therefore is an appropriate database for comparison with the relatively coarse resolution of the CESM. For this study, there are 38 sites (Table S4) that have continuous, hourly ozone and temperature data from 1995 - 2005 with at least 80% complete hourly data for the summertime months (June, July, and August) after filtering the raw CASTNET data to remove all data marked as invalid. Only one site from each corresponding model grid cell was chosen. Where there were two sites within one grid cell, the site with the largest level of complete hourly data was chosen. The above criteria result in 10 sites in the western US and 28 sites in the Eastern US. Different ozone-temperature correlations are evident between the

Northeastern and Southeastern US (see Figure 3.2). We can attribute this to the temperature controls on ozone over the Northeastern US and the humidity controls on ozone over the Southeastern US (Camalier et al., 2007, Jacob and Winner, 2009). For this reason the Eastern US is divided (at roughly 36.5◦ N latitude, Figure 3.2) into Northeastern region (21 sites) and a Southeastern region (7 sites).

5. Correction of Simulated Ozone to the Surface

The CASTNET sites measure surface ozone at 10-meter and temperature at 2-meter heights (CASTNET, 2013b), which has necessitated the conversion of grid-layer ozone to 10-meter ozone. Since ozone is a secondary pollutant with no surface emissions, we would expect a lower ozone mixing ratio at 10 meters compared to the approximate 52 meter model bottom grid mid-point as a result of dry deposition and other surface process. Dingenen et al. (2009) utilized an approach based on Tuovinen et al. (2007) and the LRTAP Convention (2004), which uses a resistance analogy to estimate ozone at crop height (roughly 2 - 5 meters) from model output at the mid-point of their bottom grid-box (roughly 30 meters). The method incorporates wind speed, canopy height, surface roughness, and surface fluxes to estimate a neutral stability profile for ozone near the surface. A full description of this approach can be found in the Appendix.

Dingenen et al. (2009) found that 1 meter ozone levels estimated with this method were reduced, on average by 50±20% of 30 meter ozone, but the seasonal mean daytime ozone concentrations were only reduced to 90±10% of the 30 meter ozone. Applying the method to CESM output reduced hourly 10-meter ozone values, on average, by ~ 1 ppb, or roughly 2% on average. These results are consistent with observations of ozone in the bottom meters of the atmosphere (e.g. Kramm et al., 1991). For the remainder of this paper, reported surface ozone values are the calculated 10-meter ozone concentrations.

6. Mixed Modeling

Comparing the 38 sites analyzed in this paper to measurements presents a challenge in that the ozone chemistry at each individual site is likely to have high day-to-day variability and individual characteristics, yet we have some expectation that sites within a particular region will have similar behaviors. For instance Northeastern (see Figure 3.2) stations would be expected to be the most impacted by the promulgation of the 1998 NO_x SIP plan (US EPA, 1998) which primarily impacted NO_x levels over the Northeastern US. In addition the chemical regimes of the Northeastern and Southeastern US are controlled by fundamentally different physical drivers (Camalier et al., 2007, Jacob and Winner, 2009), different from the chemical regime of the Western US.

A site-by-site analysis is useful but cumbersome (see Supplementary Tables S4 and S5) while simple averaging of each site within a region tends to smooth out sub-regional variability (e.g. temperature decreases with increasing latitude). In light of this expectation of both regional patterns and high variability at individual locations, we turn to the Mixed Modeling (MM) statistical approach. This approach allows us to determine if a particular model configuration is significantly different from the CASTNET observations for any particular region and any particular time period as well as identify statistically significant differences between each of the four configurations. MM is a set of theoretical statistical models and tools that separate the input variables (or effects) into two categories: fixed effects and random effects. Fixed effects are variables that are consistent throughout a given dataset under and for which hypothesis testing is performed. Random effects are variables that are included to account for repeated measurements at the site level.

For simplicity, we conduct a MM analysis on each region (i.e. Northeastern, Southeastern, and Western US) and each time period (1995-2000 or pre-SIP and 2001-2005 or post-SIP) independently. In this analysis we classify each dataset (CASTNET, CMT_56, AMIP_56, AMIP_26, CCM_26) as a fixed effect and the data from the individual sites within a time period, region, and dataset as the random effects. This way we can determine if a particular model configuration is significantly different from the CASTNET observations or any of the other configurations for any particular region and any particular time period. By conducting this analysis independently for each region and each time period, we keep the analysis simple and easy to interpret. By treating the sites as the random effect, or as repeated measurements drawn from the same dataset, we are able to determine confidence intervals and conduct significance testing in a straightforward manner without averaging out the variation within each region. This is particularly useful given the high site-to-site variability of all of the variables we analyze in this paper.

IV. Results

In this section, we primarily use the MM approach to determine significant ($p < 0.05$) differences between the CASTNET observations and each of the model configurations, and then differences between the configurations themselves. In particular, the following pairs of simulations are compared in order to isolate: (1) differences in analyzed versus simulated meteorology (CTM_56 versus AMIP_56); (2) differences in vertical resolution (AMIP_56 versus AMIP_26), and (3) differences in specified sea surface temperatures or simulated sea surface temperatures (AMIP_26 versus CCM_26).

A. Mean Ozone and Temperature Biases and Interannual Variability

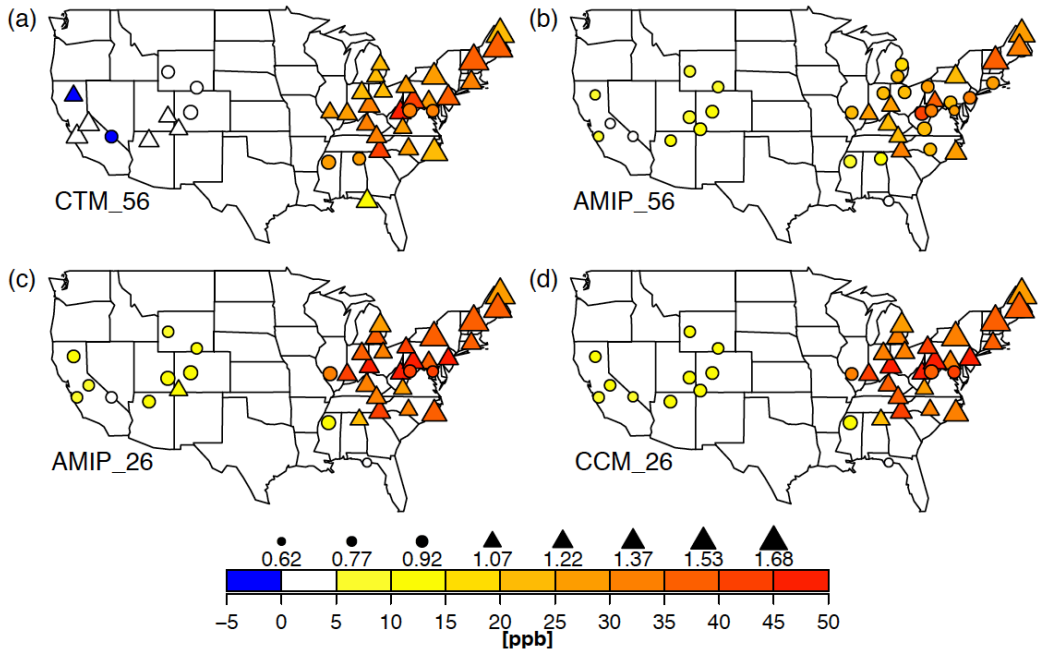

Figure 3.3: Mean biases and interannual standard deviation of summertime DM8H O_3 during the summertime (JJA) for each model configuration sampled at the CASTNET sites: (a) CTM_56, (b) AMIP_56, (c) AMIP_26, and (d) CCM_26, as compared with observations. The color scale indicates the DM8H O_3 bias [ppb] while the size and shape indicate the standard deviation of JJA averaged ozone over the 11-year period divided by the average CASTNET standard deviation at that site (e.g. an upward facing triangle indicates the configuration has a larger standard deviation than CASTNET, while a circle indicates a smaller, or equal, standard deviation). See Table 3.2 for a summary of this Figure.

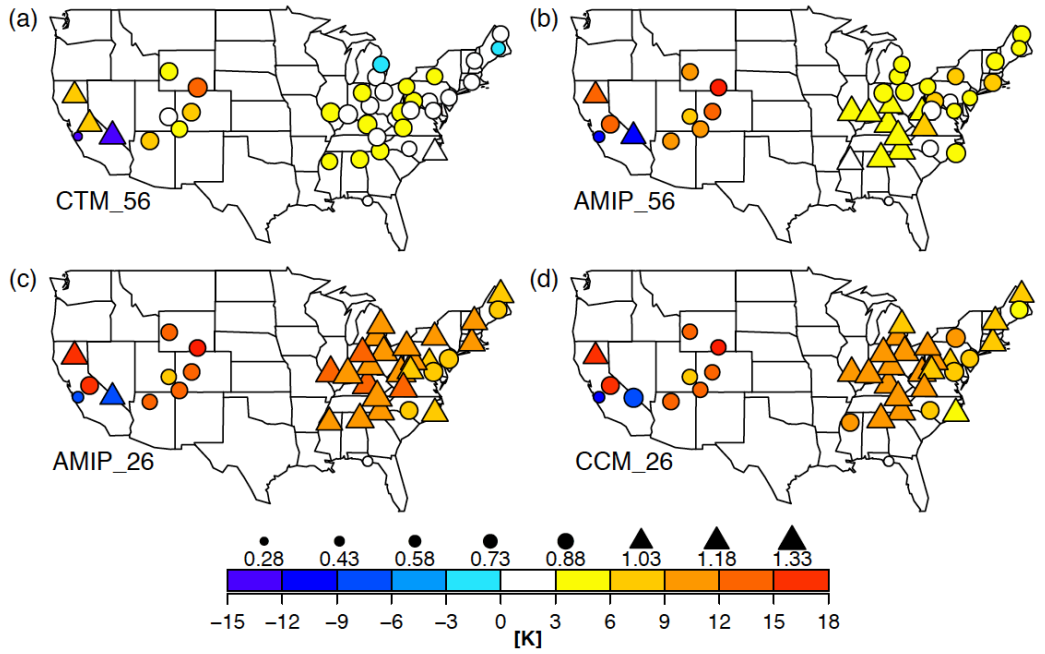

Figure 3.4: Same as Figure 3.3 but for the average DMT Bias [K]. See Table 3.2 for a summary of this Figure.

Table 3.2: Summary of the DM8H O_3 and DMT biases for the four configurations (columns) and three regions (rows) for the summertime months (JJA). Biases and confidence intervals are first calculated at each site and then are averaged among each region using MM modeling. Results for each site can be found in the Supplemental Material (Tables S4-S5). Green values indicate no significant bias calculated using Mixed Model results (see Section III.B.6). Warm values (yellow, orange, red) indicate a significant high bias in order of increasing bias while cool values (blue) indicate a significant low bias. Differences in colors between each configuration indicate that significant differences exist between the configurations. Conversely, if two configurations have the same color for a particular region and variable than there are no significant differences between the two configurations.

	DM8H O_3 Bias [ppb]			
	CTM_56	AMIP_56	AMIP_26	CCM_26
Northeastern US	27.8 [25.4 , 30.3]	25.1 [22.6 , 27.6]	34.7 [32.2 , 37.2]	35.6 [33.2 , 38.1]
Southeastern US	25.7 [17.5 , 33.9]	17.0 [8.78 , 25.2]	24.1 [15.8 , 32.3]	24.4 [16.1 , 32.6]
Western US	1.48 [0.09 , 2.88]	7.96 [6.57 , 9.36]	10.6 [9.23 , 12.0]	9.78 [8.39 , 11.2]

	DMT Bias [K]			
	CTM_56	AMIP_56	AMIP_26	CCM_26
Northeastern US	0.99 [0.46 , 1.52]	3.27 [2.74 , 3.80]	7.02 [6.49 , 7.55]	7.88 [7.35 , 8.41]
Southeastern US	1.75 [0.25 , 3.25]	1.64 [0.14 , 3.14]	5.62 [4.12 , 7.11]	6.03 [4.53 , 7.53]
Western US	0.97 [-4.17 , 6.11]	5.39 [0.25 , 10.5]	6.93 [1.79 , 12.1]	7.37 [2.23 , 12.5]

	overpredicts compared to CASTNET
	no difference from CASTNET
	underpredicts compared to CASTNET

Consistent with other studies (e.g. Murazaki and Hess, 2006, Fiore et al., 2009, Reidmiller et al., 2009, L2012) all four configurations have significant DM8H O_3 and DMT biases in the Northeastern US (Table 3.2, Figure 3.3 and 3.4). Note that DMT is biased in the CTM_56 configuration even though the surface temperature is taken from large-scale analyzed meteorological data. In the Southeastern US all sites in all four configurations have a significant DM8H O_3 bias but only the 26-level models have significant DMT biases. In the Western US the only model without significant bias in either DM8H O_3 or DMT is the CTM_56 configuration.

When comparing the DMT biases from each configuration to each other we find that, in general, the 26-level configurations perform worse than the 56-level configurations and that the CTM_56 generally outperforms all other configurations. In the Northeastern and Southeastern US both the 56-level configurations capture DMT significantly better than the 26-level configurations. In contrast, the DM8H O_3 bias in the CTM_56 is only significantly better than the AMIP_56 in the Western US, but performs equally well in the Southeastern and Northeastern US. The 26-level configurations have the highest DMT biases (from 6 – 8 K) and the highest DM8H O_3 biases (except for the Western US). Rasmussen et al. (2012) found comparable monthly averaged temperature biases (of around 5 K) in online simulations of the Northeastern US. They attributed 5–15 ppb of the DM8H O_3 bias to this temperature bias.

Figures 3.3 and 3.4 also show the interannual variability (IAV) of the four configurations relative to the CASTNET observations. In the Northeastern US, all configurations show more DM8H O_3 IAV than CASTNET except for the AMIP_56 configuration (Figure 3.3b). For the Northeastern US the two 56-level configurations underestimate the DMT IAV (Figure 3.4a,b) while the two 26-level configurations overestimate the DMT IAV (Figure 3.4c,d). Both DM8H O_3 and DMT IAV is realistically simulated in the Southeastern US while in the Western US all configurations show less DM8H O_3 and DMT IAV than CASTNET except for the CTM_56 configuration's DM8H O_3 IAV (Figure 3.3a).

B. Ozone Response to Changes in Anthropogenic Emissions

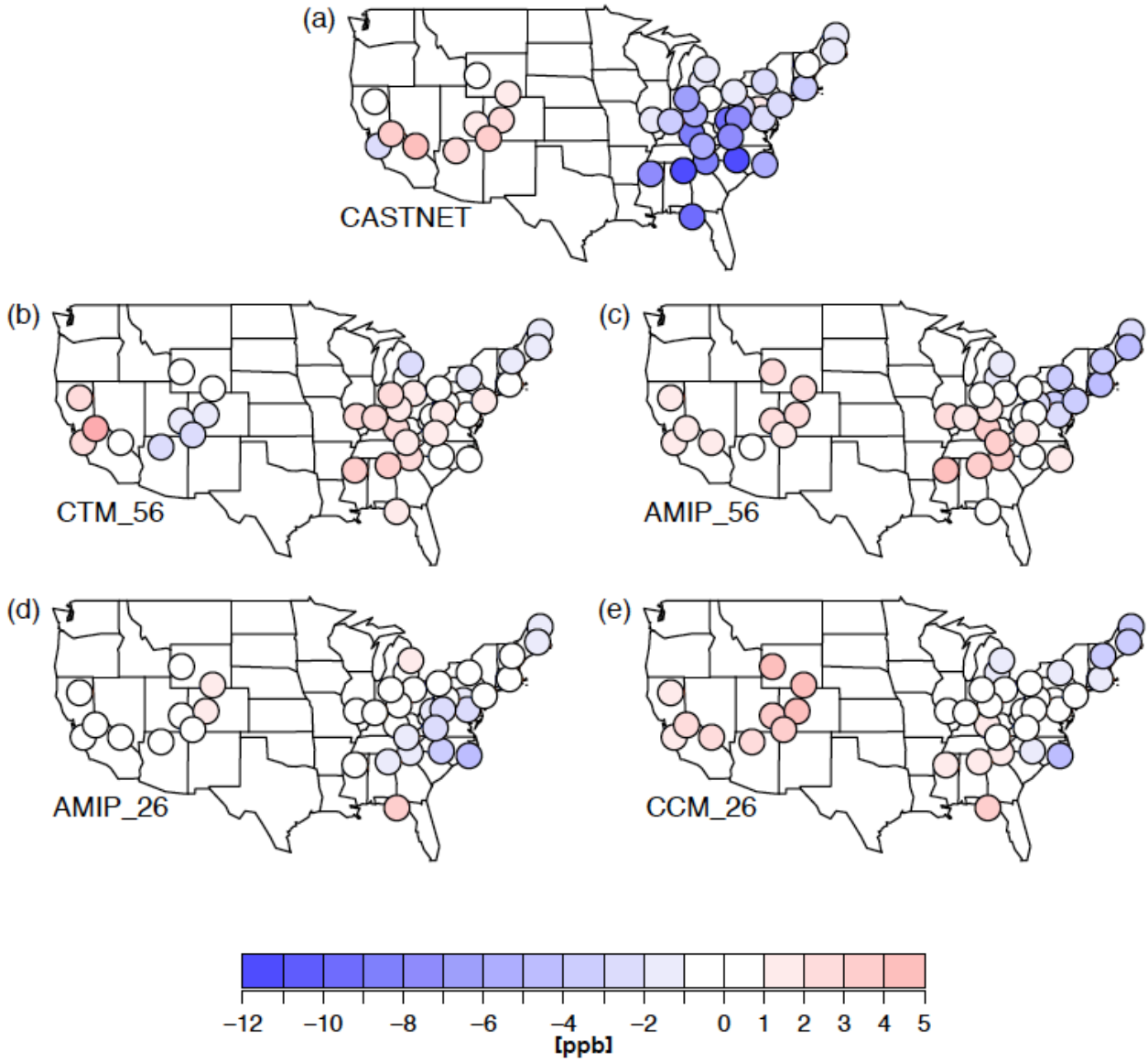

Figure 3.5: The difference [ppb] between the mean DM8H O_3 values from the post-SIP period (2001-2005) and the pre-SIP period (1995 – 2000) for each site at (a) each of the CASTNET sites and the corresponding grid cells for (b) CTM_56, (c) AMIP_56, (d) AMIP_26, and (e) CCM_26 configurations.

Table 3.3: Summary of the difference (ppb) in mean summertime (JJA) DM8H O_3 from the pre-SIP (1995-2000) to the post-SIP (2001-2005) period for CASTNET and the four simulations including 95% confidence intervals in brackets, calculated using linear Mixed Model results (see Section III.B.6). Colors match those in Table 3.2. The differences are first calculated at each site and then are averaged among each region. Asterisks indicate a difference that is statistically different from zero.

	Total DM8H O_3 Difference from pre-SIP to post-SIP [ppb]				
	CASTNET	CTM_56	AMIP_56	AMIP_26	CCM_26
Northeastern US	-5.10* [-6.18 , -4.03]	1.54* [0.46 , 2.62]	-0.82 [-1.90 , 0.26]	1.37 [0.29 , 2.44]	2.17* [1.10 , 3.25]
Southeastern US	-6.96* [-8.57 , -5.35]	4.48* [2.87 , 6.09]	1.37 [-0.24 , 2.98]	2.28* [0.67 , 3.89]	0.46 [-1.15 , 2.07]
Western US	1.75* [0.51 , 2.98]	-1.06 [-2.29 , 0.18]	2.40* [1.17 , 3.64]	4.32* [3.08 , 5.55]	1.35 [0.12 , 2.58]

Table 3.3 summarizes the DM8H O_3 SIP difference (defined here as the difference between the mean summertime DM8H O_3 average from the post-SIP period to the pre-SIP period) for CASTNET observations and the four configurations. Figure 3.5 plots the DM8H O_3 SIP difference for each site for the CASTNET observations and for the four configurations. The CASTNET observations show a significant decrease in DM8H O_3 over the Northeastern and Southeastern US during the between the post-SIP and pre-SIP periods and a significant increase in DM8H O_3 over the Western US. The decreased DM8H O_3 in the Northeastern US has been ascribed to changes in NO_x emissions (Frost et al., 2006, Kim et al., 2006). It is more difficult to ascribe the changes over the Western US to changes in US emissions but decadal ozone changes can be simply caused by climate variability and associated shifts in atmospheric circulation patterns (Lin et al, 2014).

The EPA finds that NO_x emissions decreased significantly after 2002 and reductions in ozone levels began in 2003 (US EPA, 2005). The NO_x emissions in these simulations began to decrease in 2001 (see Supplemental Material and Figure 3.1) due to the linear interpolation between the years 2000 and 2005 using in our input emission datasets. The fact that all four configurations fail to accurately simulate the observed decrease in DM8H O_3 in the Eastern US is somewhat surprising. One possible explanation is that our NO_x emissions show reductions of roughly 20%

over the simulated time period while other studies find a larger decrease of up to 50% (see Section 2.2.1). It is also possible that our simulated NO_x decrease is not sufficient to overcome the simulated DM8H O_3 variability or that the CESM CAM-Chem does not properly simulate the ozone sensitivity to NO_x emissions, perhaps due to the simulated NO_x-VOC emissions ratio (e.g. Duncan et al., 2010).

C. Climate Penalty Factor

The ozone-temperature relationship (alternatively the climate penalty factor, climate change penalty, or $m_{O3\text{-}T}$), typically defined as the slope of the ozone-temperature relationship with units of ppb O_3 K^{-1}, has been utilized in many recent studies (Dawson et al., 2007, Wu et al., 2008, Bloomer et al., 2009, Bloomer et al., 2010, Steiner et al., 2010, Avise et al., 2012, Rasmussen et al., 2012) to characterize the complex ozone climate-chemistry system and to diagnose chemistry model capabilities. The $m_{O3\text{-}T}$ is a useful metric for examining the overall nature of ozone-temperature interactions but is unable to explain any of the individual causal linkages that cumulate to create the total $m_{O3\text{-}T}$ (Weaver et al., 2009, Rasmussen et al., 2012). Thus while $m_{O3\text{-}T}$ is at best an uncertain predictor in a future climate (Weaver et al., 2009) it is still a useful diagnostic tool when examining the overall ozone-temperature relationship.

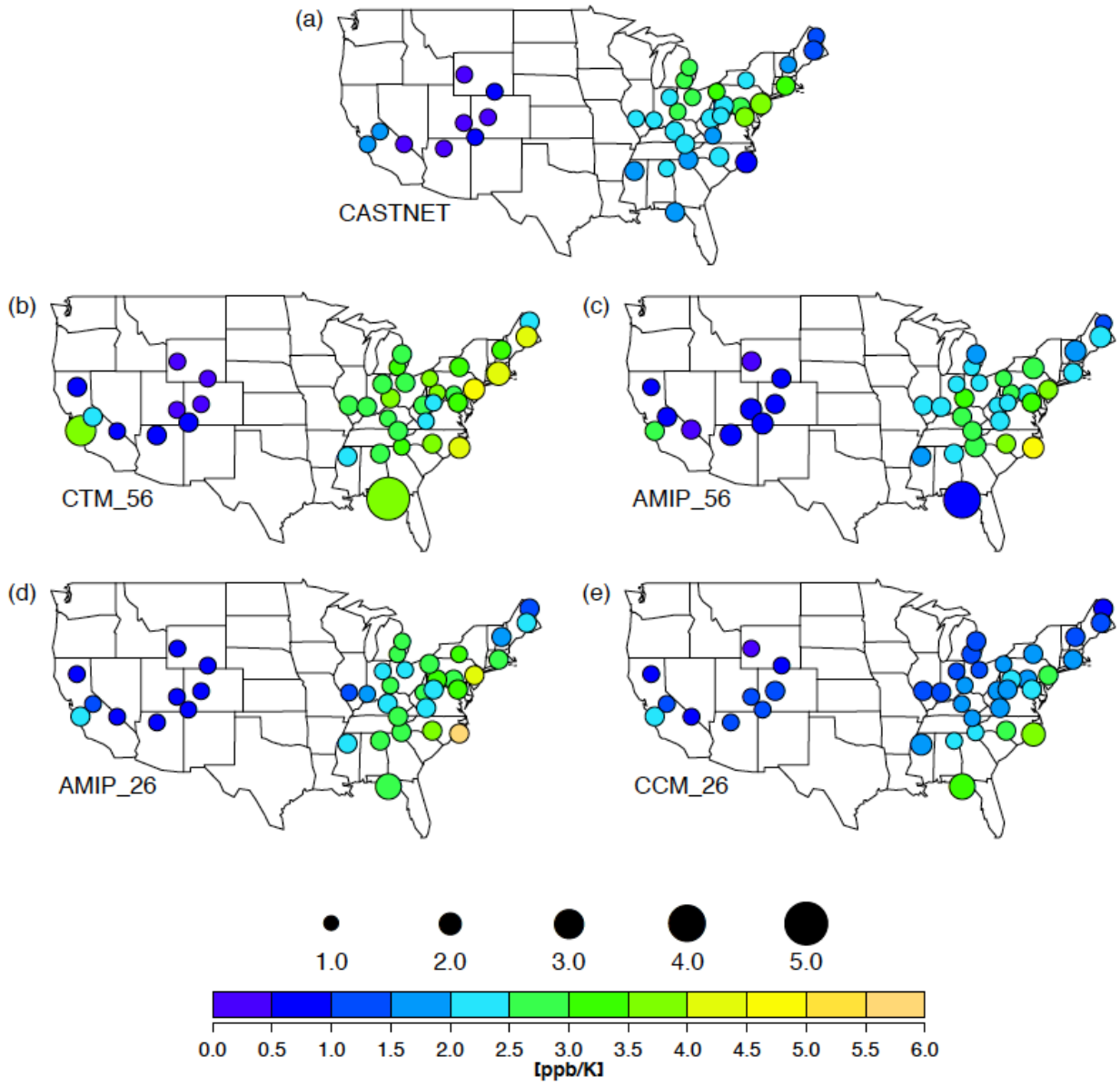

Figure 3.6: Average daily (DM8H O_3 and DMT) summertime (JJA) $m_{O3\text{-}T}$ at (a) each of the CASTNET sites and the corresponding grid cells for (b) CTM_56, (c) AMIP_56, (d) AMIP_26, and (e) CCM_26 configurations. The color scale indicates the $m_{O3\text{-}T}$ [ppb K^{-1}] and the size of each circle indicates the daily standard deviation of the $m_{O3\text{-}T}$.

Table 3.4: Summary of summertime (JJA) statistics accompanying Figure 3.2 and 3.6. The top row contains the R^2 values between DM8H O3 and DMT (all of which are significant), and the second row gives the post-SIP $m_{O3\text{-}T}$ (in ppb/K) with the 95% confidence intervals in brackets obtained through the Mixed Model results (see Section III.B.6). Only post-SIP $m_{O3\text{-}T}$ is shown since we find no significant difference between pre-SIP and post-SIP $m_{O3\text{-}T}$. Colors match those in Table 3.2.

	DM8H O_3 and DMT R^2				
	CASTNET	CTM_56	AMIP_56	AMIP_26	CCM_26
Northeastern US	0.381	0.366	0.331	0.342	0.159
Southeastern US	0.164	0.232	0.337	0.398	0.249
Western US	0.138	0.110	0.132	0.205	0.192

	post-SIP $m_{O_3\text{-}T}$ [ppb/K]				
	CASTNET	CTM_56	AMIP_56	AMIP_26	CCM_26
Northeastern US	2.28 [1.99 , 2.58]	3.54 [3.24 , 3.83]	2.54 [2.24 , 2.84]	2.59 [2.29 , 2.88]	1.72 [1.42 , 2.02]
Southeastern US	1.67 [0.80 , 2.54]	4.07 [3.19 , 4.94]	2.46 [1.59 , 3.33]	3.54 [2.67 , 4.41]	2.97 [2.09 , 3.84]
Western US	0.73 [0.21 , 1.25]	1.64* [1.11 , 2.16]	1.33* [0.81 , 1.85]	1.16 [0.64 , 1.68]	0.88 [0.36 , 1.41]

Here, we define $m_{O3\text{-}T}$ only for the summer months (JJA), as is done in most other studies, and use daily values (DM8H O_3 and DMT) to calculate $m_{O3\text{-}T}$. The slope of the ozone-temperature relationship is calculated using Ordinary Least Squares (OLS) regression as the uncertainty in measured temperature is significantly less than the uncertainty in ozone. This is the method used in the majority of other studies. Using Reduced Major Access (RMA) regression to define $m_{O3\text{-}T}$ (e.g. Rasmussen et al., 2012) is likely to systematically estimate a larger slope than OLS regression (Smith, 2009). We find daily $m_{O3\text{-}T}$ to be in the range of 0 – 6 ppb K^{-1} (Figure 3.6, Table 3.4), which is within the range of other studies although details of the sampling frequency and geographical averaging tend to differ in each of these studies: Bloomer et al. (2009) used hourly ozone and temperature measurements in the Eastern US and found a summertime $m_{O3\text{-}T}$ range from 2.4 – 3.3 ppb K^{-1}; Steiner et al. (2010) used 1-hour maximum ozone and temperature measurements and found $m_{O3\text{-}T}$ of 2 – 8 ppb K^{-1}; Avise et al. (2012) modeled daily maximum ozone and temperature and found summertime values throughout the US in the range of 0.12 – 2.65 ppb K^{-1}; Rasmussen et al. (2012) analyzed monthly averaged DM8H O_3 and DMT CASTNET measurements using RMA and found $m_{O3\text{-}T}$ ranging from 3 – 6 ppb K^{-1} in the summertime Northeastern US.

Interestingly, AMIP_56 matches the CASTNET $m_{O3\text{-}T}$ in the pre-SIP period (not shown) and in the Northeastern and Southeastern US post-SIP period (Table 3.4) while CTM_56 over predicts the observed $m_{O3\text{-}T}$ in all regions. In the Southeastern US, the CTM_56 post-SIP $m_{O3\text{-}T}$ is roughly double the CASTNET $m_{O3\text{-}T}$ (Table 3.4). CASTNET observations show the mean $m_{O3\text{-}T}$ is smaller in the Southeastern US than in the Northeastern US (Table 3.4). The two 56-level configurations show little difference between these two regions and the 26-level configurations show higher values in the Southeastern US than in the Northeastern US, the opposite of observed $m_{O3\text{-}T}$ (Figure 3.6, Table 3.4). A noticeable discrepancy with measurements is also observed over the far Northeastern US in the CTM_56 configuration.

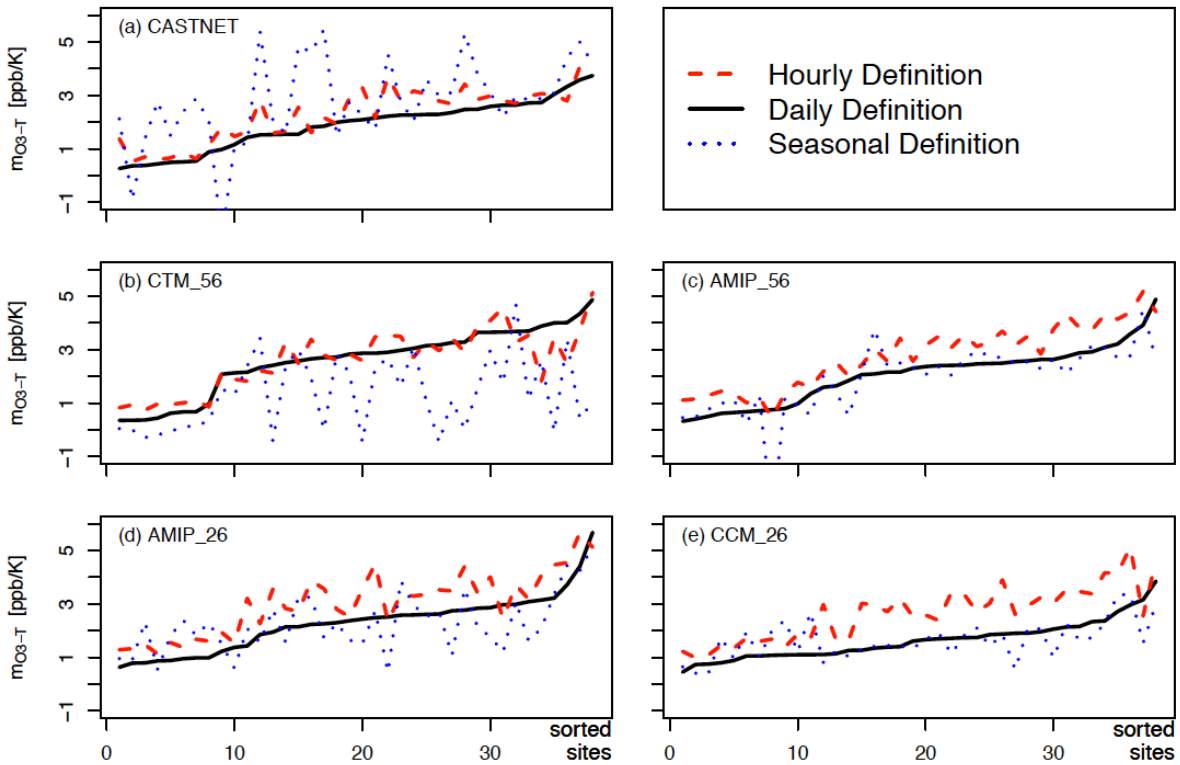

Figure 3.7: Different time-scales of definition for $m_{O3\text{-}T}$ for: (a) CASTNET, (b) CTM_56, (c) AMIP_56, (d) AMIP_26, and (e) CCM_26. For each plot, the sites are sorted from lowest to highest daily $m_{O3\text{-}T}$ (the solid black line) for the summer months (JJA). The red dashed line is the hourly $m_{O3\text{-}T}$ and the blue dotted line is the seasonal (JJA) $m_{O3\text{-}T}$. Note that among the plots, the sorted sites are not the same (i.e. site 1 for CASTNET does not correspond to site 1 for CTM_56). Also note that CASTNET (a) and AMIP_56 (b) each have one anomalous site, BFT142 and SUM156, respectfully, that drops below the bottom axis with values of -2.36 ppb/K and -3.49 ppb/K, respectfully. These sites are not shown for reasons of clarity.

Figure 3.7 demonstrates rather subtle differences do occur at individual sites when sampling on hourly, daily, or seasonally averaged timescales. On hourly timescales $m_{O3\text{-}T}$ will capture the short term relationship between ozone and temperature (such as the diurnal cycle) while on daily or seasonal timescales $m_{O3\text{-}T}$ should better capture the synoptic changes in ozone and temperature. For CASTNET (Figure 3.7a) little difference is apparent between an hourly definition of $m_{O3\text{-}T}$ and a daily definition of $m_{O3\text{-}T}$ (black and red lines, respectfully), with differences typically less than 2 ppb K^{-1}. In contrast, some sites show a large difference between the seasonally averaged definition of $m_{O3\text{-}T}$ (blue line) and the other two definitions. Site-by-site analysis shows maximum differences between 3 and 4 ppb K^{-1} with the outlier sites for the seasonal definition of $m_{O3\text{-}T}$ located in the western US (data not shown). Moreover, the sites where ozone is most sensitive to seasonal changes in temperature do not appear to be the most sensitive sites to hourly or daily values. This indicates that, at least at many sites, the ozone-temperature relationship is controlled by different factors at different time scales in the data.

None of the model configurations reproduce the measured relationship on the seasonal timescale between ozone and temperature (Figure 3.7b-e). In all simulations the qualitative behavior of the hourly and daily slopes appear similar to the CASTNET measurements with hourly and daily slopes following the same curve and with similar magnitudes to those measured. However, the seasonal slopes are different from the CASTNET slope. In the case of online simulations, the seasonal slopes are comparable to the daily and hourly slopes and the sensitivity of the individual sites is approximately the same. In contrast, the CTM_56 shows much lower seasonal sensitivities by almost 5 ppb K^{-1} at many sites (Figure 3.7b). These anomalous sites for the CTM_56 configuration are exclusively in the Northeastern US (data not

shown), implying that the offline meteorology is likely driving the model-measurement discrepancy in seasonal $m_{O3\text{-}T}$ in the Northeastern US.

D. Extreme Value Theory Analysis

Several recent studies (Frossard et al., 2013, Rieder et al., 2013a, 2013b) have utilized extreme value theory (EVT) to characterize DM8H O_3 distributions since they are generally positively skewed (i.e. have long right-hand tails) and since state and federal agencies are particularly concerned with characterizing and controlling high ozone exceedances. Due to this positively skewed distribution the Generalized Pareto Distribution (GPD) (see Pickands, 1975) can match DM8H O_3 distributions better than the normal Gaussian distribution (Rieder et al., 2013a). We chose the threshold parameter of the GPD distribution to match the NAAQS for ozone at 75 ppb (see Rieder, 2013a). The size and shape parameter are fit with the maximum likelihood method and the return interval (below) are calculated using the R (www.r-project.org) Points-Over-Threshold (POT) Package (Ribatet, 2012).

For more details on EVT, POT, and the methods by which we calculate the return interval see Reider et al. (2013a) and Ribatet (2012). Note that for the following analysis, for each of the configurations, the mean DM8H O_3 biases are removed. This corrects for the magnitude of the mean biases (and allows for concordant comparisons of a set threshold), and thus only differences in the shape of the distributions are accounted for here. This is a simple preliminary EVT analysis and a more advanced analysis is beyond the scope of this current study.

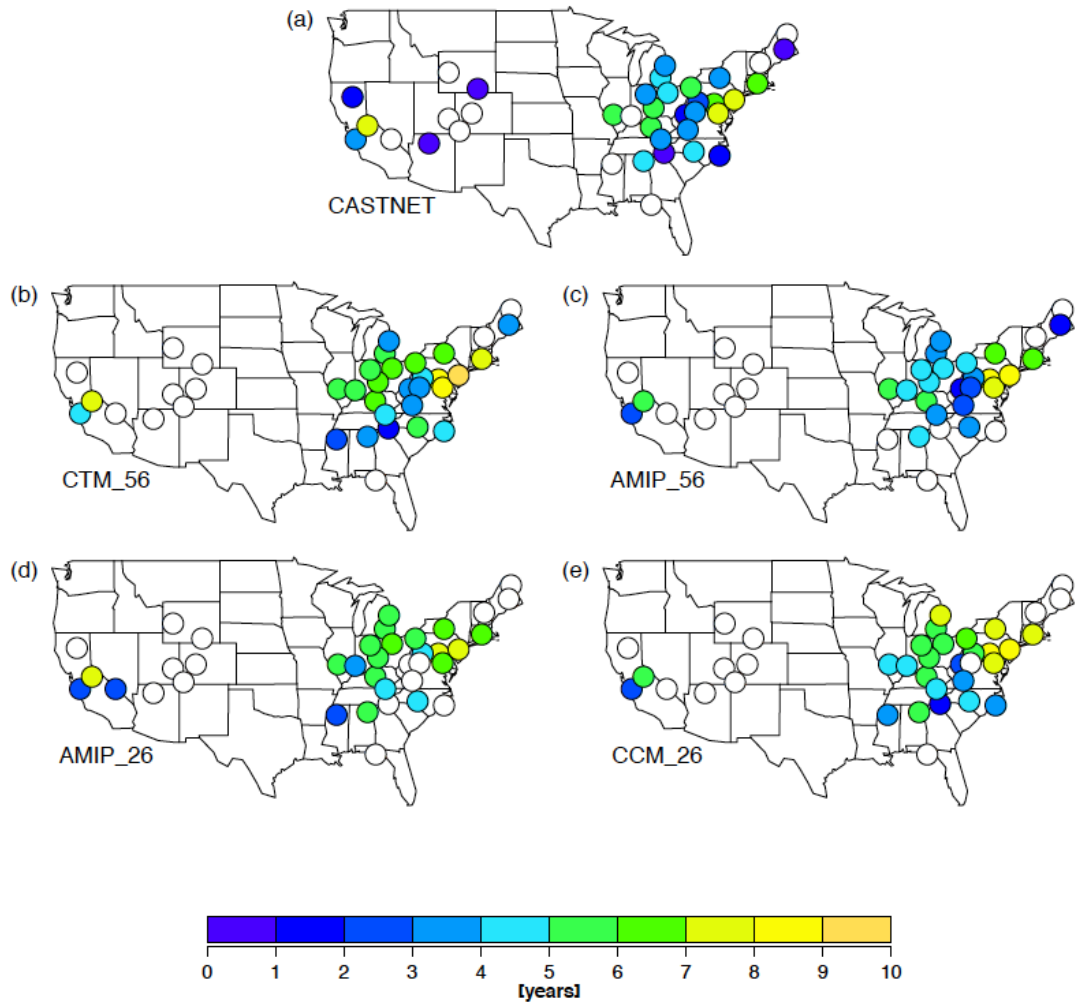

Figure 3.8: The estimated return interval for a 100 ppb daily ozone event (in years) for JJA for (a) the CASTNET sites and the corresponding grid cells for (b) CTM_56, (c) AMIP_56, (d) AMIP_26, and (e) CCM_26 configurations. A white circle indicates that there was not enough data to determine a return interval for a threshold parameter of 75 ppb

Table 3.5: Statistical Summary of Return Interval (accompanying Figure 3.8) and Skewness for the mean values and standard deviations of all sites within each region. Colors match those in Table 3.2. Return Interval significance testing is omitted for Western US since only 2 sites within the region had DM8H O_3 values high enough to draw conclusive results regarding the 100 ppb Return Interval.

	Return Interval [days]				
	CASTNET	CTM_56	AMIP_56	AMIP_26	CCM_26
Northeastern US	4.50 [3.72 , 5.46]	5.83 [4.96 , 6.71]	4.74 [3.87 , 5.62]	5.78 [4.90 , 6.66]	5.42 [4.53 , 6.31]
Southeastern US	2.86 [1.36 , 4.35]	3.65 [2.16 , 5.14]	2.50 [0.95 , 4.05]	3.89 [2.41 , 5.38]	3.82 [2.31 , 5.34]
Western US	2.99 [0.23 , 5.74]	3.37 [0.62 , 6.13]	1.06 [-1.70 , 3.81]	1.24 [-1.52 , 4.00]	2.15 [-0.60 , 4.91]

	Skewness [unitless]				
	CASTNET	CTM_56	AMIP_56	AMIP_26	CCM_26
Northeastern US	0.44 [0.35 , 0.52]	0.26 [0.18 , 0.35]	0.25 [0.16 , 0.34]	0.11 [0.02 , 0.20]	0.08 [-0.01 , 0.17]
Southeastern US	0.21 [-0.28 , 0.70]	0.14 [-0.36 , 0.63]	0.46 [-0.04 , 0.95]	0.34 [-0.15 , 0.83]	0.42 [-0.08 , 0.91]
Western US	0.14 [-0.06 , 0.34]	0.18 [-0.02 , 0.38]	-0.06 [-0.26 , 0.14]	-0.22 [-0.42 , -0.02]	-0.08 [-0.28 , 0.12]

Figure 3.8 plots the mean Return Interval and Table 3.5 summarizes the Return Interval and Skewness MM statistical analysis. CASTNET and all four configurations show high heterogeneity for the calculated return interval. The return interval for a 100 ppb DM8H O_3 event generally ranges from roughly every 3 years in the far Western US and in the Southeastern US to nearly every 5 years in the Northeastern US. The interior Western US generally has lower ozone levels, and therefore fewer events where ozone exceeds 75 ppb. In all simulations there are only a few (1 to 3) events in the interior Western US where bias corrected ozone exceeds 100 ppb. For this reason, we focus on the Eastern US return intervals for the rest of this analysis. The return intervals are generally well simulated for all configurations in the Southeastern US. In the Northeastern US only the AMIP_56 configuration accurately reproduces the return interval; the other configurations over estimate the return interval and thus underestimate the frequency of high ozone events. This may be related to the underestimation of the skewness parameter (Table 3.5), although the relationship is not simple. Skewness is related to the overall shape of the distribution while the extreme values relate to the tails of the distribution. The CASTNET observations for the Northeastern and Southeastern US have positive skewness (i.e. a long high ozone tail). All of the configurations underestimate this positive skewness in the Northeastern US. This translates to an overestimation of the 100 ppb return interval for all configurations except for the AMIP_56. The AMIP_56 configuration underestimates the skewness parameter while accurately simulating the return intervals in the Northeastern US. Significant differences are noted between the 56-level configurations and the 26-level configurations, with the 56-level configurations underestimating the observed skewness by roughly 50% and the 26-level

configurations predicting less than 25% of the observed skewness (Table 3.5). All configurations capture the Southeastern US skewness.

V. Discussion

In order to clarify both the differences and the similarities among the four configurations we now interpret the above results in the context of the following questions: (1) How do differences in forced or simulated meteorology (i.e. CTM_56 versus AMIP_56) impact the summertime ozone chemistry over the US? (2) How do differences in vertical resolution and/or model tuning (i.e. AMIP_56 versus AMIP_26) impact the summertime ozone chemistry? (3) How do differences in forced sea surface temperatures or simulated sea surface temperatures (i.e. AMIP_26 versus CCM_26) impact the simulated chemistry.

Table 3.6: A Summary Table for CASTNET and the simulation configurations for all of the metrics used in this paper for different regions for the summertime (JJA). Green colors (with a 0) indicate no statistical difference between the configuration and CASTNET observations. Warmer colors (with + symbol) indicate that the configuration over predict compared to CASTNET, while cooler colors (with – symbol) indicate the configurations under predict compared to CASTNET. Different colors (and number of symbols) indicate a grouping of the configurations based on statistical differences. For instance, all configurations over predict the DM8H O_3 in the Northeastern US (warm colors); the two 56-level configurations (yellow with +) are not statistically different from one another and the two 26-level configurations (orange with ++) are not statistically different from one another, but each pair is statistically different from the other pair.

	Northeastern US				Southeastern US				Westernern US			
	CTM_56	AMIP_56	AMIP_26	CCM_26	CTM_56	AMIP_56	AMIP_26	CCM_26	CTM_56	AMIP_56	AMIP_26	CCM_26
DM8H O_3 Bias (Figure 3, Table 2)	+	+	++	++	+	+	+	+	0	+	++	++
DMT Bias (Figure 4, Table 2)	+	++	+++	++++	0	0	+	+	0	+	+	+
DM8H O_3 IAV (Figure 3)	+	0	+	+	0	0	0	0	0	-	-	-
DMT IAV (Figure 4)	--	-	+	+	0	0	0	0	-	-	-	-
ΔDM8H O_3 from pre-SIP to post-SIP (Table 3)	++	+	++	++	++	+	+	+	-	0	+	0
Post-SIP $m_{O_3\text{-}T}$ (Table 4)	+	0	0	-	+	0	+	0	+	+	0	0
Return Interval (Figure 8, Table 5)	+	0	+	+	0	0	0	0	0	-	0	0
Skewness (Table 5)	--	--	-	-	0	0	0	0	0	0	-	0

--	-	0	+	++	+++	++++
underpredicts compared to CASTNET		no difference from CASTNET	overpredicts compared to CASTNET			

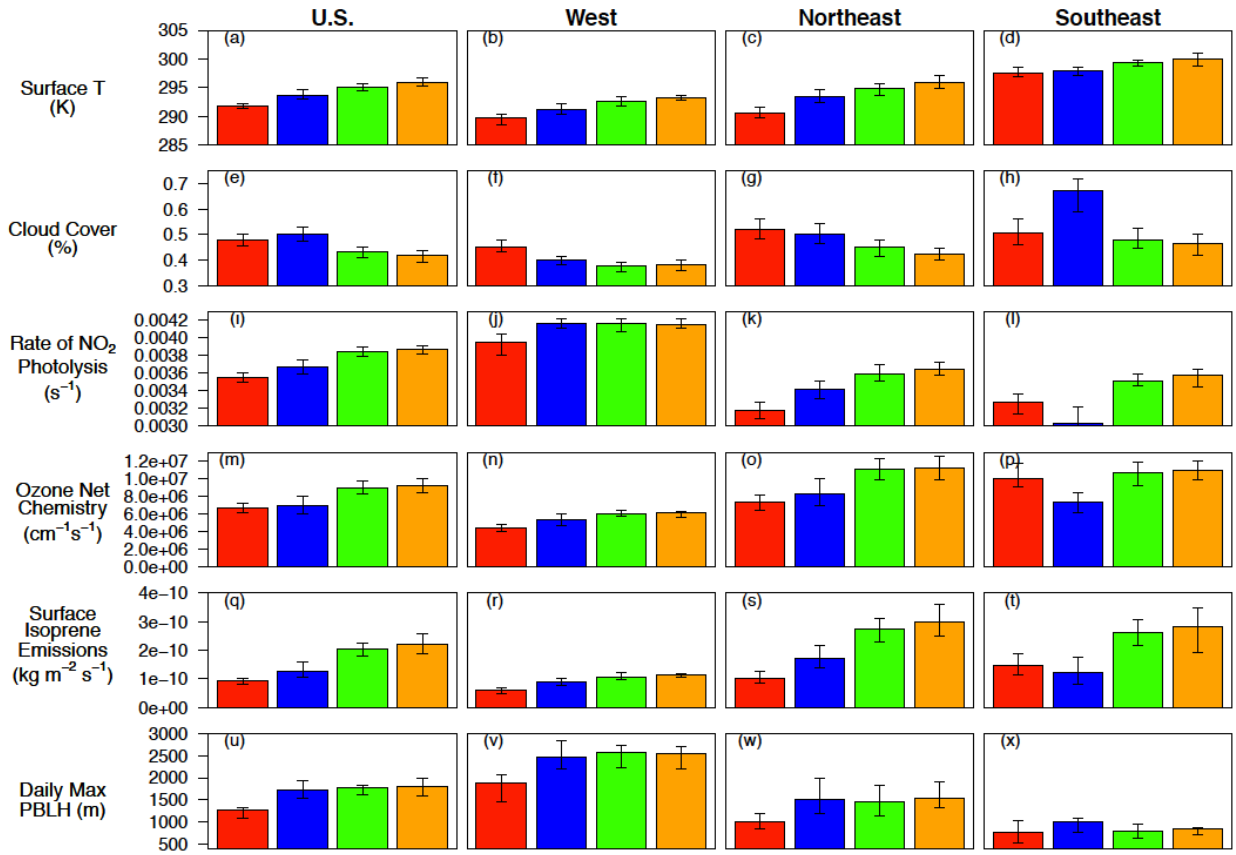

Figure 3.9: Surface layer variables from all four model configurations (CTM_56 (red), AMIP_56 (blue), AMIP_26 (green), and CCM_26 (orange)) for the 1995 – 2005 summertime (JJA). Error bars are the 95% confidence intervals for the average summertime (JJA) values for each region. The variables plotted are chosen for their likely impact on surface ozone chemistry. The rate of NO_2 photolysis we use as a proxy for insolation. The O_3 net chemistry is the net production minus destruction of ozone. The plots are for the contiguous US (left) and three sub regions: the Western US, the Northeastern US, and the Southeastern US (See Figure 3.2).

Table 3.6 summarizes the results from Section 3 while Figure 3.9 shows a comparison of select surface layer climatological variables (temperature, percent cloud cover, the photolysis rate of NO_2, net ozone chemical production, emissions of isoprene and boundary layer height) that are expected to have a large impact on ozone chemistry. The photolysis rate of NO_2 acts as a proxy for the amount of radiation that can penetrate to the surface layer in the model. Note that many of these variables are not well characterized through measurements.

We begin by examining the online configuration (CTM_56) with respect to the offline configuration (AMIP_56). This comparison allows us to examine the extent to which

meteorological biases inherent in online versus offline configurations introduce biases in the chemical fields. All temperature biases are higher in the AMIP_56 configuration than in the CTM_56 configuration. However, in other metrics (Table 3.6) the CTM_56 configuration does not outperform the AMIP_56 configuration. For example over the Northeastern US the CTM_56 outperforms the AMIP_56 in simulation of temperature, but does not do as well in the simulation of IAV (temperature and ozone), $m_{O3\text{-}T}$, and return interval. A similar conclusion can be drawn for a variety of metrics for the Southeastern and Western US (Table 3.6).

Differences in maximum daily planetary boundary layer height (PBLH) are apparent in most regions when comparing CTM_56 and AMIP_56 configurations (Figure 3.9u-x). Except in the Southeastern US the CTM_56 configuration is anomalously low. The boundary layer in the AMIP_56 configuration is comparable to that in the simulations with 26-levels, suggesting that the height of the boundary layer is not simply related to the number of vertical levels. By looking at summertime mean daily maximum PBLH we see that AMIP_56, AMIP_26, and CCM_26 are all within 10% of each other. Satellite retrievals over the US find afternoon PBLH of 1500 - 2000 meters in the summer with higher PBLH in the Southeastern than in the Northeastern (roughly 2000 meters and 1700 meters, respectfully) (McGrath-Spangler and Denning, 2013). All configurations match observations in the Northeast, but underestimate PBLH in the Southeastern by approximately 50%. The offline simulation appears to most dramatically underestimate the PBLH, suggesting that in some aspects offline simulations can create biases not inherent in the online simulations. The offline boundary layer is highly dependent on the input temperature and moisture input fluxes to the offline model. The fact that these fields are only input every 3 hours with linearly interpolation of the variables between these input times may not allow the boundary layer to realistically evolve in the offline model. Further

investigation of this aspect of forced meteorology and simulated meteorology is needed. Hess and Mahowald (2009) recommended that reanalysis meteorological data be used with caution as they found that climate models are sometimes able to outperform reanalysis data in capturing some long-term meteorological trends.

Over the Southeastern US the AMIP_56 configuration has significantly more clouds, reduced NO_2 photolysis and reduced ozone production than the CTM_56 and the 26-level configurations. Somewhat surprisingly, these differences are not apparent when comparing the DM8H O_3 and DMT statistics between the CTM_56 and AMIP_56 configurations (Table 3.6). We suspect the large cloudiness fraction produced by AMIP_56 over the Southeastern US is due to a coupling of the high vertical resolution and the land surface fluxes of temperature and moisture in AMIP_56. In the CTM_56 configurations the surface fluxes are input from meteorological analysis, while in the 26 level versions the surface fluxes are calculated from the GCCM (as in AMIP_56).

Comparisons between AMIP_56 and the AMIP_26 configurations reflect differences in the number of vertical levels as well as in model tuning: the 26-level configurations have been globally tuned while the 56-level configurations have not (L2012). Mauritsen et al. (2012) demonstrate how the unavoidable practice of model tuning can obscure a variety of compensating errors within GCMs. Since the CESM CAM-Chem has been globally tuned only for 26-levels (L2012), the decision to switch to 56 vertical levels without additional tuning is expected to draw out biases or errors that may have previously been left malignant during the previous tuning process. We do not know if tuning of the 56-level configurations will reduce these biases and errors.

The AMIP_56 configuration generally outperforms the AMIP_26 configuration, particularly over the Northeastern US. The AMIP_26 configuration has less cloud cover than AMIP_56

configuration in all regions (Figure 3.9), higher temperatures, higher NO_2 photolysis and higher isoprene emissions. Taken together these could lead to higher ozone production**.** The combination of these factors is consistent with the larger ozone biases in AMIP_26 configuration than in the AMIP_56 configuration (Table 3.2 and Table 3.6). In addition, the high DMT biases in the 26-level configurations may distort the ozone-temperature relationship. For example, high DMT biases in the 26-level configurations may occasionally be simulating temperatures outside of the 295 – 312 K temperature range where a linear increase in ozone production with temperature is noted (Steiner et al, 2009), which could alter the simulated $m_{O3\text{-}T}$. The analysis above suggests that at least over the US simple changes in model formulation (i.e. the number of vertical levels) may have significant impacts on simulated ozone chemistry.

The comparison between the two 26-level model configurations, one driven by interactive ocean (CCM_26) and the other by specified SST (AMIP_26), suggests little difference in the two simulations. The AMIP_26 may outperform the CCM_26 in the Northeastern US, but the CCM_26 shows a slight edge over the Southeastern US. In all aspects the surface layer climatology of these two simulations is similar. Thus, our simulations suggest, that the use of an ocean model does not significantly degrade simulations of ozone chemistry during the summer months over the US.

VI. Conclusion

We have conducted a diagnostic analysis of ozone chemistry simulated by the CESM CAM-Chem with MOZART-4 chemistry, a Global Climate-Chemistry Model, during the summer months over the US from 1995 – 2005. The purpose of this study was to determine whether the CESM CAM-Chem is appropriate for simulations of future climate and chemistry. In particular, we wanted to determine the extent to which meteorological biases in the CESM act to distort its

ability to simulate surface ozone. We compared the following four configurations: (1) CTM_56, with forced meteorology, specified sea ice and ocean temperatures, and 56 vertical levels; (2) AMIP_56, with simulated meteorology, specified sea ice and ocean temperatures, and 56 vertical levels; (3) AMIP_26, with simulated meteorology, specified sea ice and ocean temperatures, and 26 vertical levels; and (4) CCM_26, with simulated meteorology, simulated sea ice and ocean temperatures, and 26 vertical levels.

We examined a number of metrics to distinguish the model simulations and compare them to CASTNET observations: (1) ozone and temperature biases, (2) ozone and temperature interannual variability; (3) ozone changes from 1995 – 2005; (4) the slope of the ozone-temperature relationship ($m_{O3\text{-}T}$); and (5) return interval of a 100 ppb DM8H O_3 event.

We have used Mixed Modeling (MM) to evaluate the model results. This is a procedure for statistically combining station records regionally to more clearly isolate model-measurement differences. We believe this technique can be valuably pursued in future comparisons between models and observations to provide a more nuanced statistical analysis. As with most statistical methods, larger datasets will invariably increase the statistical power of these results.

Most model-measurement comparisons have simply compared ozone in the first model layer with surface ozone measurements. We evaluated the validity of this practice by extrapolating simulated ozone to 10 meters using wind speed, canopy height, surface roughness, and surface fluxes and assuming a neutral stability profile for ozone near the surface (see Appendix and Supplemental Material). In the simulations analyzed here this has little impact on the model-measurement ozone comparisons, although we do not always expect this to be the case. Further analysis of surface layer dynamics and their parameterizations in GCCMs is recommended.

Our analysis has clarified some of the reasons for the significant differences in $m_{O3\text{-}T}$ reported in the literature. First, use of the Reduced Major Axis (RMA) to diagnose the temperature-ozone slope produces a significantly larger slope. We have used Ordinary Least Squares (OLS) in our analysis. Second, care must be taken when defining the time-scale of ozone-temperature metrics as ozone-temperature interactions span a range of time scales, with potentially different slopes. Finally, care must be taken when combining measurements from individual sites within a region so as to avoid confounding the geographical and temporal relationship between ozone and temperature (see also the analysis of Rasmussen et al., 2012).

All simulations capture some aspects of the measured metrics correctly (Table 3.6), especially in the Western and Southeastern US. However there were also some notable biases in all simulations. First, consistent with other studies, we have found high DM8H O_3 biases of 15 – 35 ppb over the Eastern US under all configurations. We also found significant DMT biases of 1 – 8 K in the Eastern US under all configurations. Even the simulation using analyzed meteorology (CTM_56) has a positive DMT bias. The DMT biases, however, are not sufficient to explain the very large bias in simulated DM8H O_3 over the Northeastern US. Val Martin et al. (2014) shows that modifications in the parameterization for the dry deposition of ozone can alleviate some, but not all, of the surface bias in simulated ozone.

None of the simulations capture the clear decrease in ozone between 1995-2000 and 2001-2005 over the Northeastern US captured in the CASTNET measurements. The measured ozone reduction has been attributed to reductions in NO_x emissions due to the EPA 1998 NO_x SIP call. While this may indicate a potential problem in the simulated response to NO_x emission decreases (i.e. ozone formation sensitivity changes noted in Duncan et al. (2010)), it is more likely that the

lack of expected ozone response is due to the 20% decrease in NO_x emissions used in these simulations instead of the nearly 50% decrease as seen in the observations.

We find daily $m_{O3\text{-}T}$ (DM8H O_3 and DMT) to be in the range of 0 – 6 ppb K^{-1} (Figure 3.6, Table 3.4), which is within the range of other studies. CASTNET observations show a lower mO3-T in the Southeastern US than in the Northeastern US that is not captured by any of the configurations. In addition, none of the configurations produced the correct $m_{O3\text{-}T}$ when using a seasonal definition. This suggests that while simulations of short-term chemistry (i.e. days to months) may have the correct response to temperature changes, simulations of long-term chemistry (i.e. years to decades) should be treated cautiously.

This was one of the first applications of extreme value analysis to simulated results. Our simulations capture the observed return intervals in the Southeastern and Western US. The CASTNET observations suggest the return interval for a 100 ppb DM8H O_3 event is highest over the Northeastern US. Our configurations do simulate a higher return interval in the Northeastern US, but with the exception of the AMIP_56 configuration, which matches the CATNET observations, the return interval is overestimated. In addition, the DM8H O_3 distribution skewness is well simulated in all regions except the Northeastern US, where all configurations underestimate the observed skewness. Additional EVT analysis, especially in the Northeastern US, is recommended.

Our analysis has one primary question at its core: Is the meteorology simulated in GCMs adequate for simulations of future chemistry and climate in GCCMs? Overall the answer is yes although care must be taken, as the simulated chemistry is sensitive to a variety of model parameters. As discussed above, if general climate-chemistry models (GCCMs) perform as well as models using input meteorology (CTMs), then the inherent meteorological biases in GCCMs

may be within tolerable bounds. We have shown the AMIP_56 configuration performs better than the CTM_56 configuration in a number of metrics (Table 3.6). This is particularly notable in the response ozone to temperature, particularly on long time scales. We hypothesize the forced meteorology in the offline CTM_56 configuration has introduced biases and errors pertaining to ozone chemistry, particularly in the simulation of the boundary layer. This may have important implications in the interpretation of hindcast simulations as well as the response of offline simulations to heat waves, stagnation events, and synoptic jet stream meteorology. Thus the differences between CTM and GCCM simulations (here CTM_56 and AMIP_56 configurations) should not be attributed solely to differences in GCCM meteorology but also to subtle differences in model formulation. The consistent formulation of model dynamics in the GCCMs may lead to more consistent results.

The largest simulation differences are between versions of the CESM with 56 vertical levels and versions with 26 vertical levels. The 56-level versions have not been tuned for climate applications while the 26-level versions have been tuned. However, our working hypothesis is that the results are more sensitive to the number of levels than the climate tuning. Support for this hypothesis is that for many variables the two 56-level models are more alike than the two 26-level models (Table 3.6 and Figure 3.9). However, additional simulations are needed to better understand the impact of climate tuning on atmospheric chemistry.

Based on these simulation results we would strongly recommend the models with higher vertical resolution be used in simulations of future (and present) atmospheric chemistry. We found that the number of vertical levels has a large impact on ozone chemistry. The online simulation with 56 vertical levels (AMIP_56) produced simulations that are markedly better that the online simulation using 26 vertical levels (AMIP_26) in simulating surface ozone, surface

temperature, and ozone trends, but not better in capturing the ozone-temperature relationship (m_{O3-T}). One of the largest differences between the configurations are the DMT biases, namely that the 26-level configurations simulate statistically significantly higher DMT biases than the 56-level configurations. We find this DMT bias is correlated to many other simulated parameters including, but not limited to, sunlight, cloud cover, and biogenic emissions (Figure 3.9). In all regions, the 26-level configurations show up to 200% higher surface isoprene emissions than the 56-level configurations reflecting higher temperature biases in the 26-level configurations (Figure 3.7).

Studies examining the impact of model resolution on surface chemistry in GCCMs have been largely limited to the impact of changes in horizontal resolution (e.g. Wild and Prather, 2006, Lin et al., 2008). Wild and Prather (2006) found that moving from coarse to fine horizontal resolution simulations does reduce model biases, it does not appear to do so at statistically significant levels. Lin et al. (2009) and Huang et al. (2013) have examined the impact of changes in vertical resolution on surface chemistry for regional chemical transport models. Consistent with our results they found that that increased vertical resolution improves the simulation of surface ozone chemistry largely due to better representation of the near-surface meteorology.

The performance of the configuration with interactive ocean and sea ice (CCM_26) did not produce simulations that were markedly different from the configuration with forced sea surface temperatures and sea ice (AMIP_26). Models with interactive oceans may increase model biases and results taken from such simulations must be treated with caution.

Nevertheless some biases persist in the AMIP_56 configurations. Therefore we recommend caution in the use of GCCMs in simulating surface chemistry. We have shown that meteorological changes due to different model configurations can have strong impacts on the

simulated chemistry. Over the Northeastern US the differences in the temperature, cloudiness, photolysis, isoprene emissions and ozone production are closely related in the different simulations. Generally, cloud cover is highest in simulations with the coldest temperatures. These simulations also have relatively low photolysis rates of NO_2, low isoprene emissions and relatively low net ozone production. Over the Southeastern US anomalous cloud cover in the AMIP_56 simulation has a clear impact on the chemistry terms. These types of errors must be accounted for in the interpretation of GCCM results.

VII. Acknowledgments

This publication was made possible by US EPA grant 83520501 and grant 83428301. Its contents are solely the responsibility of the grantee and do not necessarily represent the official views of the US EPA. Further, US EPA does not endorse the purchase of any commercial products or services mentioned in the publication. The authors also acknowledge the support of NSF grant CNS-0832782. We would also like to acknowledge the helpful advice of Daniel Fuka, Qi Tang, and the climate-chemistry research group at Cornell University. In addition, we would like to thank the guidance of Francoise Vermeylen and Jay Barry of the Cornell University Statistical Consulting Unit for their invaluable help with the Mixed Modeling analysis.

VIII. References

Avise, J., Abraham, R.G., Chung, S.H., Chen, J., Lamb, B., Salathé, E.P., Zhang, Y., Nolte, C.G., Loughlin, D.H., Guenther, A., Wiedinmyer, C., Duhl, T., 2012. Evaluating the effects of climate change on summertime ozone using a relative response factor approach for policymakers. J. Air Waste Manage. Assoc. 62, 1061–1074.

Barnes, E.A., Fiore, A.M., 2013. Surface ozone variability and the jet position: Implications for projecting future air quality. Geophys. Res. Lett. 40, 2839–2844.

Bloomer, B.J., Stehr, J.W., Piety, C.A., Salawitch, R.J., Dickerson, R.R., 2009. Observed relationships of ozone air pollution with temperature and emissions. Geophys. Res. Lett. 36, 1–5.

Bloomer, B.J., Vinnikov, K.Y., Dickerson, R.R., 2010. Changes in seasonal and diurnal cycles of ozone and temperature in the eastern U.S. Atmos. Environ. 44, 2543–2551.

Brasseur, G.P., Hauglustaine, D.A., Walters, S., Rasch, P.J., Mfiller, J., Granter, C., Tie, X.X., 1998. MOZART, a global chemical transport model for ozone and related chemical tracers - 1. Model description. J. Geophys. Res. 103, 28,265–28,289.

Brown-Steiner, B., Hess, P., 2011. Asian influence on surface ozone in the United States: A comparison of chemistry, seasonality, and transport mechanisms. J. Geophys. Res. 116, 1–13.

Camalier, L., Cox, W., Dolwick, P., 2007. The effects of meteorology on ozone in urban areas and their use in assessing ozone trends. Atmos. Environ. 41, 7127–7137.

CASTNET, 2013a. 2011 Annual Report, prepared by AMEC Environment & Infrastructure, Inc. for the US. Environmental Agency, Office of Air and Radiation, Clean Air Markets Division, Washington, D.C. February 2103.

CASTNET, 2013b. CASTNET Factsheet, available at epa.gov/castnet/javaweb/docs/CASTNET_Factsheet_2013.pdf, accessed on October 30, 2014.

Chan, E., Vet, R.J., 2010. Baseline levels and trends of ground level ozone in Canada and the United States. Atmos. Chem. Phys. 10, 8629–8647.

Cooper, O.R., Gao, R.-S., Tarasick, D., Leblanc, T., Sweeney, C., 2012. Long-term ozone trends at rural ozone monitoring sites across the United States, 1990–2010. J. Geophys. Res. 117, 1–24.

Dawson, J.P., Adams, P.J., Pandis, S.N., 2007. Sensitivity of ozone to summertime climate in the eastern USA: A modeling case study. Atmos. Environ. 41, 1494–1511.

Dingenen, R. Van, Dentener, F.J., Raes, F., Krol, M.C., Emberson, L., Cofala, J., 2009. The global impact of ozone on agricultural crop yields under current and future air quality legislation. Atmos. Environ. 43, 604–618.

Doherty, R.M., Wild, O., Shindell, D.T., Zeng, G., MacKenzie, I. A., Collins, W.J., Fiore, A. M., Stevenson, D.S., Dentener, F.J., Schultz, M.G., Hess, P., Derwent, R.G., Keating, T.J., 2013. Impacts of climate change on surface ozone and intercontinental ozone pollution: A multi-model study. J. Geophys. Res. Atmos. 118, 3744–3763.

Duncan, B.N., Yoshida, Y., Olson, J.R., Sillman, S., Martin, R. V., Lamsal, L., Hu, Y., Pickering, K.E., Retscher, C., Allen, D.J., Crawford, J.H., 2010. Application of OMI observations to a space-based indicator of NO_x and VOC controls on surface ozone formation. Atmos. Environ. 44, 2213–2223.

Emmons, L.K., Walters, S., Hess, P.G., Lamarque, J.-F., Pfister, G.G., Fillmore, D., Granier, C., Guenther, A., Kinnison, D., Laepple, T., Orlando, J., Tie, X., Tyndall, G., Wiedinmyer, C., Baughcum, S.L., Kloster, S., 2010. Description and evaluation of the Model for Ozone and Related chemical Tracers, version 4 (MOZART-4). Geosci. Model Dev. 3, 43–67.

Fiore, A.M., Jacob, D.J., Mathur, R., Martin, R. V, 2003. Application of empirical orthogonal functions to evaluate ozone simulations with regional and global models. J. Geophys. Res. 108, 1–10.

Fiore, A.M., Dentener, F.J., Wild, O., Cuvelier, C., Schultz, M.G., Hess, P., Textor, C., Schulz, M., Doherty, R.M., Horowitz, L.W., MacKenzie, I.A., Sanderson, M.G., Shindell, D.T., Stevenson, D.S., Szopa, S., Van Dingenen, R., Zeng, G., Atherton, C., Bergmann, D., Bey, I., Carmichael, G., Collins, W.J., Duncan, B.N., Faluvegi, G., Folberth, G., Gauss, M., Gong, S., Hauglustaine, D., Holloway, T., Isaksen, I.S.A., Jacob, D.J., Jonson, J.E., Kaminski, J.W., Keating, T.J., Lupu, A., Marmer, E., Montanaro, V., Park, R.J., Pitari, G., Pringle, K.J., Pyle, J.A., Schroeder, S., Vivanco, M.G., Wind, P., Wojcik, G., Wu, S., Zuber, A., 2009. Multimodel estimates of intercontinental source-receptor relationships for ozone pollution. J. Geophys. Res. 114, 1–21.

Frossard, L., Rieder, H.E., Ribatet, M., Staehelin, J., Maeder, J.A., Di Rocco, S., Davison, A.C., Peter, T., 2013. On the relationship between total ozone and atmospheric dynamics and chemistry at mid-latitudes – Part 1: Statistical models and spatial fingerprints of atmospheric dynamics and chemistry. Atmos. Chem. Phys. 13, 147–164.

Frost, G.J., McKeen, S.A., Trainer, M., Ryerson, T.B., Neuman, J.A., Roberts, J.M., Swanson, A., Holloway, J.S., Sueper, D.T., Fortin, T., Parrish, D.D., Fehsenfeld, F.C., Flocke, F., Peckham, S.E., Grell, G.A., Kowal, D., Cartwright, J., Auerbach, N., Habermann, T., 2006. Effects of changing power plant NO_x emissions on ozone in the eastern United States: Proof of concept. J. Geophys. Res. 111, 1–19.

Guenther, A.B., 1997. Seasonal and Spatial Variations in Natural Volatile Organic Compound Emissions. Ecol. Appl. 7, 34–45.

Guenther, A.B., Jiang, X., Heald, C.L., Sakulyanontvittaya, T., Duhl, T., Emmons, L.K., Wang, X., 2012. The Model of Emissions of Gases and Aerosols from Nature version 2.1 (MEGAN2.1): an extended and updated framework for modeling biogenic emissions. Geosci. Model Dev. 5, 1471–1492.

Hauglustaine, D.A., Brasseur, G.P., Walters, S., Rasch, P.J., Mfiller, J., Ernrnons, L.K., Carroll, M.A., 1998. MOZART, a global chemiscal transport model for ozone and related chemical tracers 2. Model results and evaluation. J. Geophys. Res. 103, 28,291–28,335.

Heald, C.L., Henze, D.K., Horowitz, L.W., Feddema, J., Lamarque, J.-F., Guenther, A., Hess, P.G., Vitt, F., Seinfeld, J.H., Goldstein, A. H., Fung, I., 2008. Predicted change in global secondary organic aerosol concentrations in response to future climate, emissions, and land use change. J. Geophys. Res. 113, 1–16.

Hegglin, M.I., Shepherd, T.G., 2009. Large climate-induced changes in ultraviolet index and stratosphere-to-troposphere ozone flux. Nat. Geosci. 2, 687–691.

Hess, P., Mahowald, N., 2009. Interannual variability in hindcasts of atmospheric chemistry : the role of meteorology. Atmos. Chem. Phys. 9, 5261–5280.

Hilboll, A., Richter, A., Burrows, J.P., 2013. Long-term changes of tropospheric NO_2 over megacities derived from multiple satellite instruments. Atmos. Chem. Phys. 13, 4145–4169. doi:10.5194/acp-13-4145-2013.

Hu, X.-M., Doughty, D.C., Sanchez, K.J., Joseph, E., Fuentes, J.D., 2012. Ozone variability in the atmospheric boundary layer in Maryland and its implications for vertical transport model. Atmos. Environ. 46, 354–364.

Huang, M., Carmichael, G.R., Chai, T., Pierce, R.B., Oltmans, S.J., Jaffe, D. a., Bowman, K.W., Kaduwela, A., Cai, C., Spak, S.N., Weinheimer, A. J., Huey, L.G., Diskin, G.S., 2013. Impacts of transported background pollutants on summertime western US air quality: model evaluation, sensitivity analysis and data assimilation. Atmos. Chem. Phys. 13, 359–391.

Jacob, D.J., Winner, D.A., 2009. Effect of climate change on air quality. Atmos. Environ. 43, 51–63.

Kim, S.-W., Heckel, A., McKeen, S.A., Frost, G.J., Hsie, E.-Y., Trainer, M.K., Richter, A., Burrows, J.P., Peckham, S.E., Grell, G.A., 2006. Satellite-observed U.S. power plant NO_x emission reductions and their impact on air quality. Geophys. Res. Lett. 33, 1–5.

Kramm, G., Müller, H., Fowler, D., Höfken, K.D., Meixner, F.X., Schaller, E., 1991. A Modified Profile Method for Determining the Vertical Fluxes of NO, NO_2, Ozone, and HNO_3 in the Atmospheric Surface Layer. J. Atmos. Chem. 13, 265–288.

Lai, T.-L., Talbot, R., Mao, H., 2012. An Investigation of Two Highest Ozone Episodes During the Last Decade in New England. Atmosphere. 3, 59–86.

Lam, Y.F., Fu, J.S., Wu, S., Mickley, L.J., 2011. Impacts of future climate change and effects of biogenic emissions on surface ozone and particulate matter concentrations in US. Atmos. Chem. Phys. Discuss. 11, 4789–4806.

Lamarque, J.-F., Bond, T.C., Eyring, V., Granier, C., Heil, A., Klimont, Z., Lee, D., Liousse, C., Mieville, A., Owen, B., Schultz, M.G., Shindell, D., Smith, S.J., Stehfest, E., Van Aardenne, J., Cooper, O.R., Kainuma, M., Mahowald, N., McConnell, J.R., Naik, V., Riahi, K., van Vuuren, D.P., 2010. Historical (1850–2000) gridded anthropogenic and biomass burning emissions of reactive gases and aerosols: methodology and application. Atmos. Chem. Phys. 10, 7017–7039.

Lamarque, J.-F., Emmons, L.K., Hess, P.G., Kinnison, D.E., Tilmes, S., Vitt, F., Heald, C.L., Holland, E. A., Lauritzen, P.H., Neu, J., Orlando, J.J., Rasch, P.J., Tyndall, G.K., 2012.

CAM-chem: description and evaluation of interactive atmospheric chemistry in the Community Earth System Model. Geosci. Model Dev. 5, 369–411.

Lang, C., Waugh, D.W., 2011. Impact of climate change on the frequency of Northern Hemisphere summer cyclones. J. Geophys. Res. 116, D04103.

Langford, A.O., Aikin, K.C., Eubank, C.S., Williams, E.J., 2009. Stratospheric contribution to high surface ozone in Colorado during springtime. Geophys. Res. Lett. 36.

Lin, J., Youn, D., Liang, X., Wuebbles, D., 2008. Global model simulation of summertime U.S. ozone diurnal cycle and its sensitivity to PBL mixing, spatial resolution, and emissions. Atmos. Environ. 42, 8470–8483.

Lin, M., Holloway, T., Oki, T., Streets, D.G., Richter, A., 2009. Multi-scale model analysis of boundary layer ozone over East Asia. Atmos. Chem. Phys. 9, 3277–3301.

Lin, M., Fiore, A.M., Cooper, O.R., Horowitz, L.W., Langford, A.O., Levy, H., Johnson, B.J., Naik, V., Oltmans, S.J., Senff, C.J., 2012a. Springtime high surface ozone events over the western United States: Quantifying the role of stratospheric intrusions. J. Geophys. Res. Atmos. 117, 1-20.

Lin, M., Fiore, A.M., Horowitz, L.W., Cooper, O.R., Naik, V., Holloway, J., Johnson, B.J., Middlebrook, A.M., Oltmans, S.J., Pollack, I.B., Ryerson, T.B., Warner, J.X., Wiedinmyer, C., Wilson, J., Wyman, B., 2012b. Transport of Asian ozone pollution into surface air over the western United States in spring. J. Geophys. Res. Atmos. 117, 1-20.

Lin, M., Horowitz, L.W., Oltmans, S.J., Fiore, A.M., Fan, S., 2014. Tropospheric ozone trends at Mauna Loa Observatory tied to decadal climate variability. Nat. Geosci. 7, 136 – 143.

LRTAP Convention, 2004. Manual on Methodologies and Criteria for Modelling and Mapping Critical Loads and Levels and Air Pollution Effects, Risks and Trends. International Cooperative Programme on Mapping and Modelling under the UNECE Convention on Long-Range Transboundary Air Pollution. Available from: http://www.oekodata.com/icpmapping/.

Masson, D., Knutti, R., 2011. Climate model genealogy. Geophys. Res. Lett. 38, 1–4.

Mauritsen, T., Stevens, B., Roeckner, E., Crueger, T., Esch, M., Giorgetta, M., Haak, H., Jungclaus, J., Klocke, D., Matei, D., Mikolajewicz, U., Notz, D., Pincus, R., Schmidt, H., Tomassini, L., 2012. Tuning the climate of a global model. J. Adv. Model. Earth Syst. 4, 1–18.

McGrath-Spangler, E.L., Denning, A.S., 2013. Global seasonal variations of midday planetary boundary layer depth from CALIPSO space-borne LIDAR. J. Geophys. Res. Atmos. 118, 1–8.

Murazaki, K., Hess, P., 2006. How does climate change contribute to surface ozone change over the United States? J. Geophys. Res. 111, 1–16.

Pickands, III, J., 1975. Statistical Inference Using Extreme Order Statistics. Ann. Stat. 3, 119–131.

Racherla, P.N., Adams, P.J., 2008. The response of surface ozone to climate change over the Eastern United States. Atmos. Chem. Phys. 8, 871–885.

Räisänen, J., 2007. How reliable are climate models? Tellus 59, 2–29.

Rasch, P.J., Mahowald, N.M., Eaton, B.E., 1997. Representations of transport, convection, and the hydrologic cycle in chemical transport models: Implications for the modeling of short-lived and soluble species. J. Geophys. Res. 102, 28127–28138.

Rasmussen, D.J., Fiore, A.M., Naik, V., Horowitz, L.W., McGinnis, S.J., Schultz, M.G., 2012. Surface ozone-temperature relationships in the eastern US: A monthly climatology for evaluating chemistry-climate models. Atmos. Environ. 47, 142–153.

Reidmiller, D.R., Fiore, A.M., Jaffe, D.A., Bergmann, D., Cuvelier, C., Dentener, F.J., Folberth, G., Gauss, M., Gong, S., Hess, P., Jonson, J.E., Keating, T., Lupu, A., Marmer, E., Park, R., Schultz, M.G., Shindell, D.T., Szopa, S., Vivanco, M.G., Wild, O., Zuber, A., 2009. The influence of foreign vs. North American emissions on surface ozone in the US. Atmos. Chem. Phys. 9, 5027–5042.

Ribatet, M., 2012. POT: Generalized Pareto Distribution and Peaks Over Threshold. R package version 1.1-3. http://CRAN.R-project.org/package=POT.

Rieder, H.E., Fiore, A.M., Polvani, L.M., Lamarque, J.-F., Fang, Y., 2013a. Changes in the frequency and return level of high ozone pollution events over the eastern United States following emission controls. Environ. Res. Lett. 8, 1–10.

Rieder, H.E., Frossard, L., Ribatet, M., Staehelin, J., Maeder, J.A., Di Rocco, S., Davison, A.C., Peter, T., Weihs, P., Holawe, F., 2013b. On the relationship between total ozone and atmospheric dynamics and chemistry at mid-latitudes – Part 2: The effects of the El Niño/Southern Oscillation, volcanic eruptions and contributions of atmospheric dynamics and chemistry to long-term total ozone. Atmos. Chem. Phys. 13, 165–179.

Rienecker, M.M., Suarez, M.J., Gelaro, R., Todling, R., Bacmeister, J., Liu, E., Bosilovich, M.G., Schubert, S.D., Takacs, L., Kim, G.-K., Bloom, S., Chen, J., Collins, D., Conaty, A., da Silva, A., Gu, W., Joiner, J., Koster, R.D., Lucchesi, R., Molod, A., Owens, T., Pawson, S., Pegion, P., Redder, C.R., Reichle, R., Robertson, F.R., Ruddick, A.G., Sienkiewicz, M., Woollen, J., 2011. MERRA: NASA's Modern-Era Retrospective Analysis for Research and Applications. J. Clim. 24, 3624–3648.

Roberts, J.M., Marchewka, M., Bertman, S.B., Goldan, P., Kuster, W., de Gouw, J., Warneke, C., Williams, E., Lerner, B., Murphy, P., Apel, E., Fehsenfeld, F.C., 2006. Analysis of the isoprene chemistry observed during the New England Air Quality Study (NEAQS) 2002 intensive experiment. J. Geophys. Res. 111, 1–9.

Russell, A.R., Valin, L.C., Cohen, R.C., 2012. Trends in OMI NO_2 observations over the United States: effects of emission control technology and the economic recession. Atmos. Chem. Phys. 12, 12197–12209.

Schultz, M.G., Heil, A., Hoelzemann, J.J., Spessa, A., Thonicke, K., Goldammer, J.G., Held, A.C., Pereira, J.M.C., van het Bolscher, M., 2008. Global wildland fire emissions from 1960 to 2000. Global Biogeochem. Cycles 22, 1–17.

Schumann, U., Huntrieser, H., 2007. The global lightning-induced nitrogen oxides source. Atmos. Chem. Phys. Discuss. 7, 2623–2818.

Sillman, S., Samson, P.J., 1995. Impact of temperature on oxidant photochemistry in urban, polluted rural and remote environements. J. Geophys. Res. 100, 11,497–11,508.

Smith, R.J., 2009. Use and misuse of the reduced major axis for line-fitting. Am. J. Phys. Anthropol. 140, 476–86.

Steiner, A.L., Davis, A.J., Sillman, S., Owen, R.C., Michalak, A.M., Fiore, A. M., 2010. Observed suppression of ozone formation at extremely high temperatures due to chemical and biophysical feedbacks. Proc. Natl. Acad. Sci. U. S. A. 107, 19685–19690.

Tuovinen, J.-P., Simpson, D., Emberson, L., Ashmore, M., Gerosa, G., 2007. Robustness of modelled ozone exposures and doses. Environ. Pollut. 146, 578–586.

Turner, A.J., Fiore, A.M., Horowitz, L.W., Bauer, M., 2013. Summertime cyclones over the Great Lakes Storm Track from 1860–2100: variability, trends, and association with ozone pollution. Atmos. Chem. Phys. 13, 565–578.

US EPA, 1998. Finding of Significant Contribution and Rulemaking for Certain States in the Ozone Transport Assessment Group Region for Purposes of Reducing Regional Transport of Ozone, 40 CFR Parts 51, 72, 75, and 96 [FRL-6171-2], RIN 2060-AH10, Federal Register, Vol. 63, No. 207, 57356-57538.

US EPA, 2005. August 2005 Report: Evaluating Ozone Control Programs in the Eastern United States: Focus on the NO_x Budget Trading Program, 2004. Available at: http://www.epa.gov/airtrends/2005/ozonenbp/.

US EPA, 2008. National Ambient Air Quality Standards for Ozone: Final Rule. Federal Register, Vol. 73, No. 60, 16436-16514.

Val Martin, M., Heald, C.L., Arnold, S.R., 2014. Coupling dry deposition to vegetation phenology in the Community Earth System Model: Implications for the simulation of surface O_3. Geophys. Res. Lett. 41.

Wang, H., Jacob, D.J., Le, P., Streets, D.G., Park, R.J., Gilliland, A.B., Donkelaar, A. Van, 2009. Surface ozone background in the United States : Canadian and Mexican pollution influences. Atmos. Environ. 43, 1310–1319.

Weaver, C.P., Cooter, E., Gilliam, R., Gilliland, A., Grambsch, A., Grano, D., Hemming, B., Hunt, S.W., Nolte, C., Winner, D.A., Liang, X.-Z., Zhu, J., Caughey, M., Kunkel, K., Lin, J.-T., Tao, Z., Williams, A., Wuebbles, D.J., Adams, P.J., Dawson, J.P., Amar, P., He, S., Avise, J., Chen, J., Cohen, R.C., Goldstein, A.H., Harley, R.A., Steiner, A.L., Tonse, S., Guenther, A., Lamarque, J.-F., Wiedinmyer, C., Gustafson, W.I., Leung, L.R., Hogrefe, C., Huang, H.-C., Jacob, D.J., Mickley, L.J., Wu, S., Kinney, P.L., Lamb, B., Larkin, N.K., McKenzie, D., Liao, K.-J., Manomaiphiboon, K., Russell, A.G., Tagaris, E., Lynn, B.H., Mass, C., Salathé, E., O'neill, S.M., Pandis, S.N., Racherla, P.N., Rosenzweig, C., Woo, J.-H., 2009. A Preliminary Synthesis of Modeled Climate Change Impacts on U.S. Regional Ozone Concentrations. Bull. Am. Meteorol. Soc. 90, 1843–1863.

Wild, O., Prather, M.J., 2006. Global tropospheric ozone modeling : Quantifying errors due to grid resolution. J. Geophys. Res. 111, 1–14.

Wu, S., Mickley, L.J., Leibensperger, E.M., Jacob, D.J., Rind, D., Streets, D.G., 2008. Effects of 2000 – 2050 global change on ozone air quality in the United States. J. Geophys. Res. Geophys. Res. 113, 1–12.

IX. APPENDIX (INCLUDING SUPPLEMENTAL MATERIAL)

Mixed Modeling

We used Mixed Modeling (MM) (see Baayen et al., 2008) for much of the statistical analysis in this study in order to determine statistical differences between the CASTNET observations and between the various simulations. This analysis is conducted using the R-Project Linear Mixed Effect Model Using S4 Classes (lme4) library (Bates et al., 2013) to create each linear MM and the Least-Squares Means (lsmeans) library (Lenth, 2013) for the statistical significance testing. A full description of Linear MM in R can be found in Bates (2013) and references therein. Linear MM assumes that both the fixed and random effects have a linear form. The predictor variable is estimated by summing estimated regression coefficients for each fixed effect and each random effect individually, plus a residual error term. In each data table in this paper, and using the MM analysis mentioned above, significance testing was conducted both between CASTNET observations and each of the four individual configurations. All significance testing was conducted at the $p < 0.05$ level.

Details of Scaling to 10 meter Ozone

Here we describe the method of estimating ozone values at the 10-meter height of the EPA CASTNET observational stations rather than the bottom grid cell height output by the model. A more complete description and discussion of this method can be found in LRTAP (2004).

The concentration of a chemical species at a particular height (z_1) is found with:

$$C(z_1) = C(z_R) * [1 - (R_a(z_R, z_1) * V_g(z_R))]$$

where

$$R_a(z_R, z_1) = \frac{1}{ku^*} \ln\left(\frac{z_R - d}{z_1 - d}\right)$$

and

$$u^* = \frac{u(z)k}{\ln\left(\frac{z-d}{z_0}\right)}$$

Here:

$C(z_1)$	=	concentration at z_1
$C(z_R)$	=	concentration at z_R
d	=	displacement height (d = 0.7 m)
k	=	von Kármán constant (k = 0.4)
$R_a(z_R,z_1)$	=	aerodynamic resistance between two heights (s m^{-1})
u(z)	=	wind speed at height z (m s^{-1})
u^*	=	friction velocity (m s^{-1})
$V_g(z)$	=	deposition velocity at height z (m s^{-1})
z_0	=	level at which R_a becomes zero (m)
z_1	=	desired height (m)
z_R	=	reference height (m)

References

Baayen, R.H., Davidson, D.J., Bates, D.M., 2008. Mixed-effects modeling with crossed random effects for subjects and items. J. Mem. Lang. 59, 390–412.

Bates, D., 2013. Linear mixed model implementation in lme4. Ms., University of Washington – Madison.

Bates, D., Maechler, M., Bolker, B and Walker, S., 2013. lme4: Linear mixed-effects models using S4 classes. R package version 1.1-6. http://CRAN.R-project.org/package=lme4

Lenth, R.V., 2013. Least-squares means (lsmeans). R-Package, version 1.10-01. http://cran.r-project.org/web/packages/lsmeans.

LRTAP Convention, 2004. Manual on Methodologies and Criteria for Modelling and Mapping Critical Loads and Levels and Air Pollution Effects, Risks and Trends. International Cooperative Programme on Mapping and Modelling under the UNECE Convention on Long-Range Transboundary Air Pollution. Available from: http://www.oekodata.com/icpmapping/.

Supplemental Tables

S4.1: Emissions Comparison for Asia, US, Global to ACCMIP and E2010/L2012

	ACCMIP*			E2010/L2012**			This project		
Tg(species) yr^{-1}	Asia	U.S.	Global	Asia	U.S.	Global	Asia	U.S.	Global
CB1	2.44	0.38	6.21	2.28	0.34	5.56	2.39	0.37	5.94
CB2	0.61	0.09	1.55	0.57	0.09	1.39	0.60	0.09	1.48
BIGALK	9.29	12.4	40.9	10.4	13.0	75.8	8.73	5.76	37.0
BIGENE	2.77	1.23	6.53	3.35	1.27	8.13	3.00	0.69	8.52
C_2H_4	10.3	2.08	30.8	6.35	0.95	16.4	6.49	1.05	17.4
C_2H_5OH	1.36	0.20	2.91	2.40	0.60	5.78	1.84	0.28	5.86
C_2H_6	3.04	0.33	6.65	3.01	1.22	10.9	2.68	0.32	6.64
C_3H_6	4.92	0.79	13.5	2.20	0.33	5.33	2.51	0.37	6.00
C_3H_8	1.81	0.37	5.84	2.11	0.79	10.6	1.63	0.49	6.36
CH_2O	2.34	0.34	9.03	0.95	0.20	3.19	1.20	0.32	5.42
CH_3CHO	1.82	0.10	4.33	1.40	0.35	6.94	1.80	0.18	6.71
CH_3COCH_3	1.15	0.23	4.27	4.74	1.90	27.0	5.04	2.04	27.8
CH_3OH	43.8	10.7	173	45.7	18.9	237	46.5	19.0	239
CO	418	130	1,160	395	110	1,120	376	120	1,130
MEK	1.01	0.28	3.75	0.93	0.40	5.83	1.10	0.34	6.09
NH_3	24.7	4.10	59.3	30.2	3.56	64.9	18.7	4.25	53.4
NO	21.0	16.8	95.3	22.5	15.8	88.6	24.2	17.1	96.0
OC1	6.10	0.50	18.0	5.76	0.90	17.3	4.89	0.54	15.6
OC2	6.10	0.50	18.0	5.76	0.90	17.3	4.89	0.54	15.6
SO_2	34.0	22.0	117	47.4	20.6	143	37.8	18.4	116
TOLUENE	10.3	4.83	28.2	9.31	6.19	31.8	8.84	3.05	23.8

*: ACCMIP emissions described in Lamarque et al. [2010] and accessed through CESM CAM-Chem distribution

**: E2010/L2012 emissions described in Emmons et al. [2010] & Lamarque et al. [2012] and accessed through CESM CAM-Chem distribution

S4.2: Division of Annual Emissions by All Sectors for All Species for the year 2000

Tg(species) yr^{-1}	anthro	fires	biogenic	soil	ocean	volcano	total
CB1	4.12	1.82	0	0	0	0	5.94
CB2	1.03	0.45	0	0	0	0	1.48
BIGALK	32.3	4.72	0	0	0	0	37.0
BIGENE	4.85	3.67	0	0	0	0	8.52
C_2H_4	7.75	4.67	5.01	0	0	0	17.4
C_2H_5OH	2.84	3.02	0	0	0	0	5.86
C_2H_6	3.35	2.29	1.00	0	0	0	6.64
C_3H_6	3.47	1.54	1.00	0	0	0	6.00
C_3H_8	3.87	0.49	2.00	0	0	0	6.36
CH_2O	3.18	2.23	0	0	0	0	5.42
CH_3CHO	1.92	4.79	0	0	0	0	6.71
CH_3COCH_3	1.10	2.17	24.5	0	0	0	27.8
CH_3OH	1.98	6.68	230	0	0	0	239
CO	610	336	160	0	19.9	0	1,130
MEK	1.37	4.72	0	0	0	0	6.09
NH_3	37.6	5.20	0	2.44	8.18	0	53.4
NO	68.5	10.4	0	17.1	0	0	96.0
OC1	6.35	9.23	0	0	0	0	15.6
OC2	6.35	9.23	0	0	0	0	15.6
SO_2	104	2.02	0	0	0	9.59	116
TOLUENE	21.3	2.49	0	0	0	0	23.8

S4.3: Total Annual Emissions (Sum of All Sectors) for All Species from 1994 – 2005

Tg(species) yr^{-1}	1994	1995	1996	1997	1998	1999	2000	2001	2002	2003	2004	2005
CB1	6.03	5.86	5.87	6.97	7.10	6.19	5.94	6.14	6.38	6.27	6.40	6.47
CB2	1.51	1.47	1.47	1.74	1.78	1.55	1.48	1.53	1.59	1.57	1.60	1.62
BIGALK	37.1	36.5	36.3	41.0	41.1	38.1	37.0	37.1	37.8	37.2	37.8	36.9
BIGENE	6.73	6.33	6.67	10.74	11.09	9.08	8.52	8.60	9.21	8.80	9.27	8.62
C_2H_4	19.2	18.2	18.1	21.8	21.4	18.4	17.4	17.9	18.7	18.3	18.9	19.1
C_2H_5OH	3.34	3.35	3.66	7.41	7.79	6.23	5.86	5.98	6.53	6.26	6.69	6.21
C_2H_6	7.42	6.85	6.85	9.26	8.90	7.22	6.64	6.91	7.41	7.16	7.62	7.70
C_3H_6	8.10	7.32	7.28	7.17	7.32	6.28	6.00	6.14	6.45	6.39	6.44	6.49
C_3H_8	7.55	7.08	7.08	6.55	6.67	6.40	6.36	6.42	6.53	6.53	6.55	6.59
CH_2O	7.66	7.16	7.36	7.29	8.03	5.86	5.42	5.51	6.32	6.37	6.12	6.15
CH_3CHO	4.89	4.51	4.49	9.57	10.17	7.41	6.71	7.11	7.82	7.58	7.66	7.75
CH_3COCH_3	28.4	28.1	28.1	29.0	29.2	28.1	27.8	28.0	28.2	28.1	28.2	28.3
CH_3OH	228	226	226	243	243	240	239	239	240	240	240	240
CO	1,200	1,150	1,150	1,350	1,380	1,180	1,130	1,150	1,200	1,180	1,170	1,180
MEK	8.69	8.39	7.67	8.61	9.17	6.70	6.09	6.24	7.05	6.57	7.21	6.41
NH_3	58.2	56.2	55.9	57.7	57.7	54.6	53.4	54.3	55.3	55.5	56.1	56.7
NO	102	101	101	99.4	102	96.9	96.0	97.0	98.1	97.9	97.8	98.2
OC1	16.8	15.6	16.1	20.8	23.4	16.9	15.6	16.1	18.2	18.1	17.2	17.3
OC2	16.8	15.6	16.1	20.8	23.4	16.9	15.6	16.1	18.2	18.1	17.2	17.3
SO_2	129	126	124	123	121	118	116	117	119	120	121	122
TOLUENE	23.1	22.8	22.7	25.5	26.1	24.3	23.8	24.1	24.7	24.9	24.8	24.9

S4.4: DM8H O_3 Bias for Each Site and Configuration By Region and Latitude

				DM8H O3 Mean and Standard Deviations									
				CASTNET		CTM_56		AMIP_56		AMIP_26		CCM_26	
	Site	lats	lons	mean	s.d.	mean	s.d.	mean	s.d.	mean	s.d.	mean	s.d.
NE	ASH135	46.6	-68.4	36.82	10.67	59.80	16.67	60.57	15.91	62.23	17.41	62.77	17.88
	HOW132	45.2	-68.7	38.85	12.56	72.20	20.42	70.48	17.55	72.46	20.41	73.42	19.92
	WST109	43.9	-71.7	37.65	11.50	71.00	18.44	69.96	16.44	73.59	19.28	74.02	18.56
	UVL124	43.6	-83.4	50.17	16.48	69.11	17.20	67.56	15.79	75.02	20.87	75.87	20.34
	ANA115	42.4	-83.9	54.14	15.52	74.54	16.36	75.40	13.75	86.31	19.04	87.28	18.12
	CTH110	42.4	-76.7	52.74	13.28	79.06	18.06	76.12	16.30	85.36	20.76	85.66	20.49
	ABT147	41.8	-72.0	54.45	19.33	85.37	23.32	81.32	17.61	87.65	21.67	88.98	20.62
	MKG113	41.4	-80.1	56.21	16.06	82.82	17.68	80.76	14.45	93.75	17.80	94.62	16.89
	LYK123	40.9	-83.0	57.63	14.91	76.53	15.68	76.35	13.30	87.78	16.30	88.71	15.60
	SAL133	40.8	-85.7	56.80	13.69	76.76	15.02	77.03	13.21	88.56	15.69	89.49	14.71
	WSP144	40.3	-74.9	60.64	20.83	93.23	25.77	91.33	18.61	103.44	24.70	106.65	23.18
	LRL117	40.0	-79.3	52.06	14.41	89.28	18.57	86.09	14.43	99.07	18.61	99.93	17.63
	ARE128	39.9	-77.3	61.12	16.00	85.46	17.65	82.27	14.88	92.48	18.56	93.35	17.74
	OXF122	39.5	-84.7	58.53	14.79	89.59	17.65	84.83	15.48	100.23	17.39	100.51	16.78
	PAR107	39.1	-79.7	53.82	13.34	83.79	13.19	81.75	11.88	90.46	13.25	91.42	12.61
	BEL116	39.0	-76.8	62.38	20.17	92.15	19.42	89.16	15.22	100.60	18.90	101.85	17.26
	CDR119	38.9	-80.8	49.42	13.85	91.05	16.31	86.62	13.45	98.82	15.46	99.90	15.16
	ALH157	38.9	-89.6	59.79	14.74	82.93	15.30	79.42	14.11	90.91	13.93	90.89	14.73
	VIN140	38.7	-87.5	56.99	13.59	83.84	15.55	80.78	14.27	93.38	14.68	93.46	14.95
	MCK231	37.7	-85.0	59.33	14.08	88.52	15.63	79.51	15.70	92.32	16.12	91.12	16.22
	VPI120	37.3	-80.6	58.59	12.75	82.40	13.15	77.34	12.65	85.32	12.83	85.63	12.91
SE	SPD111	36.5	-83.8	56.35	13.21	85.76	14.10	78.31	13.85	89.40	14.93	88.90	14.77
	CND125	35.3	-79.8	55.50	17.05	81.07	19.36	77.06	15.80	85.73	17.83	87.35	17.12
	COW137	35.1	-83.4	44.48	13.07	85.69	15.43	74.35	14.41	83.69	15.70	83.27	15.25
	BFT142	34.9	-76.6	46.90	14.84	70.02	21.25	71.22	17.54	75.71	20.83	79.49	20.16
	SND152	34.3	-86.0	57.85	15.69	82.58	14.02	69.59	14.97	79.27	16.03	77.97	15.85
	CVL151	34.0	-89.8	50.25	15.00	73.73	14.88	57.23	13.45	63.59	14.66	62.54	14.58
	SUM156	30.1	-85.0	39.14	14.37	51.61	17.25	42.88	10.38	42.62	8.86	42.82	9.55
West	PND165	42.9	-109.8	56.54	6.85	58.26	6.63	64.16	5.89	66.80	5.71	66.31	5.45
	CNT169	41.4	-106.2	58.71	7.41	60.32	6.61	66.68	6.05	69.18	6.32	68.80	6.49
	LAV410	40.5	-121.6	54.45	10.45	50.71	11.05	61.30	7.92	65.19	9.02	64.57	9.25
	GTH161	39.0	-107.0	55.55	7.09	59.77	6.97	66.41	6.40	68.00	6.45	67.74	6.99
	CAN407	38.5	-109.8	58.82	6.99	60.72	7.17	68.03	6.21	69.59	6.40	69.03	6.88
	YOS404	37.7	-119.7	68.56	11.92	69.94	13.79	73.45	8.55	77.68	9.89	75.94	10.19
	MEV405	37.2	-108.5	56.30	7.32	59.87	7.64	67.96	6.69	69.25	6.76	68.81	7.37
	DEV412	36.5	-116.8	63.68	9.04	62.91	8.46	66.67	6.70	69.37	6.91	68.15	7.74
	PIN414	36.5	-121.2	56.52	13.31	57.79	15.35	62.34	10.46	65.69	10.57	65.07	11.62
	GRC474	36.1	-112.2	57.38	7.59	60.46	8.17	68.13	6.54	69.98	6.84	69.11	7.23

S4.5: DMT Bias for Each Site and Configuration By Region and Latitude

				DMT Mean and Standard Deviations									
				CASTNET		CTM_56		AMIP_56		AMIP_26		CCM_26	
	Site	lats	lons	mean	s.d.	mean	s.d.	mean	s.d.	mean	s.d.	mean	s.d.
NE	ASH135	46.6	-68.4	21.45	4.44	20.85	3.60	24.84	4.10	26.82	4.64	27.75	4.81
	HOW132	45.2	-68.7	22.83	4.42	20.51	3.01	24.90	3.36	26.28	4.04	28.96	4.22
	WST109	43.9	-71.7	21.83	3.93	21.88	3.42	25.89	3.61	27.98	4.34	29.03	4.50
	UVL124	43.6	-83.4	24.25	4.24	22.56	3.74	27.72	3.77	30.90	4.54	31.49	4.91
	ANA115	42.4	-83.9	24.69	4.03	24.84	3.65	28.33	3.58	32.24	4.53	32.76	4.74
	CTH110	42.4	-76.7	21.59	4.00	23.65	3.47	26.22	3.25	29.23	3.97	30.10	4.30
	ABT147	41.8	-72.0	22.85	3.81	23.29	3.27	27.11	3.46	29.01	4.27	30.56	4.38
	MKG113	41.4	-80.1	23.96	3.87	25.64	3.29	27.66	3.39	32.10	4.29	32.64	4.49
	LYK123	40.9	-83.0	25.04	3.83	26.43	3.44	28.62	3.64	33.41	4.42	33.87	4.59
	SAL133	40.8	-85.7	25.58	3.92	27.49	3.76	29.59	3.86	34.54	4.75	35.01	4.81
	WSP144	40.3	-74.9	26.01	4.04	25.38	3.38	27.91	3.10	30.24	3.95	31.77	4.03
	LRL117	40.0	-79.3	22.78	3.65	25.05	3.34	26.97	3.30	30.84	4.02	31.49	4.21
	ARE128	39.9	-77.3	25.38	4.00	25.26	3.52	27.02	3.18	30.32	4.07	31.31	4.12
	OXF122	39.5	-84.7	26.30	3.61	27.66	3.28	28.77	3.64	33.88	4.24	34.32	4.46
	PAR107	39.1	-79.7	24.50	3.46	25.22	3.23	26.13	3.39	30.31	3.79	30.87	3.90
	BEL116	39.0	-76.8	27.02	4.09	27.73	3.55	29.46	3.21	32.31	4.06	33.58	4.09
	CDR119	38.9	-80.8	25.64	3.30	27.63	3.27	28.77	3.57	33.50	3.99	33.94	4.21
	ALH157	38.9	-89.6	27.34	3.87	29.38	3.83	31.18	4.47	36.79	4.77	37.00	4.85
	VIN140	38.7	-87.5	27.83	3.63	28.81	3.59	30.20	4.07	35.75	4.49	36.08	4.67
	MCK231	37.7	-85.0	26.85	3.36	29.48	3.34	30.13	4.07	35.74	4.11	36.17	4.46
	VPI120	37.3	-80.6	22.35	3.21	26.42	2.91	26.71	3.52	31.33	3.71	31.87	3.74
SE	SPD111	36.5	-83.8	26.68	3.10	28.06	2.93	28.47	3.70	33.56	3.84	34.01	4.08
	CND125	35.3	-79.8	28.12	3.79	29.36	3.03	29.66	3.12	33.18	3.63	33.94	3.55
	COW137	35.1	-83.4	24.62	2.94	28.43	2.83	27.78	3.59	32.79	3.57	33.08	3.61
	BFT142	34.9	-76.6	27.03	2.33	28.56	2.34	28.96	2.31	30.99	2.69	31.85	2.67
	SND152	34.3	-86.0	27.13	3.13	29.44	2.97	29.37	3.80	34.70	3.66	34.98	3.86
	CVL151	34.0	-89.8	29.19	3.24	31.11	2.86	30.64	3.63	36.15	3.14	36.39	3.59
	SUM156	30.1	-85.0	29.08	2.81	28.94	1.21	28.27	1.00	29.66	1.19	29.72	1.21
West	PND165	42.9	-109.8	19.37	5.11	21.08	5.00	26.23	4.25	28.51	3.99	28.68	4.18
	CNT169	41.4	-106.2	13.09	4.58	23.19	4.51	28.29	3.74	29.76	3.41	29.93	3.78
	LAV410	40.5	-121.6	20.76	4.94	26.37	5.11	31.32	5.07	34.21	5.25	34.41	5.59
	GTH161	39.0	-107.0	16.31	4.08	21.33	3.93	26.04	3.39	26.76	3.05	27.03	3.28
	CAN407	38.5	-109.8	27.46	4.44	28.33	4.11	32.99	3.55	34.46	3.30	34.64	3.49
	YOS404	37.7	-119.7	23.10	4.37	29.16	4.47	34.00	4.20	35.84	4.16	36.06	4.27
	MEV405	37.2	-108.5	24.82	4.20	29.79	3.60	33.93	3.51	35.06	3.27	35.32	3.40
	DEV412	36.5	-116.8	42.35	3.69	29.21	4.02	32.56	3.78	34.58	3.64	34.57	3.71
	PIN414	36.5	-121.2	29.61	4.61	15.93	1.28	19.45	2.10	18.85	2.12	21.59	2.35
	GRC474	36.1	-112.2	24.75	4.17	29.07	3.96	33.51	3.69	34.92	3.37	35.24	3.34

CHAPTER 4: BLACK CARBON EMISSIONS FROM TRUCKS AND TRAINS IN THE MIDWESTERN AND NORTHEASTERN UNITED STATES FROM 1977 – 2007

Benjamin Brown-Steiner, Peter Hess, Jialie Chen, Kieran Donaghy

I. Abstract

We have developed a framework to estimate BC emissions from trucks and trains in the transportation sector in the Midwestern and Northeastern United States (MNUS) from available economic data from 1977 – 2007. We first expand on previous development of a regional econometric input-output model (REIM) that has been used to estimate commodity flows between 13 states (plus the rest of the US) and 13 sectors. These commodity flow data are then distributed over the MNUS region using a link-and-node network, which creates great circle transportation links between nodes in each state at the county with the largest population. Freight flows are converted to BC transportation emissions using the best available data and the resulting BC emissions are comparable to the MACCity and HTAPv2 existing BC emissions inventories of the MNUS region from 1977 - 2007. This link-and-node distribution methodology distributes emissions over an idealized transportation network. We find that from 1977 – 2007 the continued increase in freight tonnage in the MWUS is counteracted by decreases in the BC emission factors in heavy-duty diesel trucks, which results in a decrease of BC emissions by 2007. Two sectors (fabricated metal and construction) have dominated the BC transportations emissions throughout 1977 to 2007 with fabricated metal emissions decreasing after 2000 and construction emissions increasing throughout the period. The BC transportation emissions are concentrated in and around the urban centers, which serve as transportation and production nodes and decrease in the transportation corridors and in rural areas in the MNUS region. This framework established in this study can be used to estimate future BC transportation emissions under a set of stylized economic, technological, and regulatory scenarios.

II. Introduction

Black Carbon (BC) aerosols are a human health hazard (e.g. Janssen et al., 2012) with emissions from all sources having a net radiative forcing on the order of 1 W m^{-2} of which nearly one-third is attributed to fossil fuel combustion (Bond et al., 2013). In industrialized nations, including the US, where biomass burning emissions are relatively low, on-road diesel vehicles in the transportation industry are the dominant source of BC emissions (Bond et al., 2013). The transportation industry in the US has transformed dramatically since the 1970s: freight volumes have nearly tripled, increasing at a rate that is faster than the growth of US GNP (US DOT, 2013); emission factors for BC from diesel trucks, which account for over 50% of US BC transportation emissions (US EPA, 2012a), have declined by nearly 80% (US EPA, 2012a; US EPA, 2012b); and the transportation sector has transformed as a part of an increasingly interconnected global economy that is dependent on just-in-time deliveries of both intermediate and finished commodities (Donaghy, 2012).

The ultimate impact of an increased demand for transportation and a concurrent decrease in BC emission factors is complicated. This paper examines the factors by which freight flows impact BC emissions in the Midwestern and Northeastern US (MNUS) over a historical period (1977 – 2007). We use a regional econometric model to describe the historical time series of freight flows and historical emission factor (EF) changes to estimate gridded BC emissions. We are also able to isolate the BC emissions that result from the individual influences of the economic and the regulatory sectors. These results, provide us with the capability to examine future BC emissions under a variety of economic and regulatory scenarios.

There have been many influences on BC emissions resulting from freight transportation in the MNUS from 1977 - 2007. The majority of BC emissions from the transportation sector

come from the heavy-duty diesel vehicle (HDDV) fleet with a minor contribution from railroads (ICF, 2005). The HDDV and railroads transport freight based upon demand from producers of finished and semi-finished goods, which themselves are driven by the dynamics of both regional and global economies including growth, supply and demand, and globalization. At the same time, particulate matter (PM) emissions, and therefore also BC emissions, have been subject to increasingly stringent regulatory efforts from the US EPA (US EPA, 2012a) and from local municipalities (e.g. NYSDEC, 2014). Here we briefly review the changes in the transportation and economic sector and changes in the regulatory sector that have impacted BC emissions during the historical period.

Nationally the volume (as value) of freight movement is growing at an annual rate of roughly 5% which is more than twice as fast as the growth of the country's Gross National Product (GNP) (US DOT, 2013). Much of the increase in demand for freight shipment is the result of aggregated economic growth as well as changes in the geography of production (e.g. Feenstra, 1998; Donaghy, 2007). In addition to these broad growth trends, the transportation sector has experienced changes in the process and geography of the production of goods. Advancements in information technologies has increase the efficiency and reliability of the freight transportation sector, which in turn has allowed industries to transition to a "just-in-time" inventory management system where products can be shipped quickly in an "on-demand" basis (e.g. Krishnamurthy, 2007). Subsequently the industrial production process has grown more dependent upon the transportation sector, with a growing trend towards regular shipments of unfinished goods between production centers throughout the production process (Castells, 2000). Essentially, industries are able to take advantage of regional economies of scale (Feenstra, 1998) and economies of scope (Jones and Kierzkowski, 2001), which has resulted in a "hollowing out"

and “clustering” of production and transportation nodes (Munroe et al., 2007). An example is the regular transportation of unfinished automobile parts between Canada and the US (Anderson and Coates, 2010), where car parts experience multiple border crossings throughout the production process (Anderson, 2012). This is a significant change from the traditional vertically-integrated, or traditional assembly line production process (Feenstra, 1998).

Concurrently, the US EPA and regional municipalities have become increasingly aware of the negative health effects of BC emissions (e.g. Annenberg et al. 2012) and have indirectly promulgated increasingly stringent controls on BC through by continuously tightening the National Ambient Air Quality Standard (NAAQS) for all particulate matter (PM) (US EPA, 2012a, 2012b, 2013). This, combined with a continued increase in technological efficiencies in transportation technologies has resulted in the HDDV EF of BC to drop from 1.29 μg/g in 1977 to 0.39 μg/g in 2007 (from the US EPA MOVES software, US EPA 2012b). This downward trend in BC emission standards is expected to continue into the future.

This study, while limited in scope compared to other BC emissions inventories, provides us with the ability to examine the economic and regulatory trends described above. We can isolate the impact of globalization and EF changes on the final BC emissions in order to understand the overall mechanisms controlling and driving BC emissions in the MNUS. Instead of distributing emissions based on a population proxy we distribute emissions based on an idealized transportation network that allows us to examine sub-regional impacts of the transportation sector on BC air quality. We compare our methodology to other existing BC emissions inventories and explore the strengths and weaknesses of our BC emissions. Finally, the framework created in this paper allows for the direct estimation of future BC emissions under a variety of economic, technological, and regulatory scenarios.

Section 2 describes the methodology of this study, including details of the REIM input and output, the conversion and distribution process, and the format and caveats of the resultant BC emissions. Section 3 evaluates these BC emissions against existing BC emission inventories. Section 4 explores the results of these BC emissions including the interaction between increasing freight volume and decreasing emission factors, the major contributing sectors and their trends, and the regional impact of BC emissions in the Midwestern and Northeastern US.

III. Methods

Figure 4.1: Study region. Black dots indicate location of each state's most populous county (US Census, 2010) used as the nodes for distribution of emissions. One additional county (San Francisco County, California) serves as the node for the Rest of the US (RUS) region.

Table 4.1. Region Input-Output Table Sector Definitions

Sector	Description	Abbreviations	Commodity Flow Conversion (millions of dollars per kiloton)	NAICS Code
1	Agriculture, forestry, fishing, and hunting	agricu	0.88	11
2	Mining	mining	0.26	21
3	Construction	constr	0.18	23
4	Food product manufacturing	foodpm	1.40	311
5	Chemical manufacturing	chemmf	2.01	325
6	Primary metal manufacturing	pmetal	1.18	331
7	Fabricated metal product manufacturing	fmetal	0.06	332
8	Machinery manufacturing	machin	9.41	333
9	Computer and electronic product manufacturing	comput	22.0	334,335
10	Transportation Equipment	treqpt	7.72	336
11	Other Non-durable Manufacturing	ondrmf	1.56	312-316,322-324,326
12	Other Durable Manufacturing	odrmfr	1.63	321,327,337,339
13	TCU, Services and Government Enterprises	govten	3.10	42,44,45,48,49,51-56,61,62,71,72,81

Table 4.2: Emission Factors Used for Paper. HDDV are from MOVES. Locomotives are from US EPA (2009).

	grams BC per ton-km	
	HDDV	Locomotives
1977	0.06	0.01
1990	0.03	0.01
2000	0.02	0.01
2005	0.01	0.01
2007	0.01	0.01

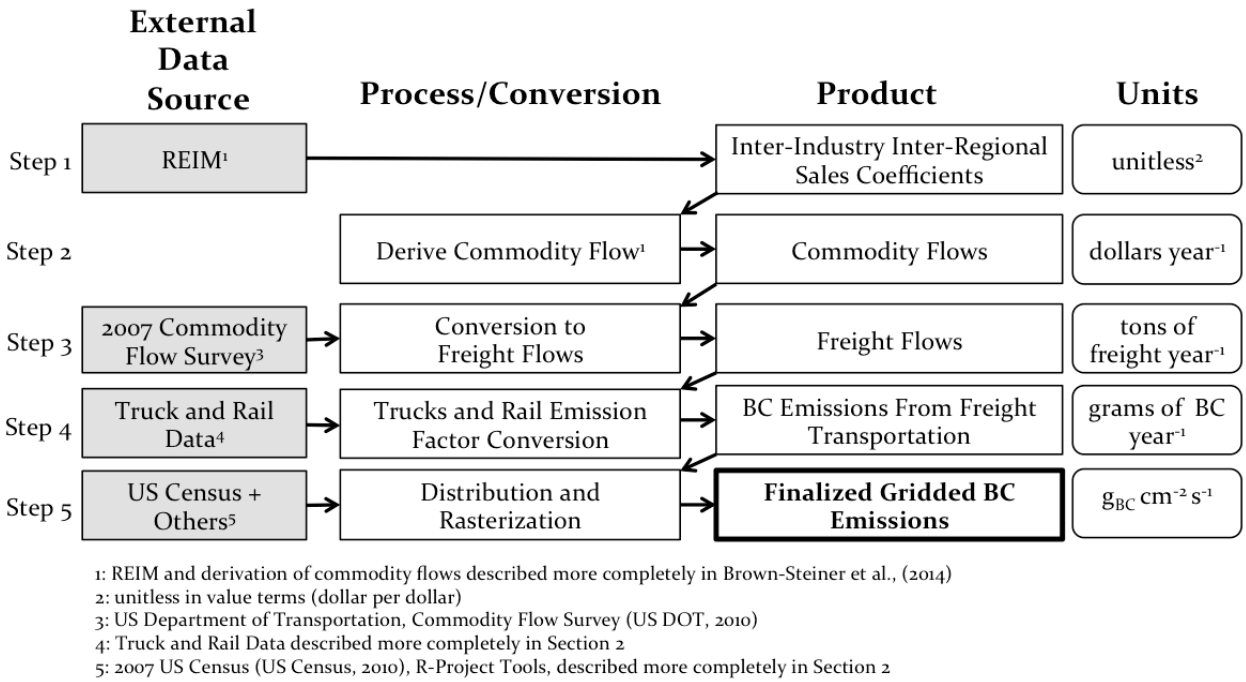

Figure 4.2: Process Schematic for this paper. Section 2 follows and describes in more complete detail the central two columns of this Figure. The leftmost column indicates which external data sources were utilized in this study. The rightmost column indicates the units of the product in the corresponding row.

In this section we detail the process and steps taken to estimate BC emissions from initial economic and industry data. We focus on flows between 13 industrial sectors (Table 4.1) located in 13 states in the Northeastern and Midwestern US (Figure 4.1) and between these states and the rest of the US (RUS). We first take available economic time-series data tracking intersectoral and interstate commodity flows in value terms (dollars per year) as detailed in Donaghy and Chen (2011) and Brown-Steiner et al. (in press). We then take these commodity flows and convert then to freight flows (in tons of freight shipped per year) using conversion factors from the Commodity Flow Survey (US DOT, 2010). We then convert the freight flows to BC emissions (g BC per year) from truck and trail transportation making assumptions from available literature. Finally, these BC emissions are then distributed between population centers and gridded to produce a stylized representation of the spatial structure of BC emissions from

transportation (g m^2 s^{-1}) in our MNUS region. The conversion process is schematically represented in Figure 4.2 and should be used as a reference for understanding the following section.

In order to produce freight flows in our region, it was necessary to first create a time series of inter-state and inter-industry commodity flows for each industry in each state for each year. Unfortunately, annual reporting of these data is not available and thus must be created based on the data from the years in which they are reported. The first step (Figure 4.2) to create these desired data takes initial data from the US Bureau of Economic Analysis (BEA) (available at http://www.bea.gov/itable/) and the US Bureau of Labor Statistics (BLS) from 1977 – 2007 (e.g. government spending, economic output, employment) and develops a dynamic multi-regional econometric input-output model (REIM). REIMs are a powerful tools that allow for analysis and interpretation of unexpected and non-linear changes in regional economies (e.g. Donaghy et al., 2007, Tao et al., 2007), which can create a flow of commodities between industries and states in value terms (dollars per year). The available commodity flows are used to estimate the inter-industry and inter-state sales coefficients from which we derived interstate inter-industry sales. The annual interstate and inter-industry sales coefficients (input-output flows in terms of a portion of total value) are extracted following the methods of Israilevich et al. (1997), which creates 2,366 time-series of sales coefficients (13 sectors x 13 sectors x 13 states plus the RUS). For a more complete description of this REIM see Donaghy and Chen (2011) and Brown-Steiner et al. (in press).

These interstate and inter-industry sales coefficients are then converted to commodity flows (in dollars per year, Step 2 in Figure 4.2). The interstate and inter-industry sales coefficients are benchmarked following the approach developed in Jackson et al. (2006) to

estimate interregional commodity flow demand, total commodity production, and total industrial output from data on consumption, investment, and government spending (Brown-Steiner et al., in press). From these data we can then derive the commodity flows (dollars per year). These sales coefficients and the derived commodity flows describe the region's overall freight activities. The commodity flow data can also be used to estimate structural parameters (referred to in the econometric literature as scale, factor-intensity, and substitution parameters, see Ferguson, 1969) which can in turn be used to forecast future trends under a set of scenarios. For this project, however, we examine only the historical (1977 – 2007) commodity flow data and the effects on BC emissions.

The commodity flows (dollars per year) are converted to freight tonnage per year using the conversion factor (in millions of constant year-2001 US dollars per kiloton of freight) taken from the US DOT Commodity Flow Survey for each sector (2007) (Table 4.1) (Step 3 in Figure 4.2). Shipments between the various sectors can either be intrastate or interstate. Intrastate shipments (within a single state) are spatially allocated to each county in each state based on the county's population (US Census, 2010). Interstate shipments are allocated using a link-and-node model. This model creates a single node in each state at the center of the county with the highest population (Figure 4.1) (US Census, 2010) and connects these nodes with a great-circle path. The node for the Rest of the US (RUS) is specified as San Francisco County, California. Each individual node has a path to every other node (for a total of 105 links between 14 nodes including the RUS). We do not include changing population demographics, which increased by roughly 10% during this historical period (Figure 4.6). While the actual transportation system in the US is more complicated, this assumption broadly distributes transportation emissions over the MNUS region. Mode implications of this choice of the RUS node are explored below.

The allocation of BC emissions by mode (Step 4 in Figure 4.2) distributes BC emissions along the links connecting each state node by: (1) multiplying the length of the great-circle link by the total tons of freight shipped for each industry (ton-km); and (2) creating a composite emission factor ($EF_{BC,comp}$ in grams of BC emitted per ton-km) which combines the emission factors from for trucks and rail transportation individually ($EF_{BC,trucks}$ and $EF_{BC,rail}$, respectively). A time-varying emission factor of BC from heavy-duty trucks was obtained from default MOVES simulations (in grams BC emitted per km) (see http://www.epa.gov/otaq/models/moves/). We assumed an average of 25 tons of freight per truck to get an estimate of the BC emissions factor from trucks (grams of BC emitted per ton-km for trucks). While HDDV particulate mater emissions standards have decreased by over 99% during the historical period (US EPA, 2012b), the realized emission factor has not decreased as dramatically as older model HDDVs are phased out of the active fleet. For rail, estimates of BC emissions is limited, both due to large uncertainties but also due to limited reporting form the rail industry. We estimate a best guess from the limited available data for the PM10 emission factor of 0.01 grams of PM10 per ton-km for rail (NESCAUM, 2006; US EPA, 2009) and we assume, on average, that BC makes up roughly 4% of the PM10 mass fraction (e.g. Handa et al., 2010; Perez et al., 2010; Yttri et al., 2007) to get a final estimate of the BC emission factor from rail (g BC emitted per ton-km for rail). This emissions factor for rail emissions does not change over time. Table 4.2 summarizes the emission factors per ton-km for HDDV and rail sources.

We then create the composite BC emission factor ($EF_{BC,comp}$) by distributing the relative percentage of ton-miles shipped by trucks (PTM_{trucks}) and trains (PTM_{trains}) (ICF, 2005) using the following equation:

$$EF_{BC,comp}(y) = \left[EF_{BC,trucks}(y)PTM_{trucks}(y) + EF_{BC,trains}PTM_{trains}(y)\right] \quad (1)$$

Here the suffix (y) indicates the parameter evolves over time (1977 – 2007). $EF_{BC,comp}$ has the units of grams of BC emitted per kilometer of the combined truck and rail fleet. While many of these HDDV and railroad parameters vary over time, by commodity, and by region, we apply a single best-guess value over our entire study area. This is in part due to the lack of available regional estimates of these parameters and in part due to the scope and goals of this study. Next, this $EF_{BC,comp}$ is multiplied by the great-circle distance along each link between each connecting node (D_i^s) and the tons shipped along that link (T_i^s) and converted to BC emissions using the following equation:

$$E_{BC}(y) = EF_{BC,comp}(y)D_i^s(y)T_i^s(y) \qquad (2)$$

The final units of E_{BC} is in grams of BC emitted per year.

We next distribute both intrastate and interstate BC emissions (grams of BC per year) by rasterizing each individually rasterized onto a 0.5˚x0.5˚ grid (to produce units of grams of BC cm^{-2} s^{-1}) and sum the two together to create gridded emissions (Step 5 in Figure 4.2). Intrastate BC emissions are distributed across all counties in a given state using county-level population data as a proxy. Interstate BC emissions are allocated uniformly onto every grid cell that touches the great-circle freight flow paths connecting each node. This process utilized the following tools from the R-Project (http://www.R-Project.org/): maptools (Bivand et al., 2013), raster (Hijmans and Etton, 2013), ncdf (Pierce, 2014), sp (Pebesma et al., 2005; Bivand et al, 2008), and classInt (Bivand, 2012). An evaluation of our data with MACCity and other BC emissions inventories is found below in Section 3.

Surface BC emissions are nearly all from rail and truck transportation modes (Uherek et al., 2010) so we neglect all BC transportation sources besides rail or truck. In 2007, trucks shipped roughly 69% and rail only 15% of total tonnage (Margreta et al., 2009), but due to the

preferential use of rail for heavy freight and long distances the rail mode transports more ton-miles (ICF, 2005). However, trucks are preferentially utilized for short-haul shipments, which accounted for nearly 80% of the total tonnage shipped in 2002 (US DOT, 2002). Since the 1970s, the distribution of freight among trucks and rail has remained largely unchanged although the volume has increased steadily (ICF, 2005). Since 1990 fuel use for both trucks and rail has increased by 30% despite increases in overall transport efficiency (ICF, 2005).

In order to conduct a preliminary analysis of inter-regional and inter-industry emissions from freight transportation and since this project is limited in scope compared to global emissions inventories, the method described above has several limitations that derive from our scope and our chosen assumptions. First, our chosen region neglects freight transportation to and from Canada, which has traditionally been the largest destination for US exports and source of US imports until China recently topped Canada in US imports (Anderson and Coates, 2010). For example, automobiles and automobile parts cross the US-Canada border between Michigan state and Ontario province multiple times during the production cycle (Anderson, 2012). We do not include these in our study. Second, while choosing San Francisco County as the node for the RUS region adequately represents the east-west transportation corridors in the US, it neglects much of the north-south transportation corridors between the Midwest/Northeast region and the South/Southeast region. Third, the large temporal and spatial differences in many of the parameters used in our conversion process (e.g. regional distributions of HDDV and railroad technologies and infrastructure) would necessitate a much more thorough analysis, such as that done by HTAP2. For our limited study, simplifying assumptions were made, as described above. Finally, our use of great-circle pathways between nodes does not reflect the actual transportation

corridors in the US highway system, although it does create stylized corridors, which we inspect and analyze below.

IV. Comparison Against Standard Existing BC Emissions Inventories

Here we evaluate our BC emissions to other existing BC emission inventories. We primarily compare our BC emissions to the MACCity emissions (available at http://accent.aero.jussieu.fr/MACC_metadata.php/) since the MACCity emissions have the most complete temporal coverage (1960 – 2010). The MACCity emissions are based on the ACCMIP emissions (available at http://accent.aero.jussieu.fr/ACCMIP_metadata.php/) for 1990 and 2000 and the RCP8.5 emissions for 2000 and 2010. The MACCity emissions give priority to regional emission over global emissions inventories (Lamarque et al, 2010). The BC transportation emissions for all regions in the ACCMIP emissions, and thus the MACCity emissions, trace back to Bond et al. (2007), which themselves are an extension of BC inventories developed in Bond et al. (2004). The Bond et al. (2004) inventory is a global inventory and used International Energy Agency (IEA) fuel consumption data and country-specific fuel, technology, and sector divisions in order to estimate BC emissions based on fuel type, and distributed emissions based on a population proxy. Thus we expect geographic differences between our results and MACCity results, but not temporal regionally averaged emission differences. We also compare our BC emissions against the HTAPv2 emissions, which are the highest resolution BC emissions inventory available for this region. Unfortunately, the high resolution has limited the temporal coverage of this inventory to only the years 2008 and 2010 and a full description of the HTAPv2 process is not yet published (although the emissions are available online at http://edgar.jrc.ec.europa.eu/htap_v2/index.php?SECURE=123).

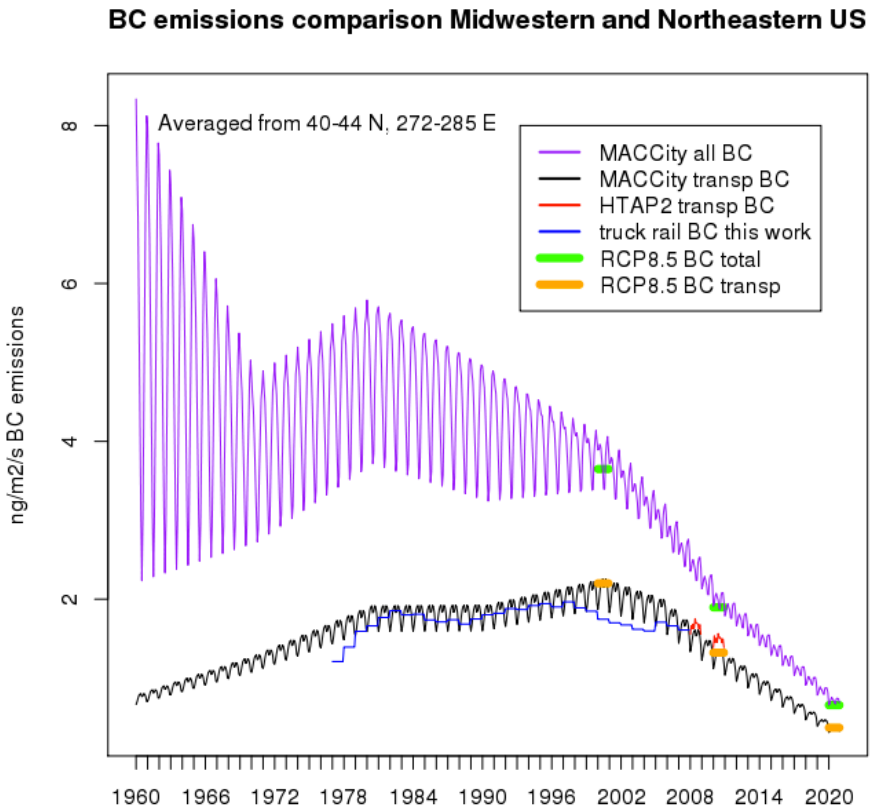

Figure 4.3: Time Series of BC Emissions over this study region (Figure 4.1) from 1960 – 2020 from available existing inventories and this study (blue). MACCity transportation emissions (black) have been scaled by a factor of 0.93, which is an estimate of the percent of mobile source emissions that come from diesel fuels (US EPA, 2012a).

Figure 4.3 compares the temporal trends of BC emissions in the 13 states in our MNUS region (see Figure 4.1) from 1977 - 2007 to BC emissions from: MACCity (1960-2020), HTAPv2 (2008 and 2010), and RCP8.5 (2000, 2010, and 2020). For the MACCity and RCP8.5 emissions, both total BC emissions and the transportation sector emissions are plotted. It can be clearly seen that the transportation BC emissions have become a greater proportion of the total BC emissions over time. The US EPA estimates that mobile sources in the US accounted for 52.8% of all BC emissions in 2005 (US EPA, 2012a), which is also reflected in the MACCity total and transportation BC emissions plotted in Figure 4.3. Our BC emissions closely follow the MACCity transportation emissions with a slight negative bias, most prominent in 1977 – 1981 and 2000 - 2005. While the MACCity emission increasing BC emissions up until 1980, a plateau

from 1980 to 1990, an increase from 1990 to 2000, and then decreases afterward, our emissions show a sharp increase from 1977 – 1981, little change until 1998, and then a decrease out to 2007.

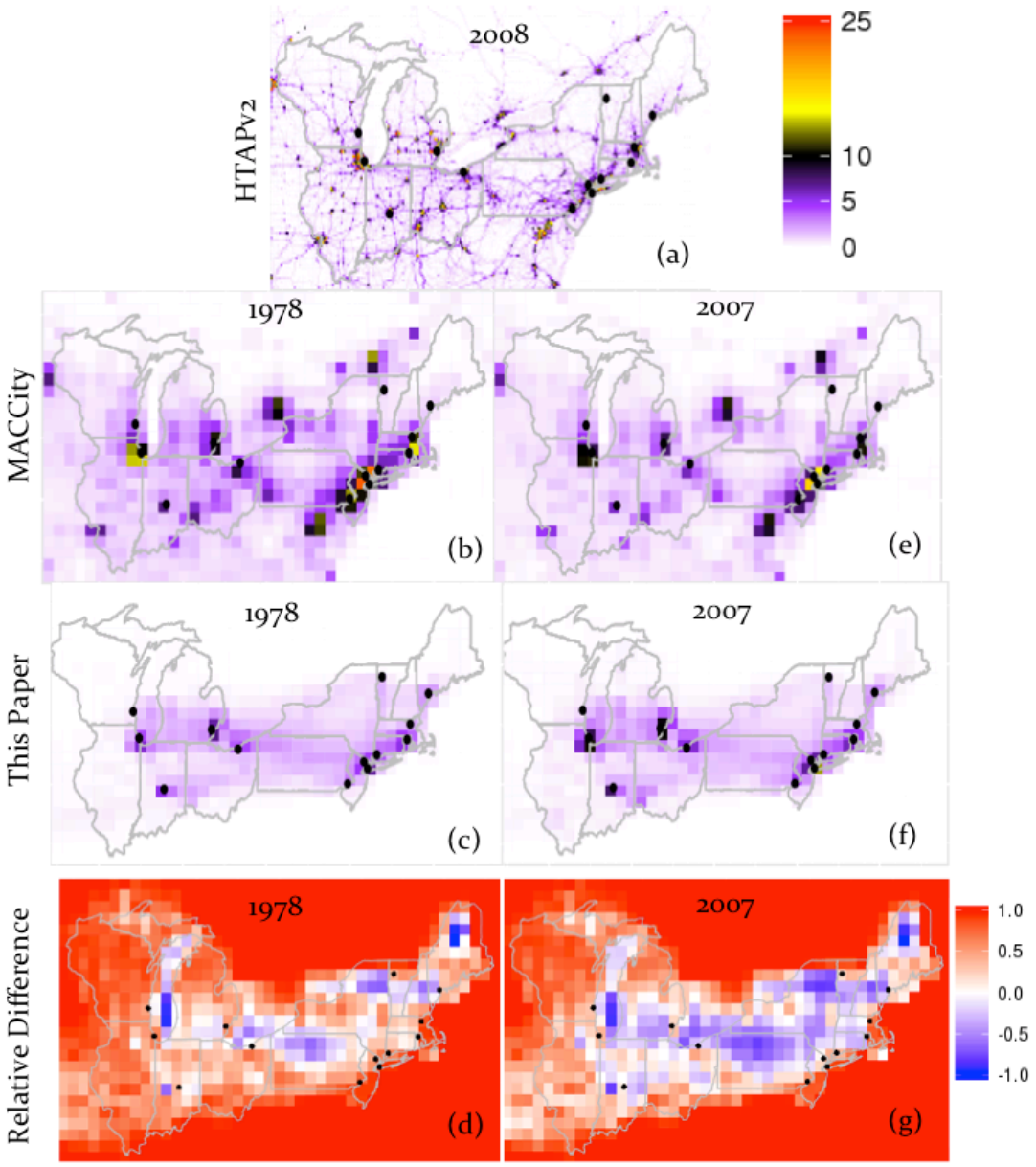

Figure 4.4: Total BC transportation emissions from: (a) HTAPv2 for 2008; (b) MACCity for 1978; (c) our study for 1978; (d) the Relative Difference between MACCity and our results for 1978; (e) MACCity for 2007; (f) our study for 2007; and (g) the Relative Difference between MACCity and our results for 2007. Relative Difference is defined as (MACCity – Our Results)/(MACCity + Our Results). Black dots mark the counties of highest population in each state (same as in Figure 4.1) which serve as the nodes in our distribution process (Section 2). For (d) and (g) warm colors indicate MACCity is higher, cool colors indicate our emissions are higher.

Figure 4.4 compares the spatial distribution of our 2007 BC emissions to the 2007 MACCity transportation BC emissions and the 2008 HTAPv2 emissions. The HTAPv2 emissions are at 0.1˚x0.1˚ resolution, and thus resolve individual highways in the US transportation network. Both the urban centers and the transportation corridors can be seen, and the HTAPv2 BC emissions are distributed across much of the US. In contrast, it can be clearly see that the MACCity BC emissions are distributed by population, clustering around major urban centers and not showing BC emissions distributed along expected transportation corridors. Our emissions are distributed both at urban centers and between urban centers along idealized great-circle transportation corridors, and thus are in between the high-resolution HTAPv2 emissions and the population-proxy MACCity emissions. The largest differences between our emissions and the MACCity emissions are in areas where our results have distributed BC emissions between cities and the MACCity emissions have not. We compare by utilizing the relative difference between the MACCity emissions and our emissions with warm colors indicating the MACCity emissions are greater and cool colors indicating our emissions are greater. The largest differences are noted along our idealized east-west transportation corridor, where our BC emissions are ~50% higher that the MACCity emissions. This is due to our treatment of the transportation network (see Section 2). Over the central portion of our region, the MACCity emissions are between 0 – 50% higher than our emissions. Near the edges of our region the relative difference between the MACCity emissions and our emissions approach 100%, as we did not simulate transportation patterns near our outside our study region.

V. Results

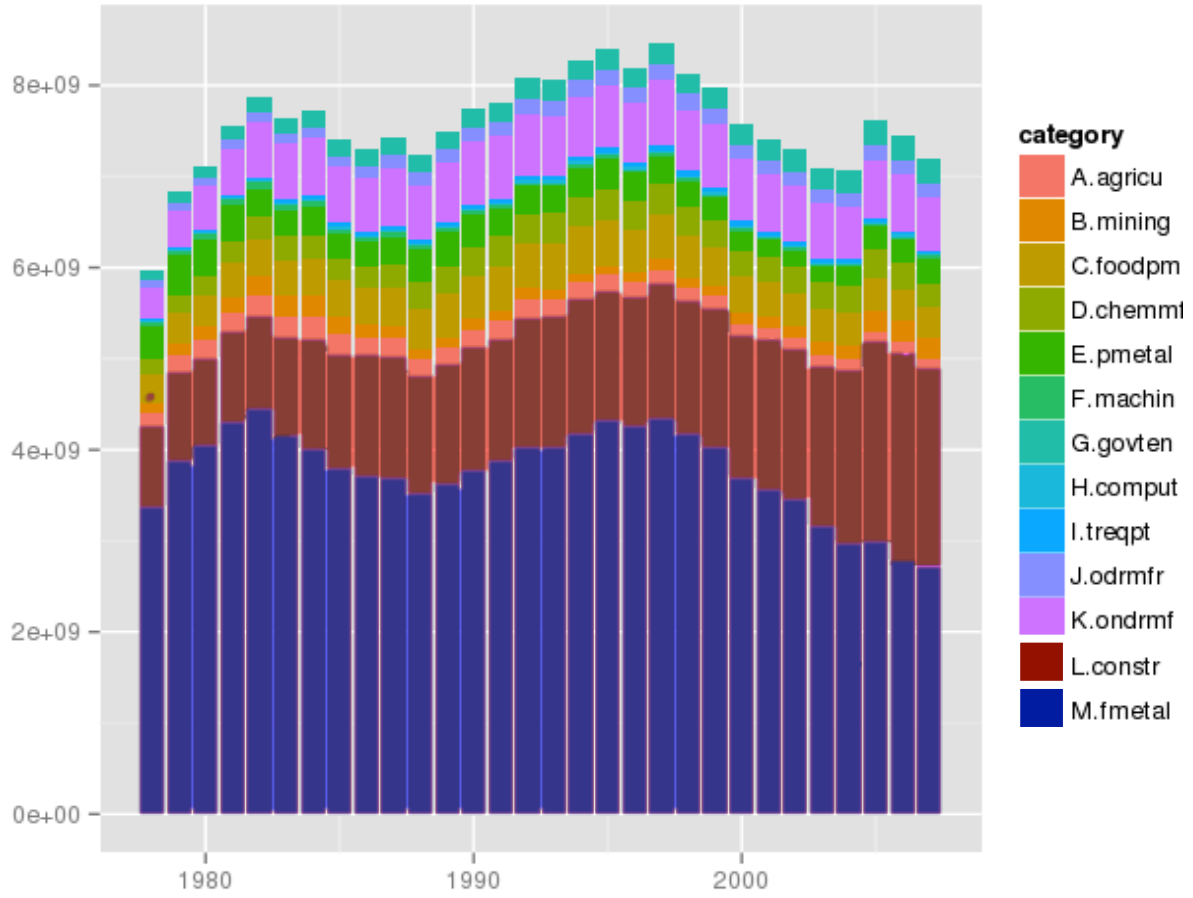

Figure 4.5: Stacked Bar Plots of BC Emissions over the entire study region from 1977 – 2007 by Sector.

Figure 4.5 plots the total BC emissions over our region divided by the 13 sectors (Table 4.1) for each year from 1977 – 2007. Two sectors dominate the BC emissions: the fabricated metal sector (FMETAL) and the construction sector (CONST). Both these sectors are relatively small contributors to overall economic output (e.g. Tao et al., 2010), but both regularly transport heavy freight. Figure 4.5 shows that the BC emissions from fabricated metal transportation approached 60% of the total emissions in 1977 and had generally decreased ever since, dropping to around 36% by 2007. Concurrently, construction emissions contributed roughly 14% of the

total BC emissions in 1977 and had steadily increased its contribution reaching 30% by 2007. All other sectors account for only 26% of total BC emissions in 1977 and 33% in 2007.

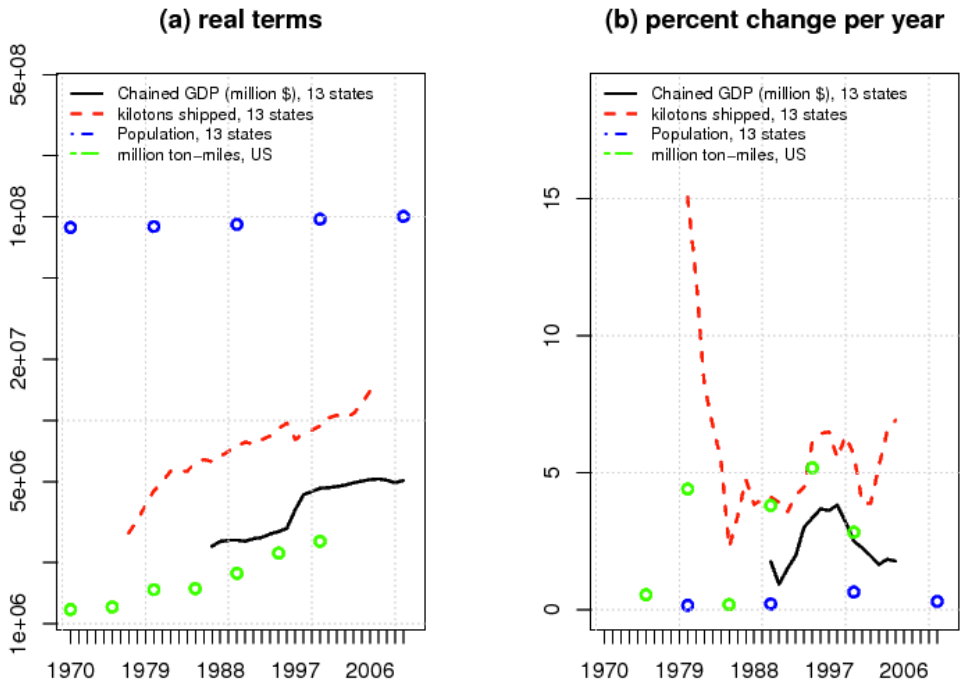

Figure 4.6: (a) Real Terms and (b) Percent Change Per Year for: chained GDP in millions of dollars (black) from http://www.bea.gov for the 13 states in this study, kilotons freight shipped (red) from this study from all regions, population (blue) for the 13 states in our region (from the 2010 US Census), and million ton-miles from HDDV and railroad transportation (green) for all US (US DOT, 2005). Note the jump in chained GDP in (a) in the year 1997 is due to a change in methods from the BTS database (see http://www.bea.gov/regional/docs/product/). Pre-1997 GDP is in chained 1997 dollars and post-1997 GDP is in chained 2009 dollars. GDP in 1997 is the average of the two databases. For both Chained GDP and kilotons of freight shipped in (b) the 5-year moving average is plotted.

One way to explain the trends in BC emissions over the historical period is to examine the concurrent trends in population growth, GDP growth, and freight dynamics. Figure 4.6 plots these together both in real terms (Figure 4.6a) and in the percent change per year (Figure 4.6b). Between 1977 and 2007, the population, GDP, tons shipped and ton-miles of freight increased (Figure 4.6a). However, the growth in total transported tonnage is nearly double the growth in real GDP over the same period for the 13 states in our region (Figure 4.6b). The growth in total ton-miles fluctuated, sometimes growing at the same pace as the total tonnage shipped and

sometimes growing at a smaller pace, or not growing at all (Figure 4.6b). We will further analyze these factors when we examine trends in individual sectors below.

The methodology utilized to produce the region's BC emissions (Section 2) allows us to separate these competing influences. We can keep the BC emission factor constant at 1977 levels while allowing the transportation changes to occur to produce one set of BC emissions (EF_{const}). We can also keep the transportation constant at 1977 levels while allowing the BC emission factor changes to proceed as they have historically (TR_{const}). By comparing these two trends we can explore the underlying causes of the total BC emissions plotted in Figure 4.5.

The total BC emissions, plus the EF_{const} and TR_{const} emissions are plotted together in Figure 4.7. The black lines in Figure 4.7 are the total BC emissions from each sector (and the black line from Figure 4.7a matches the total BC emissions plotted in Figure 4.6. The red line in in Figure 4.7a shows that, if there were not reductions in the BC emission factor, BC emissions would increase just as the freight volume increased (Figure 4.6).

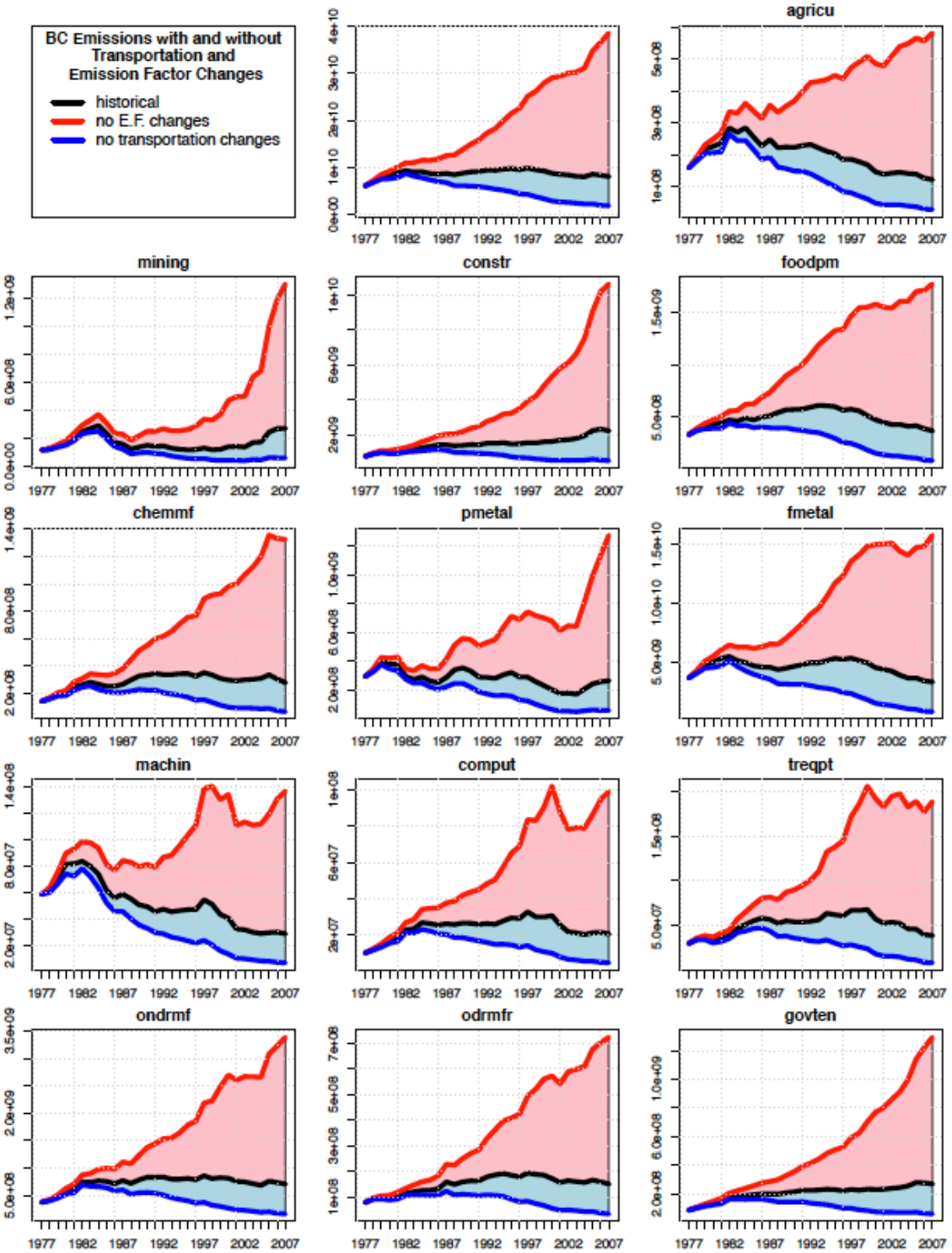

Figure 4.7: Historical time series of total BC emissions (top middle) and each individual sector for the study region (black), plus theoretical emissions if emission factors were held constant at 1977 levels (red) and if shipping/transportation volumes were held constant at 1977 levels (blue). Note that the vertical axis is not the same for each sector.

Inspection of individual sectors in Figure 4.7 allows us to explain some of the trends in total BC emissions from Figure 4.6. The volume of fabricated metal freight grew rapidly from 1985 – 2000 but leveled off out to 2007 (Figure 4.7h). The other sectors that show a decrease or plateau towards the end of the historical period are the machine equipment sector (Figure 4.7i), the computer equipment sector (Figure 4.7j), and the transportation equipment sector (Figure 4.7k). At the same time the volume of construction freight has been increasing continuously since 1977 (Figure 4.7d). In addition, the agricultural (Figure 4.7b), mining (Figure 4.7c), chemical manufacturing (Figure 4.7f), primary metal manufacturing (Figure 4.7g), other manufacturing (Figure 4.7l,m) and the government services (Figure 4.7n) sectors show continuous growth throughout the historical period.

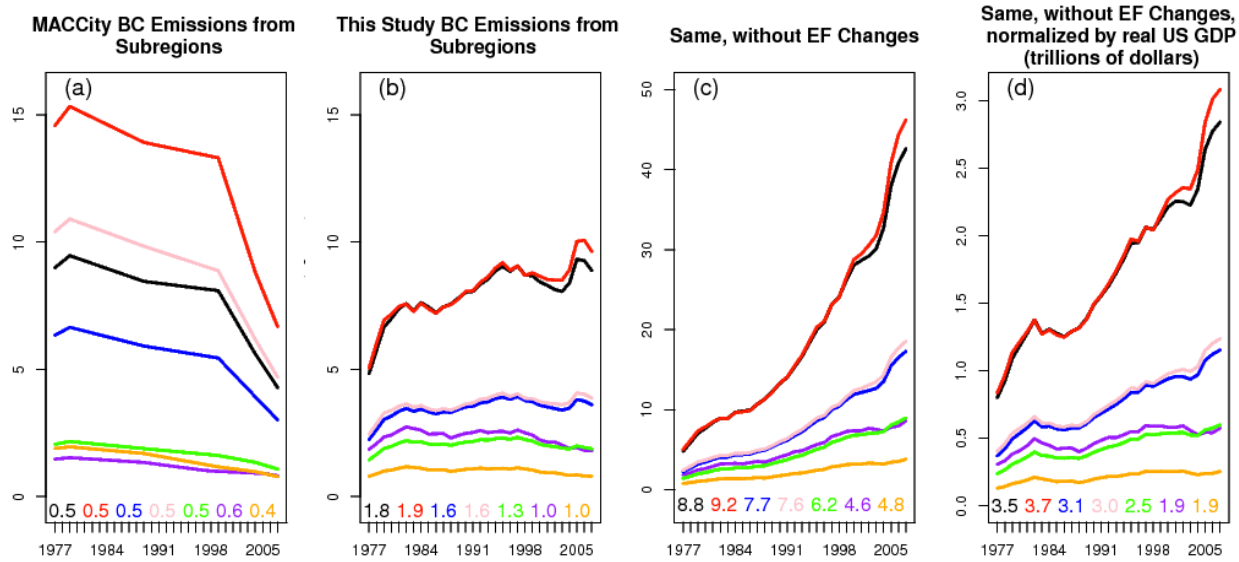

Figure 4.8: BC Emissions from various sub regions for: (a) MACCity, total BC; (b) this study, total; (c) this study with EF_{const}, which includes changes to BC emission factor and the center plot has removed changes due to emission factor changes (i.e. they are held constant at 1977 levels); and (d) which normalizes (c) with respect to the real US GDP (in trillions of dollars) over the historical period. Note the different scales in each of the various plots. The black and red lines represent an average of 6 major cities, and just New York City and Boston, respectfully. The blue and pink lines are the greater urban areas surrounding all cities (blue) and New York City and Boston (pink). The green and purple lines are the Midwestern Corridor (between Cleveland/Detroit and Chicago) and the Northeastern Corridor (between New York City/Boston and Cleveland), respectfully. The numbers at the bottom of each plot are the relative difference between 2007 and 1977 for each trend.

The spatial distribution of the transportation changes (and subsequent BC emission changes) is not uniform in our region (Figure 4.4), and we expect to see a "hollowing out" (Munroe et al., 2007) of certain industries as production centers become more centralized (Donaghy, 2012). Evidence of this would include shifts in emissions in certain sectors to particular areas or a concentration of emissions to developing production centers (with a corresponding decrease of emissions in other regions). Figure 4.8 divides BC emissions among the following sub-regions: the six biggest urban centers (1 grid cell each), the six biggest urban centers and their greater area (each grid cell adjacent to and including the urban center grid cells), a corridor between the Northeastern NYC/Boston zone and the Midwest (roughly 3 grid cells wide connecting the NYC/Boston urban area to the Cleveland/Detroit urban area), a corridor between various cities in the Midwest (roughly 3 grid cells wide connection Cleveland/Detroit to Chicago/Minneapolis in the northwest and Indianapolis to the southwest), and a rural zone away from major corridors (in northern New York and Vermont). Figure 4.8 also plots the average for New York City and Boston together. In urban centers between 1977 and 2007, BC emissions have increased by nearly a factor of 2 (Figure 4.8a) and the greater urban centers show an increase of a factor of approximately 1.5. Transportation corridors and rural zones show little or no change in BC emissions.

Figure 4.8 also plots the BC emissions where we hold the BC emission factor constant, BC_{const} (Figure 4.8b) and where the BC_{const} emissions are normalized by the US Real GDP over the historical period, which increased by roughly 2.5 times from 1977 to 2007 (Figure 4.8c). We can see in Figure 4.8b that growth in BC emissions due to increases in transportation from the urban and greater urban centers increase to a greater degree (with a factor of 8 – 9) than the corridors and rural area (with a factor of 5 – 6). Even when normalized by the Real GDP, the

urban and great urban areas increased would have increased by 3 – 3.5 times their 1977 values if BC emission factors had not changed while the transportation corridors and rural area would have increased by only 2 – 2.5 times (Figure 4.8c).

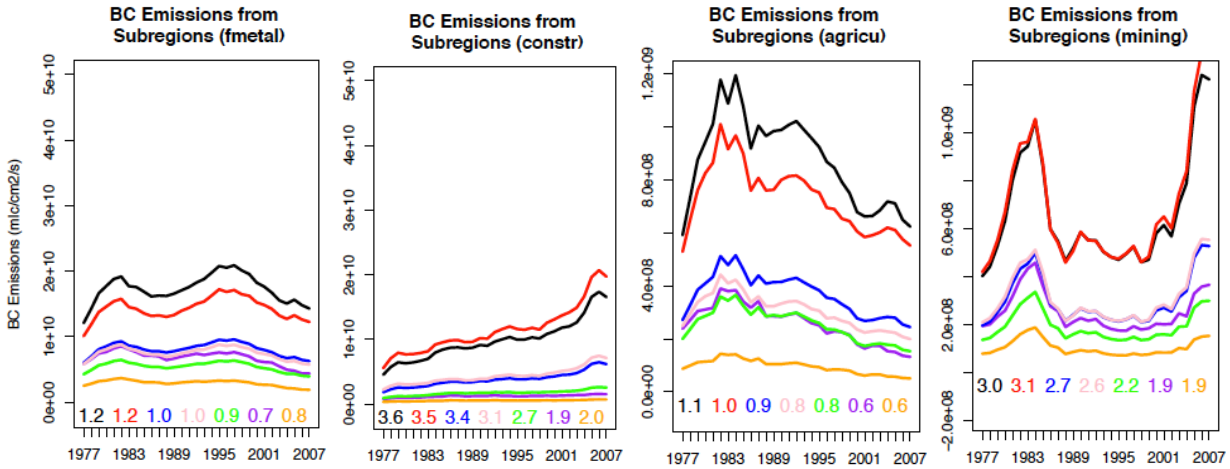

Figure 4.9: Same as Figure 4.8a but for the (a) fmetal; (b) constr; (c) agricu; and (d) mining sectors. Note vertical scale is not the same for each figure.

We now examine the temporal and spatial trends in individual sectors focusing on the two major sectors (FMETAL and CONSTR) as well as two interesting sectors (AGRICU and MINING). In nearly all sectors, growth tended to be the largest in the urban centers. In the transportation corridors and rural areas, BC emission trends varied from sector to sector. An exploration of the driving economic and societal influences can be found below in Section 4/Discussion. Transportation BC emissions from the FMETAL sector nearly doubled from 1977 – 1982, decreased slightly to 1987, increased again to a maximum around 1994, and subsequently decreased to nearly the same levels as in 1977 (Figure 4.9a). In contrast, BC emissions from transportation from the CONSTR sector more than doubled from 1977 – 2007 with a steady and gradual increase accelerating slightly after 2001 (Figure 4.9b). BC emissions from AGRICU doubled between 1977 and 1981 and subsequently dropped back to their 1977 levels by 2007 (Figure 4.9c). BC emissions from MINING also doubled from 1977 – 1981 only

to drop back down to 1977 levels after 1988. However, after 2000 the MINING emissions grew rapidly after 2000, tripling in urban centers and doubling in other sub-regions (Figure 4.9d).

Figure 4.10 examines the spatial distribution and changes in BC emissions from the same four sectors from above. In sectors that have decreased BC emissions (e.g. FMETAL and AGRICU), the decreases are found in all areas except the urban nodes. For the FMETAL sector, Detroit has the highest BC emissions in 1977 but by 2007 both New York City and Detroit are major FMETAL transportation nodes (Figure 4.10a). In sectors that have increased BC emissions (e.g. CONSTR and MINING), the increases are found everywhere, but the highest increases are found in the urban nodes, with maximum growth in the New York City urban center.

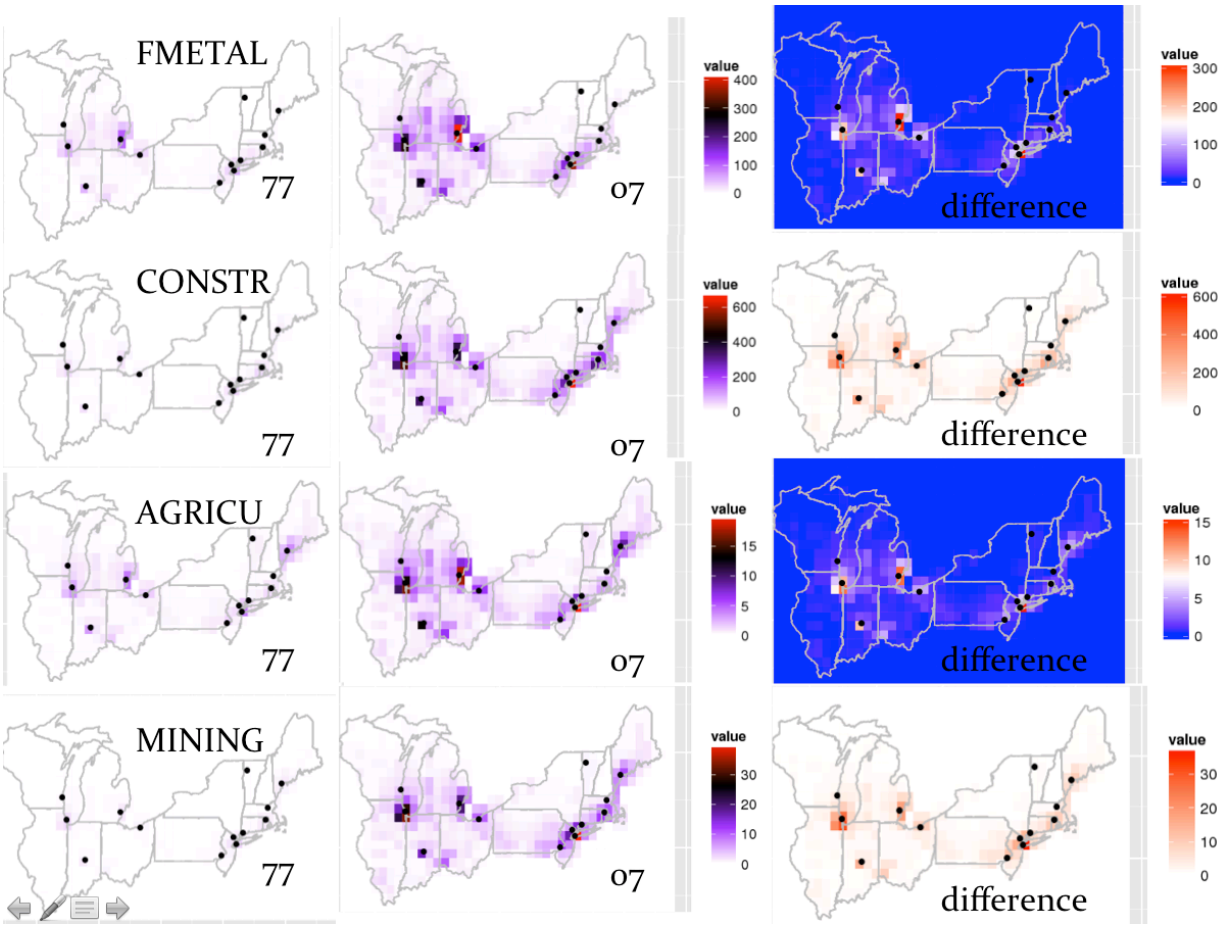

Figure 4.10: BC emissions from 1977 (left) and 2007 (middle) and the difference (2007 minus 1977, right) for FMETAL, CONSTR, AGRICU, and MINING (top to bottom).

VI. Discussion

We now interpret the preceding data to answer the following questions: (1) What has the BC emissions trend been from 1977 – 1978 and what are the major factors that have driven that trend? (2) What economic sectors dominate the BC emissions and what major changes have occurred from 1977 – 2007? (3) Are these changes consistent with established changes in regional economic structure, globalization, and developments in the transportation sector? (4) What are the remaining uncertainties and presuppositions in this analysis and how does this impact our ability to draw conclusions from the historical period? (5) What can we expect for future BC emissions in this region?

The first question is the easiest one to answer. BC emissions in the MNUS increased through, first rapidly and then gradually, until the late 1990s after which they have plateaued and show evidence of a decrease by 2007. This trend results from two primary factors: freight transportation has increased by a factor of around 6 while BC EF has decreased by nearly 80% over the same historical time period. These overall magnitude and changes in freight volume, however, are not uniform across industrial sectors.

Throughout the historical period two industrial sectors have dominated the BC transportation emissions signal: fabricated metal (FMETAL) and construction (CONSTR). The fabricated metal sector, which emitted over half of the BC emissions in 1977 had two peaks in 1982 and 1996 but has decreased gradually from 1997 to 2007 to represent roughly one-third of total BC transportation emissions in 2007 (Figure 4.5). The BC emissions from the construction sector, in contrast, has increased gradually and steadily from 1977, where they represented roughly 10% of BC transportation emissions, to 2007, where they are comparable to the fabricated metal emissions. Tao et al. (2010), looking only at the Midwestern US, found a

comparable drop in primary and fabricated metal manufacturing and attribute the drop to globalization (i.e. production of these goods requires less sophisticated technology and is readily replaced by importation). Tao et al. (2010) also found, in contrast to our results, the construction sector decreased by nearly 40% from 1970 – 2000, although this difference is due to differences in aggregated sector grouping.

During this historical period we expect to see signs of both globalization and structural changes to regional economies. Globalization is indeed observed since the growth in the total freight volumes is greater than concurrent growth in GDP (Figure 4.6). But does our data show any changes to regional economies? Between 1977 and 2007 the 97.5th percentile of all BC grew by 40% while the mean value increased by 30% (data not shown) indicating a clustering of emissions around the urban areas with the highest BC emissions (Figures 4.4 and 4.8). We also show that the BC emissions along major transportation corridors has decreased during the historical period, but this is largely due to decreased BC EF (Figure 4.8). Removing the impact of EF changes (EF_{const}) we see that the growth in freight volume along transportation corridors is less than growth in the urban nodes, but still show significant growth (Figure 4.8).

We also find that individual sectors show significantly different trends during the historical period. For instance, it is only in urban centers that BC emissions from fabricated metal transportation increase. In all other sub-regions we see decreasing BC emissions (Figures 4.9a and 4.10a). This relative change is also noted for the agricultural sector, although the magnitude of the BC emissions is less than that from the fabricated metal sector (Figure 4.9c and 10c). In general, decreasing BC emissions is a reflection of cleaner transportation. Other sectors, such as the construction sector, have increased BC transportation emissions in all sub-regions, with the greatest increases seen in and around urban areas (Figure 4.9b and 10b). Finally, other

sectors, such as the mining sector, show more complicated trends over the historical period. MINING sector BC transportation emissions peaked in the early 1980s, decreased until 2000, and peaked again by 2007 (Figure 4.9d). Tao et al. (2010) also note this peak in the early 1980s and attribute it to the oil price spike as well as to a decline in domestic use of coal. After 2000, mining employment doubled (US DOT/FHA, 2013) and mining related GDP nearly doubled between 2000 and 2007 (US BEA, 2015).

Our analysis highlights many of the complex changes impacting BC emissions from transportation sources from 1977 – 2007. However, the scope of this study has required externalizing and simplifying many potentially important factors. We do not simulate international transportation here; we only simulate transportation between industries within a limited number of states. We also simplify changes in the railroad transportation fleet, in part since information on many of these changes are not publically available and remain highly uncertain. We also ignore the growth of intermodal transportation (Costello, 2013) or changes in HDDV and railroad competition, which increased after the industry deregulation of the Motor Carrier Act of 1980 (Keebler, 2002; Costello, 2013).

Many of the current trends in transportation and emissions standards are expected to continue into the future, so we expect BC emissions from transportation in the MNUS to continue to decline. However, it is difficult to predict changes in individual sectors (e.g. the spike in mining freight volume after 2000), but continuing work with REIMs may provide valuable information as to potential changes in individual sectors into the future.

VII. Conclusions

In this paper we establish a framework to estimate BC emissions from HDDV and railroad transportation in the MNUS from 1977 – 2007 using available economic and shipment

data. This work builds upon Donaghy and Chen (2011) and Brown-Steiner et al. (in press) in which a regional econometric input-output model (REIM) was developed, time series of freight flows was derived, and BC transportation emissions was distributed and gridded. This modeling approach allows the parsing of transportation emissions of BC by state and by sector, which in turn allows for a more detailed analysis of the overall trends in BC emissions. We also isolate the influence of changes to the economic sector and resulting demand for freight shipments and the influence of changes in the BC emission factor due to increased regulatory efforts and technological and efficiency innovations.

The BC emissions data derived in this study are comparable to data from other existing BC emissions inventories. The MNUS regionally averaged BC emissions from this work show the same temporal trends as the MACCity BC emissions: a gradual increase from 1977 – 2000 followed a steady decline from 2000 to 2007 (Figure 4.3). While we do not have the spatial resolution and thus the capability of reproducing the real-world highway system that the HTAPv2 inventory has produced, we do distribute interstate emissions through an stylized link-and-node transportation network. This framework creates more dispersed spatial pattern of BC transportation emissions than the MACCity inventory, which distributes emissions based with a population proxy (Figure 4.4).

We find that while total demand for freight transportation has increased from 1977 – 2007, recent regulatory efforts to decrease the BC emission factor from HDDVs have resulted in decreasing emissions of BC from the transportation sector after 2000. Without the increasingly stringent BC emission factor regulations total BC emissions from transportation would be nearly five times as high as current levels (Figure 4.7). Inversely, without the increased demand for freight transportation, BC emissions could be nearly one-third of current levels.

Two industrial sectors dominate the BC emissions trend: the fabricated metal sector (FMETAL) and the construction sector (CONSTR). The FMETAL sector dominated the BC transportation emissions from 1977 – 2000, but has been decreasing steadily since 2000 (Figure 4.5 and 4.9). At the same time the CONSTR sector, which made up only a small fraction of total BC transportation emissions in 1977 has grown steadily from 1977 – 2007 to make up a comparable portion of the total BC transportation emissions than the FMETAL sector in 2007 (Figure 4.5 and 4.9).

We find that changes in BC emissions are not uniform across the MNUS region. In almost every sector, BC transportation emissions have increased in and around urban centers (Figure 4.9), which are serving as nodes in production networks and the freight distribution network. In sectors that have increasing BC transportation emissions, increases are seen across all sub-regions in the MNUS (Figure 4.10). However, activities of sectors that show decreasing total BC transportation emissions (such as the FMETAL and AGRICU sectors) are found largely outside of the urban centers (Figure 4.10). Large decreases are noted in the stylized transportation corridors between major clusters of urban nodes while smaller decreases are noted in rural regions (Figure 4.10).

We find that the rate of growth of the total tonnage of freight shipped in the MNUS from 1977 to 2007 is greater than the rate of growth of Real GDP in the same region over the same period (Figure 4.6). These trends combined with the concentration of BC transportation emissions in and around urban centers (Figures 4.9 and 4.10) are consistent with clusters if activities exploiting economies of scale as well as the evolution of a more fragmented production system. While the total freight movement is increasing over the entire MNUS region, a greater increase is concentrated near production nodes which results in an increasing concentration of

BC transportation emissions at these nodes and decreasing BC transportation emissions in other regions (Figure 4.8).

This study has shown that this framework (i.e. using a REIM for deriving commodity flows and a link-and-node distribution methodology for estimating BC transportation emissions) is able to accurately characterize BC emissions over a historical period over the MNUS. The same framework can be used to estimate future BC emissions under a set of stylized economic and regulatory scenarios. Doing so will enable one to derive the potential implications of changes in the economic and production systems as well as implications of future technological or regulatory changes to BC emissions, which could help inform decision makers and regional municipalities into the future.

VIII. Acknowledgements

The authors would like to thank the Environmental Protection Agency (EPA) (Project Number: RD-83428301-0) for funding. We would also like to thank Natalie Mahowald, Huaizhu Oliver Gao, Max Zhang, and Gianfranco Piras for their assistance throughout this project, as well as everyone who contributes to the R-Project and the invaluable tools they have created.

IX. References

Anderson, W.P., 2012. Public policy in a cross-border economic region. Int. J. Public Sect. Manag. 25, 492–499. doi:10.1108/09513551211260694

Anderson, W.P. and Coates, A., 2010. "Delays and Uncertainty in Freight Movements the Canada-US Border Crossings." *Transportation Logistics Trends and Policies: Successes and Failures, Proceedings of the 45th Annual Conference of the Canadian Transportation Research Forum*, pp. 129-143.

Anenberg, S. C. et al. (2012), Global air quality and health co-benefits of mitigating near-term climate change through methane and black carbon emission controls., *Environ. Health Perspect.*, *120*(6), 831–9, doi:10.1289/ehp.1104301.

Bivand, S., R.S., Edzer J. Pebesma, Virgilio Gomez-Rubio, 2008. Applied spatial data analysis with R. Springer, NY. http://www.asdar-book.org/

Bivand, R.S. (2012). classInt: Choose univariate class intervals. R package version 0.1-19. http://CRAN.R-project.org/package=classInt

Bivand, R.S. and Nicholas Lewin-Koh (2013). maptools: Tools for reading and handling spatial objects. R package version 0.8-23. http://CRAN.R-project.org/package=maptools

Bond, T.C., Bhardwaj, E., Dong, R., Jogani, R., Jung, S., Roden, C., Streets, D.G., Trautmann, N.M., 2007. Historical emissions of black and organic carbon aerosol from energy-related combustion, 1850-2000. Global Biogeochem. Cycles 21, n/a–n/a. doi:10.1029/2006GB002840

Bond, T.C., Streets, D.G., Yarber, K.F., Nelson, S.M., Woo, J.-H., Klimont, Z., 2004. A technology-based global inventory of black and organic carbon emissions from combustion. J. Geophys. Res. 109, D14203. doi:10.1029/2003JD003697

Bond, T. C. et al. (2013), Bounding the role of black carbon in the climate system: A scientific assessment, *J. Geophys. Res. Atmos.*, *118*(11), 5380–5552, doi:10.1002/jgrd.50171.

Brown-Steiner, B., Chen, J., and Donaghy, K., in press. The Evolution of Freight Movement and Associated Non-Point Source Emissions in the Midwest-Northeast Transportation Corridor of the United States, 1977 – 2007. In: *The Region and Trade: New Analytical Directions.* Batabyal, P.A. and Nijkamp, P. (eds).

Castells, M. (2000) The Rise of the Network Society, second edition. Oxford: Blackwell.

Chen, J. and Donaghy, K.P. (2012) "Econometric Estimation and Qualitative Analysis of a Dynamic Commodity-Flow Model for Studying impacts of Globalization and Infrastructure System Changes on Regional Air Quality," paper presented at the North American Meetings of the Regional Science Association International, Ottawa, Canada, November 8, 2012.

Costello, B. (2013), The Trucking Industry: The Lynchpin of the U.S. Economy, *Bus. Econ.*, *48*(3), 195–201, doi:10.1057/be.2013.16.

Donaghy, K.P. (2007). Globalization and Regional Economic Modeling: Analytical and Methodological Challenges in Cooper, R., Donaghy, K.P., and Hewings, G. (eds) Globalization and Regional Economic Modeling.

Donaghy, K.P. (2012). *Urban environmental imprints after globalization.* Regional Environmental Change, 12(2).

Donaghy, K.P. and Chen, J. (2011) "Generating Spastial Time Series on Interstate Inter-industry Freight Flows," paper presented at the National Urban Freight Conference, Long Beach, California, October 12-14.

Feenstra, R.C. (1998). *Integration of Trade and Disintegration of Production in a Global Economy*. Journal of Economic Perspectives, 12(4).

Ferguson, C.E. (1969). *The Neoclassical Theory of Production and Distribution*. Cambridge: Cambridge University Press.

Handa, D., Nakajima, H., Arakaki, T., Kumata, H., Shibata, Y., Uchida, M., 2010. Radiocarbon analysis of BC and OC in PM10 aerosols at Cape Hedo, Okinawa, Japan, during long-range transport events from East Asian countries. Nucl. Instruments Methods Phys. Res. Sect. B Beam Interact. with Mater. Atoms 268, 1125–1128. doi:10.1016/j.nimb.2009.10.115

Hijmans, R.J. & Jacob van Etten (2013). raster: raster: Geographic data analysis and modeling. R package version 2.1-25. http://CRAN.R-project.org/package=raster

ICF (2005), *Assessing the Effects of Freight Movement on Air Quality at the National and Regional Level, Final Report*. April 2005. Prepared for the US Federal Highway Administration by ICF Consulting.

Jackson, R.W., Schwarm, W.R., Okuyama, Y., and Islam, S. (2006), "A Method for Constructing Commodity by Industry Flow Matrices," *Annals of Regional Science*, **40**, 909-920.

Janssen et al., (2012). *Health Effects of Black Carbon*. World Health Organization.

Jones, R.W. and Kierzkowski, H. (2001), "A framework for fragmentation," in S.W. Arndt and H. Kierzkowski (eds) *Fragmentation: new production patterns in the world economy.* New York: Oxford University Press, New York.

Junker, C., Liousse, C., 2008. and Physics A global emission inventory of carbonaceous aerosol from historic records of fossil fuel and biofuel consumption for the period. Atmos. Chem. Phys. 1195–1207.

Keebler, J. S. (2002), Trends in the Transportation of Goods in the U.S., *Journal of Transportation. Management*, 1–14.

Krishnamarthy, A. (2007). From Just In Time Manufacturing to On-Demand Services. Service Enterprise Integration, Chapter 1. Hsu C. (eds.) Integrated Service in Information Systems, 16.

Lamarque, J.-F., Bond, T.C., Eyring, V., Granier, C., Heil, A., Klimont, Z., Lee, D., Liousse, C., Mieville, A., Owen, B., Schultz, M.G., Shindell, D., Smith, S.J., Stehfest, E., Van Aardenne, J., Cooper, O.R., Kainuma, M., Mahowald, N., McConnell, J.R., Naik, V., Riahi, K., van Vuuren, D.P., 2010. Historical (1850–2000) gridded anthropogenic and biomass burning emissions of reactive gases and aerosols: methodology and application. Atmos. Chem. Phys. 10, 7017–7039. doi:10.5194/acp-10-7017-2010

Margreta, M., C. Ford, and M. A. Dipo (2009), U.S. Freight on the Move: Highlights from the 2007 Commodity Flow Survey Preliminary Data, *US Dep. Transp.*, 1–6.

Munroe, D., Hewings, G.J.D. (2007). The role of intraindustry trade in interregional trade in the MidWest of the U.S. In: Cooper, R.J., Donaghy, K., Hewings, G.J.D. (eds) Globalization and regional economic modeling. Springer, Heidelberg, pp 87-105.

NESCAUM (2006), *Scoping Study to Evaluate Locomotive Emissions Operating in New Haven, Connecticut and Potential Control Options, Final Report*. June 2006. Prepared by the Northeast States for Coordinated Air Use Management.

NYSDEC (2014), *2014 Annual Monitoring Network Plan, New York State Ambient Air Monitoring Program*. 2014. Bureau of Air Quality Surveillance, Division of Air Resources, New York State Department of Environmental Conservation.

Pebesma, E.J., R.S. Bivand, 2005. Classes and methods for spatial data in R. R News 5 (2), http://cran.r-project.org/doc/Rnews/.

Pérez, N., Pey, J., Cusack, M., Reche, C., Querol, X., Alastuey, A., Viana, M., 2010. Variability of Particle Number, Black Carbon, and PM 10 , PM 2.5 , and PM 1 Levels and Speciation: Influence of Road Traffic Emissions on Urban Air Quality. Aerosol Sci. Technol. 44, 487–499. doi:10.1080/02786821003758286

Pierce, D. (2014). ncdf: Interface to Unidata netCDF data files. R package version 1.6.7. http://CRAN.R-project.org/package=ncdf

Tao, Z., Williams, A., Donaghy, K., Hewings, G., 2007. A socio-economic method for estimating future air pollutant emissions—Chicago case study. Atmos. Environ. 41, 5398–5409. doi:10.1016/j.atmosenv.2007.02.013

Tao, Z., Hewings, G., Donaghy, K., 2010. An economic analysis of Midwestern US criteria pollutant emissions trends from 1970 to 2000. Ecol. Econ. 69, 1666–1674. doi:10.1016/j.ecolecon.2010.03.016

Uherek, E., T. Halenka, J. Borken-Kleefeld, Y. Balkanski, T. Berntsen, C. Borrego, M. Gauss, P. Hoor, K. Juda-Rezler, and J. Lelieveld (2010), Transport impacts on atmosphere and climate: Land transport, *Atmos. Environ.*, *44*(37), 4772–4816, doi:10.1016/j.atmosenv.2010.01.002.

US Bureau of Economic Analysis, "Gross domestic product (GDP) by state (millions of current dollars)," http://www.bea.gov/iTable/iTableHtml.cfm?reqid=70&step=10&isuri=1&7003=200&7035=-1&7004=naics&7005=6&7006=91000&7036=-1&7001=1200&7002=1&7090=70&7007=2007,2000&7093=levels, Accessed January 5, 2015.

US Census Bureau (2004), *2002 Economic Census: Vehicle Inventory and Use Survey: Unite States: 2002*. December 2004. US Department of Commerce, Economics and Statistics Administration, US Census Bureau.

US DOT (2013), *Freight Facts and Figures 2013.* 2013. Federal Highway Administration and the Bureau of Transportation Statistics.

US DOT (2002), *Freight Shipments in America: Preliminary Highlights from the 2002 Commodity Flow Survey.* 2002. US Department of Transportation, Bureau of Transportation Statistics.

US DOT (2005), *National Transportation Statistics 2004*. Bureau of Transportation Statistics.

US DOT (2010), *2007 Economic Census, Transportation, 2007 Commodity Flow Survey, United States*. April 2010. US Department of Transportation, US Department of Commerce, US Census Bureau, Bureau of Transportation Statistics.

US EPA (2009), *Emission Factors for Locomotives, Technical Highlights*. April 2009. Office of Transportation and Air Quality. EPA-420-F-09-025.

US EPA (2012a), *Report to Congress on Black Carbon*. March 2012. Department of the Interior, Environment, and Related Agencies, Appropriations Act 2010. EPA-450/R-12-001.

US EPA (2012b), *Development of Emission Rates for Heavy-Duty Vehicles in the Motor Vehicles Emissions Simulator MOVES 2010 Final Report*. August 2012. EPA-420-B-12-049.

US EPA (2013), *National ambient Air Quality Standards for Particulate Matter, Final Rule*. 2013. Federal Register, 78 (10), 3086 – 3287.

Yttri, K.E., Aas, W., Bjerke, A., Cape, J.N., Cavalli, F., Ceburnis, D., Dye, C., Emblico, L., Facchini, M.C., Forster, C., Hanssen, J.E., Hansson, H.C., Jennings, S.G., Maenhaut, W., Putaud, J.P., K, T., 2007. Elemental and organic carbon in PM10 : a one year measurement campaign within the European Monitoring and Evaluation Programme EMEP. Atmos. Chem. Phys. 7, 5711–5725.Israilevich, P., Hewings, G.J.D., Sonis, M. and Schindler, G.R. (1997), "Forecasting structural change with a regional econometric input-output model," *Journal of Regional Science*, **37,** 565-590.